NTNU – Trondheim
Norwegian University of
Science and Technology

Dynamic Behavior of a Full Scale Laboratory Model of a Catenary System by Measurements and Numerical Analysis

Fredrik Hugo Haugland

Abstract

The behavior of railway systems, in particular the overhead contact line (OCL), is considered in this thesis. The modelling of such systems with the use of the finite element method are important to carry out, both to determine the systems static and dynamic behavior. The dynamic behavior is primarily related to the relationship between the overhead contact line and the pantograph, which should ensure stable currents to the train.

The aim for this study was to make a numerical model of a simplified, laboratory version of an OCL. The laboratory model consisted of two spans approximately 15m long, with a support in the middle. The finite element modelling was carried out both by the use of Python scripting, and by the use of Abaqus/CAE version 6.14 as numerical software.

Laboratory measurements were conducted, primarily to validate the numerical model, but also to compare the behavior of the laboratory model in relation to existing OCLs. The results of the measurements indicated that the laboratory model was approximately 3-4 stiffer in the vertical direction, compared to existing OCLs.

The numerical model was compared with the measurements conducted in the laboratory, which comparison primarily was related to natural frequencies and the variation of elasticity along the span. Comparison between the results obtained in the laboratory and the numerical results showed the same trend both due to natural frequency and elasticity, but the numerical model was created both less stiff and more dense than the laboratory model. Despite the latter, the numerical model was regarded as plausible in comparison to the laboratory model, and it was further used in two parameter studies.

The parameter studies performed were related to:

1. The development of the first vertical natural frequency, for varied tension in the contact and messenger wire.

2. The effect of removing droppers from the system, in relation to the first and the second vertical natural frequency.

The results obtained in these parameter studies showed first of all that the development of the first natural frequency was dependent on whether it was the contact or messenger wire that was applied the highest magnitude of tension.

Further, the removal of a dropper in the model seemed to have more effect on the first natural frequency, than the second natural frequency.

In future work, it is recommended that natural frequencies of higher modes than the first and the second are investigated. The development of the first natural frequency of existing OCLs should be compared with the results obtained in the parameter study made in this thesis, to further validate the conclusions made.

Sammendrag

Denne avhandlingen tar for seg oppførselen til kontaktlednignsanlegget, som i jernbane-sammenheng forsyner togene med strøm. Modellering av slike systemer ved bruk av elementmetoden er viktig, både for å karakterisere systemets dynamiske og statiske egenskaper. Siden samspillet mellom kontaktledningsanlegget og pantografen som overfører strøm til toget er av dynamisk art, er det viktig å utforske de dynamiske egenskapene til kontaktledningsanlegget.

Målet med denne avhandlingen var å bygge opp en numerisk modell av en forenklet versjon av et kontaktledningsanlegg, altså en laboratoriemodell. Modellen i laboratoriet bestod av to spenn. Hvert spenn var ca. 15m langt, og det var festet en utkrager i midten av modellen. Modelleringen ble gjort som en kombinasjon av å generere skript i Python, samt ved bruk av Abaqus/CAE versjon 6.14 som programvare.

Det ble gjort målinger i laboratoriet, hvor både egenfrekvenser og variasjon av elastisitet langs modellen ble målt. Disse målingene skulle primært benyttes til validering av den numeriske modellen, men de ble også benyttet til å undersøke hvordan modellen i laboratoriet oppførte seg i forhold til eksisterende kontaktledningsanlegg. Det ble til slutt konkludert at modellen så ut til å være i størrelsesorden 3-4 ganger stivere enn vanlige kontaktlednign-sanlegg i Norge.

Den numeriske modellen så ut til å ha de samme egenskapene som modellen i laboratoriet, men den var modellert både litt for myk, samt noe tyngre. Det ble likevel antatt at mulighetene for videre parameterstudier ved hjelp av den numeriske modellen var gode. To parameterstudier ble dermed gjort, som omhandlet:

1. Se på utviklingen av modellens første egenfrekvens, hvor både strekkraften i kontaktledningen, samt strekkraften i bærelinen ble variert.

2. Se på effekten av å fjerne en hengetråd fra modellen, med første og andre egenfrekvens som interessant parameter.

Paramterstudiene antydet først og fremst at utviklingen til første egenfrekvens så ut til å være avhengig av hvor mye strekkraft som var påført i kontaktledningen, i forhold til hvor mye strekkraft som var påført i bærelinen. Det viste seg også at dersom en hengetråd ble fjernet fra modellen, hadde dette mer effekt på første egenfrekvens, enn på andre egenfrekvens.

For videre arbeid anbefales det å sjekke flere egenfrekvenser for modellen, for å bedre bestemme oppførselene til kontaktledningsanlegget. I tillegg anbefales det å sjekke hvordan

første egenfrekvens utvikler seg for eksisterende kontaktledningsanlegg, for å videre definere om konklusjonen i denne avhanglingen også stemmer for komplette spenn.

Acknowledgment

I wish to show my gratitude to all who have supported me, or contributed to my master thesis. First of all, I wish to thank Associate Professor Anders Rönnquist for the opportunity to do this thesis, and the guidance he has provided throughout the work. I would also like to thank PhD Candidate Petter Røe Nåvik, for his patience, availability and guidance. Thank you Jonas Husebye for being a good support through long office hours, and for good discussions. Then I wish to thank Ragnar Moen for his help in the laboratory, and the possibility of using the equipment available.

Finally, I wish to thank both Bao-Mai Huynh and Lene Haugland for proof reading my work.

Contents

List of Figures

Symbols and notation

Abbrevations

CW   Contact wire

CW-xxkN - MW-yykN   Contact wire in xx kN tension, and messenger wire in yy kN tension

DFT   Discrete Fourier transform

DOF   Degree of freedom

FDFT   Finite discrete Fourier transform

FFT   Fast Fourier transform

GUI   Graphical user interface

MW   Messenger wire

NDOF   N degrees of freedom

OCL   Overhead contact line

OCS   Overhead contact line system

SDOF   Single degree of freedom

Latin letters

A_n Amplitude spectrum

c Wave propagation speed

$\mathbf{C}, \tilde{\mathbf{C}}$ Damping matrix, modal damping matrix

$K, \mathbf{K}, \tilde{\mathbf{K}}$ Stiffness, stiffness matrix, modal stiffness matrix

e Elasticity (flexibility)

E Young's modulus of elasticity [N/m^2]

f	Frequency [Hz]
f_n	Natural frequency associated with mode shape n
f_N	Nyquist frequency
F_n	Complex frequency function
H_{CW}	Tension in contact wire [N]
H_{MW}	Tension in messenger wire [N]
i	imaginary unit (i.e $i=\sqrt{-1}$)
I	Second moment of inertia [m^4]
L	Span length [m]
m, $\mathbf{M}$, $\tilde{\mathbf{M}}$	Mass [kg], mass matrix, modal mass matrix
m'	Mass per unit length [kg/m]
q, $\mathbf{q}$	generalized displacement/rotation, generalized displacement/rotation vector
r, $\mathbf{r}$	displacement/rotation, displacement/rotation vector
$S(f)$	Spectral density function
t	Time
T	Temperature

Greek letters

α	Stiffness-proportional damping coefficient *or* thermal expansion coefficient
β	Mass-proportional damping coefficient
δ	Logarithmic decrement
ϵ	Strain

ζ Damping ratio

θ_n Phase spectrum

ν Poisson's ratio

λ Eigenvalue

σ Stress *or* standard deviation

Φ_n, Φ Eigenvector, mode shape matrix

ω Circular frequency [rad/s]

ω_n Natural frequency associated with mode shape n

Symbols with both latin and greek letters

Δf Frequency segment

Δt Time step

ΔT Temperature change

Chapter 1

Introduction
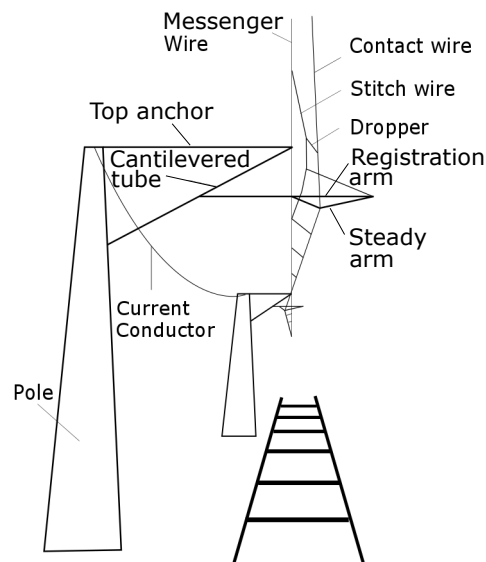
Figure 1.1: Example of an overhead contact line system (Kiessling et al., 2009).

Overhead contact line systems (OCS) for railways is the part of the railway that provides energy to the trains, and include components such as overhead contact line (OCL), cantilevers, poles, foundations, and conductors that provide currents. Some of the main components are visualized in Figure 1.1.

In this thesis, the OCL will be studied, which includes the contact wire, messenger wire, stitch wire, droppers and supports. Figure 1.2 gives a further introduction to how these components looks like in existing OCLs.

1
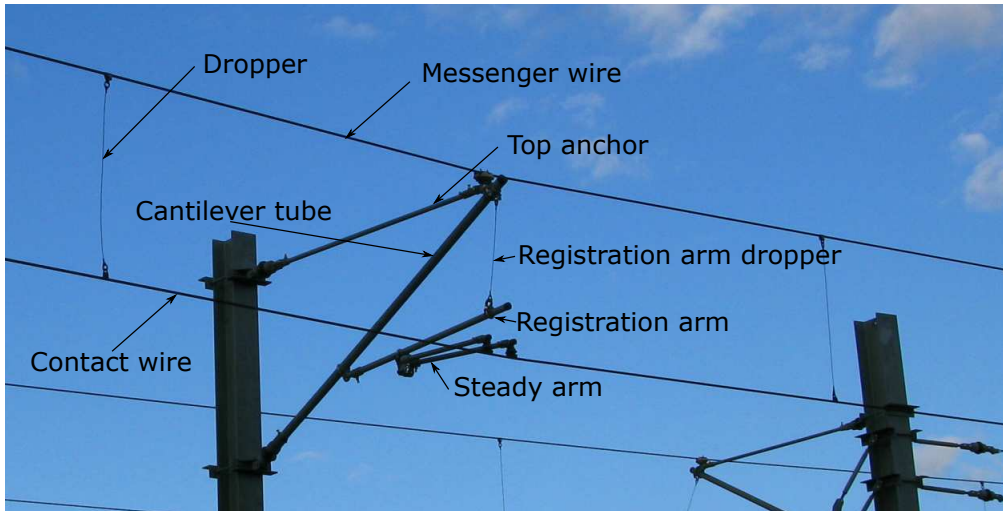
Figure 1.2: Description of main components in an OCL, without stitch wire (WordPress, 2010).

The contact wire is the main component, which transfers electricity to the train, via a pantograph that is attached on the top of the train. An exampale of a pantograph is shown in Figure 1.3.

Figure 1.3: Pantograph attached on top of the train, collecting currents from the contact wire (WordPress, 2010).

At each of the poles (supports), the registration arm and the steady arm are connected to the contact wire, to maintain the right horizontal geometry of the contact wire. The messenger wire and the droppers are present to support the contact wire, and keep it in a steady elevation above the ground.

The contact between the pantograph and the contact wire is crucial to maintain as consistent as possible, and a great number of papers has been written on this matter (for instance Ambrósio et al. (2012)). Therefore, the contact and messenger wire are applied tension, to ensure a stable elevation above ground for the contact wire.

In Poetsch et al. (1997), it is mentioned that although the OCL and the pantograph form

a coupled dynamic system, it is important to do more research on the modelling and simulation of the OCLs, since describing its behavior turned out to be the limiting factor for the coupled behavior.

In particular, two factors give rise to problems related to the description of the dynamic behavior of the system:

- The system has very low damping, which is hard to estimate exactly.

- High computational costs due to high resolution both in space and time.

In this study, a model of a simplified OCL has been investigated. The model is located in a laboratory, at Norwegian University of Science and Technology. It is primarily being used as a model for parameter studies on OCL dynamic behavior.

1.1 Aim of the thesis

The primary aim of this thesis was to make a finite element model of a simplified OCL, to be able to characterize its dynamic behavior, with natural frequencies as the main parameter. It was therefore of interest to verify the numerical model, primarily related to natural frequencies, by doing measurements in the laboratory and comparing the results with the finite element model.

The modelling of the system included an additional aim itself. Since the components in the laboratory model, in the future, may be substituted by new components, it was of interest to generate a Python script to use as input to the numerical model. By the use of this script, one could easily change the geometric and material inputs of the model, whenever a change in the physical model was made.

After validating the model, a parameter study on natural frequencies was of interest, which could reveal further characteristics about the model.

1.2 The layout of the thesis

Chapter 2 starts out with a brief introduction to OCLs, and the main aspects of such systems (Chapter 2.1). The chapter then continues on about important background theory essential to understand, due to the content of this thesis (Chapter 2.2-2.9).

Chapter 3 describes the laboratory model, and explains the methods used to perform measurements on it.

In Chapter 4, the finite element modelling of the laboratory model is presented. This chapter is split into two parts. Chapter 4.1 explains the procedure for the creation and use of the Python script, while Chapter 4.2 and 4.3 goes through the modelling choices made to create the numerical model.

Chapter 5 goes through the results obtained in the laboratory measurements, related to natural frequency and damping ratios. In this chapter, the results are discussed as they are presented, and comparisons with existing OCLs are made.

In Chapter 6, the results from the laboratory tests and the numerical simulations are compared, as a validation of the numerical model. In this chapter, the tension in the contact and messeger wire, the first two vertical natural frequencies, and the elasticity along the span are the parameters used in the validation.

After the validation of the numerical model, parameter studies related to the first two natural frequencies of the system are presented in Chapter 7.

Note that discussions have been made in each chapter where results have been presented. This has been done to create continuity of the thesis, and to avoid confusion, as several topics are discussed.

Chapter 2

Background theory

2.1 Basic overview of overhead contact lines

The basic design of contact lines is best explained by a figure, see Figure 2.1. The OCL consists of contact wire, messenger wire, droppers, stitch wires, fixed points, registration arms and tension devices (Kiessling et al., 2009). The mentioned components are always included, except the stitch wire which is omitted in some systems.
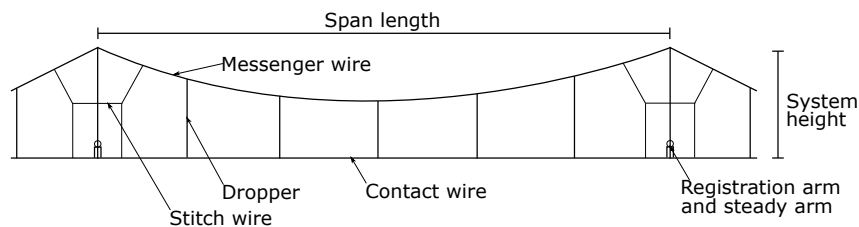
Figure 2.1: Basic design of an OCL span.

Note that the OCL is often referred to as *catenary system*, and these two terms will both be used throughout this thesis. Figure 2.1 resemble a catenary system called stitch wired system. Different types of systems exist, including *the compound catenary system* and *simple catenary system*. These two principles are shown in Figure 2.2.
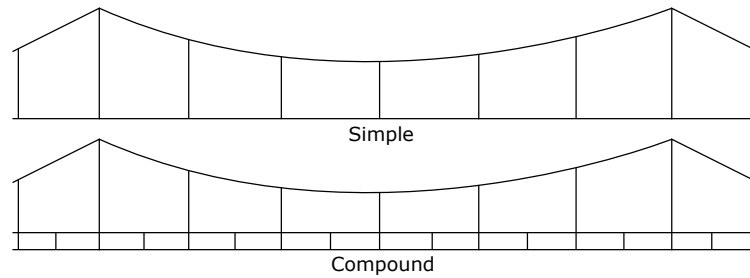
Figure 2.2: Two of the three main types of catenary design.

Compund catenary systems uses a second support wire, known as the *auxilary*, which contributes to an almost uniform stiffness along the span. The auxilary is mounted between the messenger wire and the contact wire.

Simple systems only support the contact wire with droppers throughout the span, making the stiffness dependent on the dropper distance. While compound catenary systems are used in Japan, simple or stitch wired systems are more common in Europe Oura et al. (1998).

2.1.1 Contact line systems in Norway

In general, there are three types of catenary systems in Norway: System 20, 25 and 35. In addition, there exist some older systems, which are not able to maintain the same running qualities as those mentioned. The following facts presented about the different systems in Norway can be found on the website Jernbanekompetanse (2014).

System 20 (S20)

S20 includes three versions, depending on running speed and building method. Building method primarily relates to whether stitch wires are used, or how big curvature each system can cope with. The curvature is measured as the radius of a thought circle that the railway track is part of, which principle is shown in Figure 2.3.

- System 20A is designed for speeds up to 200km/h, and is a system built with stitch wire. The tension in the contact and messenger wire is 10-10kN. The system is meant for distances with a curvature greater than 800m. The maximum span length is 75m, although it is recommended to use 70m or less.

- System 20B is designed for speeds up to 160 km/h, and is a system built without stitch wire. The tension in the contact and messenger wire is 10-10kN. The system is meant
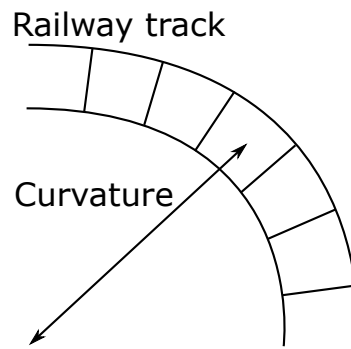
Figure 2.3: The definition of curvature, in relation to railway track.

for distances with curvature less than 800m, and the maximum span length is the same as for system 20A. An example of a span for system 20B is shown in Figure 2.4.
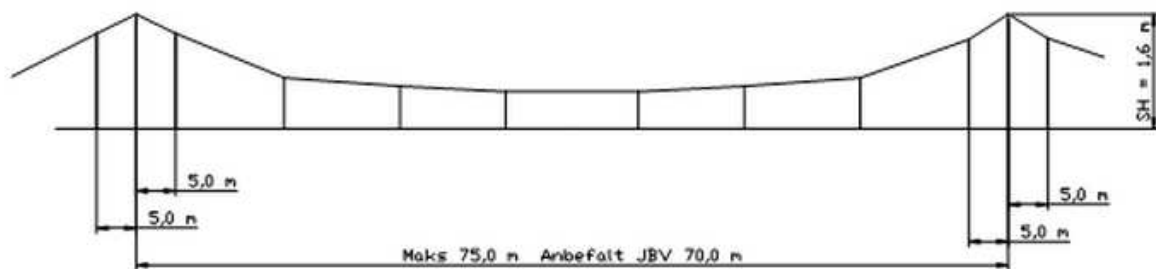
Figure 2.4: Catenary system 20B (Jernbaneverket, 2012).

- System 20C1 is primarily designed for tunnels, with speeds up to 200km/h. S20C1 can be built with or without stitch wires, and the tension in the contact and messenger wire is 13-13kN. The system is meant for distances with a curvature greater than 5000m, and the maximum span length is 45m.

- There is also a system called system 20C2, which is almost the same as system 20C1. It is built without stitch wires, but has the same tension in the contact and messenger wire as system 20C1. The maximum span length is only 30m.

System 25 (S25)

S25 is meant for speeds up to 250km/h, and is thus the system in Norway designed for the highest speeds. It is built with stitch wire, and the tension in the contact and messenger wire is 15-15kN. The system is meant for distances with curvature greater 1200m, and the max-

imum span length is 65m. It is primarily being used for the Airport Express Train between Gardermoen and Oslo. An example of a span for system 25 is shown in Figure 2.5.
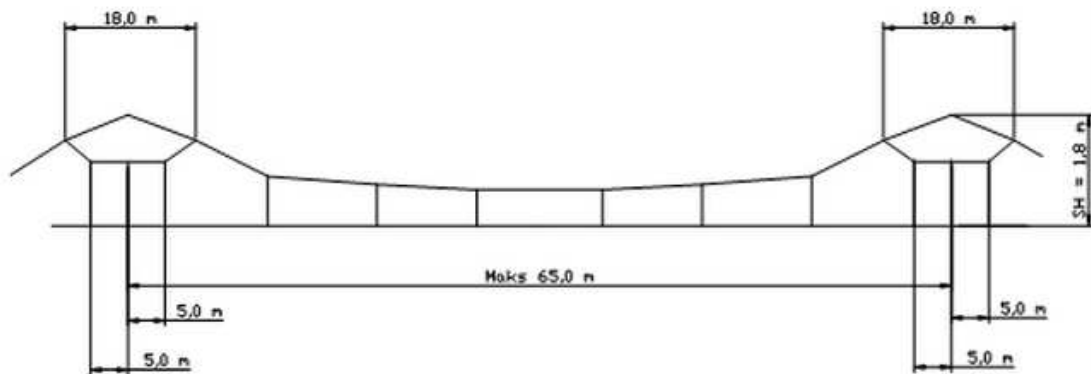
Figure 2.5: Catenary system 25 (Jernbaneverket, 2012).

System 35 (S35)

S35 is divided into two groups, S35 (with stitch wire) and S35 MS (without stitch wire). It is meant for speeds up to 130km/h, and is thus not an alternative for high speed tracks. The tension in the contact and messenger wire is 7.1-7.1kN.

Table 54

An additional, older catenary system used in Norway is Table 54. It is still in use, but new tracks are not being built with the use of this system. It can cope with train speeds up to 130km/h, and the tension in both the contact and messenger wire was set to 7.6kN. This tension was later changed, to be able to increase the maximum speed of the train, and the new tension-combination was 10kN in the contact wire and 5kN in the messenger wire (Nåvik, 2013).

Railway tracks in Norway

Figure 2.6: Railway tracks in Norway (Jernbaneverket, 2012).

Figure 2.6 shows the existing railway tracks in Norway. In total, there are 4135 km of railway tracks. Most of the tracks are electrified, but some distances still run without electricity. The south-eastern region of Norway is well covered, although there are still regions where both improvement of the existing tracks, and new tracks are needed.

2.1.2 Elasticity

As stated in Ambrósio et al. (2012), one of the main issues related to OCL design is to maintain the stiffness, or elasticity, of the contact wire as constant as possible due to transversal loading. The connection between the pantograph and the contact wire introduces an uplifting contact force, a necessary force to ensure stable currents to the train. If the uplifting force is too high, wear of both contact wire and pantograph may be one issue, aswell as the trains bypassing of the registration arms that may yield another. On the contrary, if the force is too low, contact loss may lead to electricity disruptions.

The goal is therefore to achieve as uniform contact force along the span as possible. As

known from simple mechanics, Hooke's law relates the force and displacement to stiffness or flexibility:

$$F = Kr = \frac{1}{e}r, \tag{2.1}$$

where F is the contact force [N], r is the vertical displacement [m], K is the stiffness, and e is the flexibility. In OCL design, it is common to use the term *elasticity*. The elasticity is the inverse of the stiffness, which makes it equal to the flexibility. A typical average value for the elasticity of high-speed OCLs is 0.5mm/N (Kiessling et al., 2009).

It is common to plot the elasticity along the span length for different systems, to see the variation. This is done to be able to optimize the elasticity to be as equal as possible, and an example of such a plot is shown in Figure 2.7.
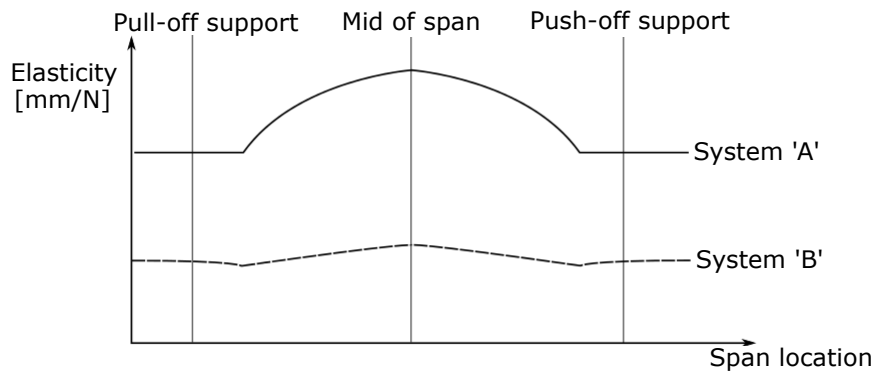
Figure 2.7: Location in span plotted against elasticity for two hypothetical OCLs.

Figure 2.7 does not show how the elasticity varies in reality, it is only meant to show the principle about varying elasticity. From the figure, it is noted that system 'A' has higher elasticity in the midspan than at the supports. System 'B' seems to have more or less equal elasticity along the span. The reason for this may be related to several factors, such as: Pre-sag of the contact wire, dropper spacing, tension system, and the use of stitch wires. These are topics that will be briefly explained explained further.

2.1.3 Tension system

Both the messenger wire and the contact wire are applied tension. The tension mechanism is introduced to maintain the magnitude of the tensile forces, and thus the vertical position of the contact wire, as constant as possible. The vertical position of the contact wire is primarily an issue when changes in temperature occur. This change can be compensated by the use of an automatic tension system. An example of such a system is shown in Figure 2.8 a).
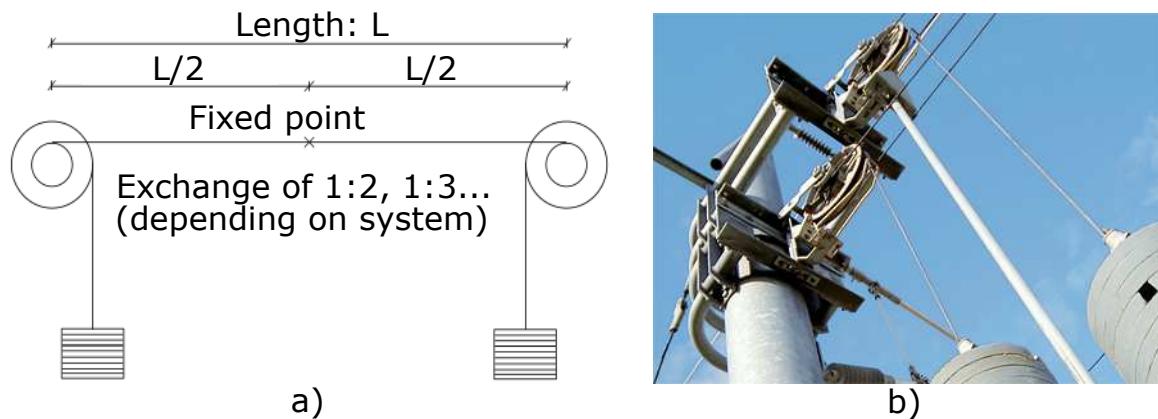
Figure 2.8: a) Basic design of a tension system, b) Tension system, with the use of concrete weights (Siemens, 2015).

The exchange of 1:3 or 1:2 means that the tension obtaiend in the wires are 3 or 2 times the force from the weights. In total, the variation of tensile forces should not be more than 11% (Kiessling et al., 2009) due to changes in temperature. Designs with tension weights and gear wheels (as shown in Figure 2.8), consists of a tension wheel with two rope drums on a common axle, and a blocking device. To achieve an exchange ratio higher than 1:1, the weights are attached to the outer part of the weel (the large drum), while the wire to be tensioned is attached to the inner part of the wheel (small split drum).

The weights used in the tension system are usually made of concrete or cast iron. Since cast iron has a greater density compared to concrete, it reduces the space required for the installation. This space-saving design is especially required in tunnels. Figure 2.8 b) shows how a tension system works in reality, where concrete weights are used to create tension.

The possibility of regulating the tension in the wires is important, especially when talking about high speed railway systems. In an earlier study this has been stated clearly: "To achieve the world record of 574.8 km/h, the contact wire was subjected to an axial load of 40 000N" (Ambrósio et al., 2012). This particular system experienced variations of 10 % in the contact wire tension in just a few hours due to temperature changes, which emphasizes that being

able to regulate the tension is important.

2.1.4   Supports and zig-zag installation

The supports are installed in two different ways: Either as push-off or as pull-off supports. These terms appear as a result of the installation of the contact wire. It is installed in a zig-zag formation to avoid wear of the pantograph, as seen in Figure 2.9. This is often referred to as *stagger* of the contact wire. The wear is reduced since the pantograph gets a wider working range on the contact wire. The latter explains why the pantograph is designed with a wide contact surface (see Figure 1.3).
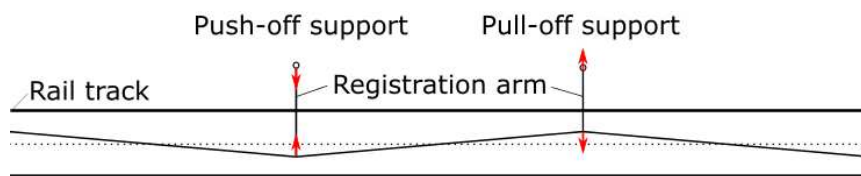
Figure 2.9: Zig-zag installation of the contact wire along the track, top view.

For a pull-off support, the contact wire is being pulled towards the support. Since the contact wire is in tension, it seeks back to the original position, creating tension in the registration arm. The opposite applies to the push-off support, where the registration arm is in compression. The red arrows in Figure 2.9 are meant to show whether the registration arm is in compression or in tension. Figure 2.10 shows the design of the registration arm and steady arm, both for a push- and a pull-off support.
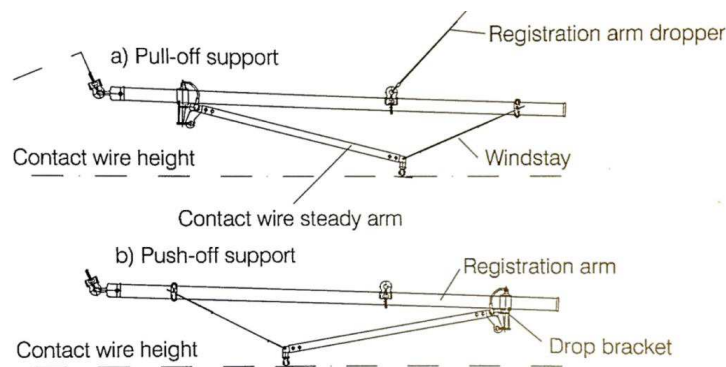
Figure 2.10: Registration and steady arm design for a) pull-off support, b) push-off support (Nåvik, 2013).

The support may be of various types, and a principle without the use of stitch wires is shown in Figure 2.11, which resembles a push-off support.
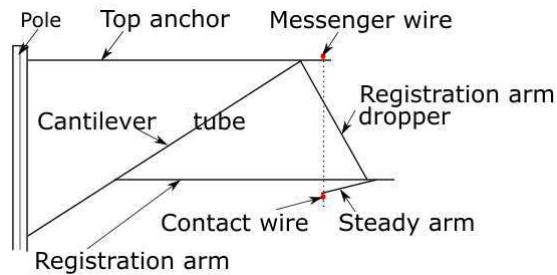
Figure 2.11: Support concept for a push-off support.

A pull-off support is showed in Figure 2.12.
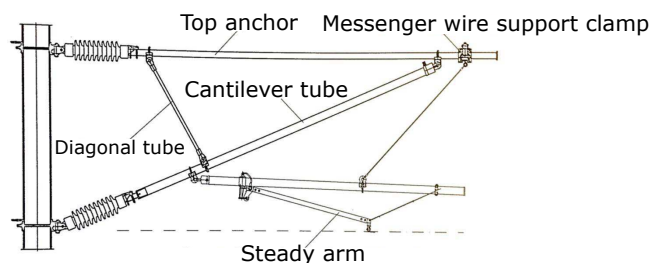
Figure 2.12: Support consept for pull-off support (Nåvik, 2013).

Note that the primary difference between a push- (Figure 2.11) and a pull-off (Figure 2.12) support relates to the position of the steady arm, and whether the registration arm is in tension or compression.

2.1.5 Stitch wire

The stitch wire is connected between the messenger wire and the contact wire, in the vicinity of the support. It has one main function, which is to make sure that the contact wires elasticity is as equal along the span as possible. The use of a stitch wire is illustrated in figure 2.13.

Figure 2.13 shows that by introducing stitch wires, the acting force on the messenger wire (F_c - contact force from pantograph) will move away from the more or less *rigid support* in comparison. If the droppers are assumed rigid in vertical direction, and $\Delta L_1 < \Delta L_2$, the vertical elasticity will increase by introducing stitch wires, since they will act as a softening component near the support.
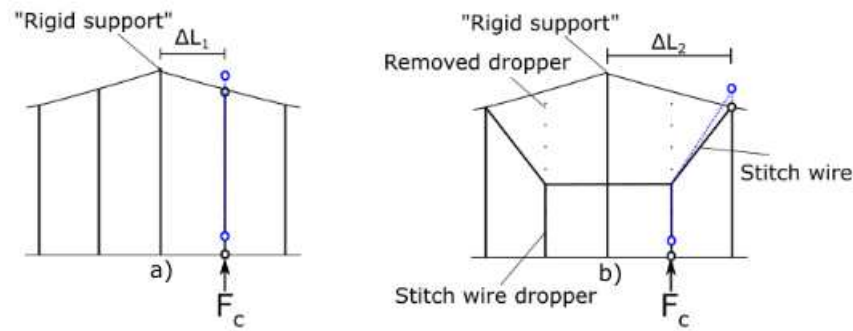
Figure 2.13: a) Without stitch wire, b) With stitch wire.

Depending on the desired running speeds, the length of the stitch wire may be between 6-22m, with 1-4 stitch wire droppers between the two connections to the messenger wire. By the use of stitch wires, bigger space between the supports may be allowed. This may result in lower investments, since the number of supports along the track is reduced.

2.1.6 Droppers

Droppers are installed between the contact and messenger wire along the span, such that the messenger wire can support the the contact wire vertically. The steady arm at the support should not be exposed to vertical load, since its working range in vertical direction is limited. This is ensured by the use of droppers, which transfers the vertical load via the messenger wire to the top anchor of the support. Figure 2.14 shows an example of a dropper, with its respective connections to both the contact wire and the messenger wire.
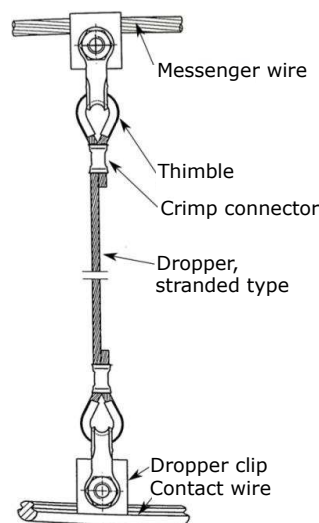
Figure 2.14: Dropper design, including its connection to the contact and messenger wire (Kiessling et al., 2009).

The droppers contribute to the distribution of elasticity along the span, and the location and spacing between them is thus important to consider. For instance, the elasticity for simple catenary systems are highly dependent on the dropper configuration, since they are the only components that connect the messenger and contact wire along the span. For these systems, the dropper distances should be calculated by standards, and not be placed too near the support.

2.1.7 Pre-sag

In some systems, the contact wire is installed with a contact wire pre-sag, typically 0.1% of the total span length (Kiessling et al., 2009). This makes the contact wire height above the ground lower in the middle of the span, than at the supports. The reason for applying pre-sag is both related to the elasticity of the system, and the deflection tolerance at the support, in contrast to the midspan. Since the contact force is preferred to be as constant as possible, the contact wire will achieve greater deflection in the midspan, than at the supports, due to higher elasticity. When installing pre-sag, the total deflection is the same in the midspan, though the relative vertical deflection compared to the support is reduced. The reduction in relative displacement creates less movement in the pantograph, and may thus improve the systems operability. This principle is shown in Figure 2.15.
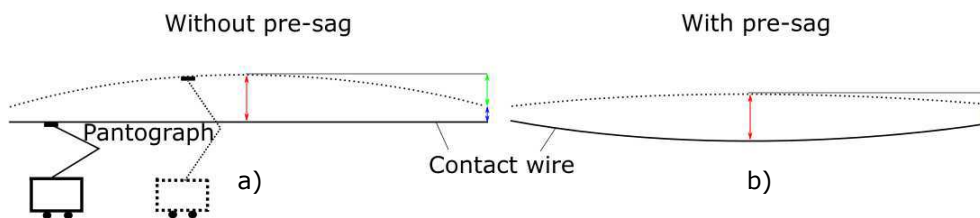
Figure 2.15: Pre-sag principle. a) Pre-sag not included. b) Pre-sag included.

In Figure 2.15, the dashed line is the vertically deflected contact wire. The red and blue markers are the mid-point deflection and the deflection at the support, respectively. The green marker shows the relative vertical displacement of the mid-point compared to the support.

However, when the train speed exceeds a certain limit, one should be aware that the pre-sag may contribute in a negative way. When the train approaches with high speed (above 200km/h (Kiessling et al., 2009)), the pantograph is being pushed down by the pre-sag in the midspan, creating unwanted dynamic behaviour. Pre-sag for speeds up to 200 km/h, with relatively large elasticity differences along the span, will although still improve the running

quality. Therefore, systems without the use of stitch wires are often combined with pre-sag.

2.2 Catenary modelling

The numerical modelling of OCLs can be compared with the modelling of wires/cables. The most common mathematical formulation that can be used to model wires are the string model, which mathematical formulation are given in Poetsch et al. (1997). Besides the string model, beam models are commonly implemented in finite element software, to represent the catenary wires. By introducing the beam models, both the bending stiffness are taken into account (Euler-Bernoulli beam), and the capability of including shear deformations (Timoshenko beam) are also possible. For more detailed theory about both the two mentioned beam formulations, see Cook et al. (2002).

Even though it is common to model the contact and messenger wire as beams, it is crucial to know that the characteristics of the wires are comparable to highly flexible cables. Highly flexible cables has no stiffness to resist lateral loads (Mathisen, 2014), which either can lead to far greater displacements than wanted, or to a singular stiffness matrix. Hence, the lateral stiffness is far less than the geometric stiffness of such components.

To avoid this problem, it is common to introduce a tensile stress to *activate* the geometrical stiffness. By applying a small amount of tensile stress, the geometric stiffness in highly flexible cables will be activated. An example of how to model a catenary system in two dimensions is shown in Figure 2.16.
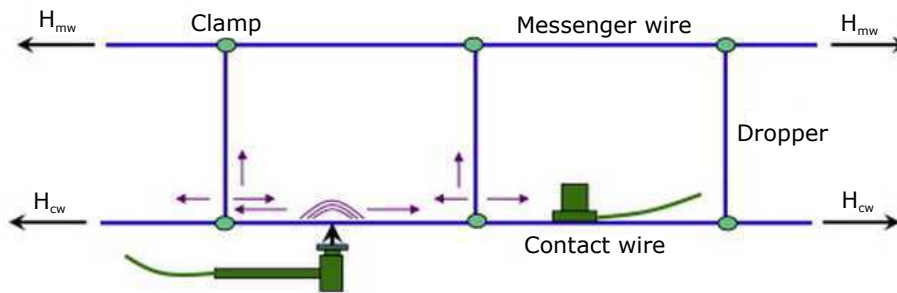
Figure 2.16: Example of a two dimensional model of a part of an OCL (Cho et al., 2010).

2.3 Wave propagation speed and natural frequency of an OCL

For high-speed OCL systems, the materials and tensile forces are selected such that the resulting wave-propagation velocity, c, in the contact wire is sufficiently high (Kiessling et al.,

2009):

$$c = 3.6\sqrt{\frac{H_{CW}}{m'_{CW}}}, \tag{2.2}$$

where H_{CW} is the tensile force in the contact wire [N], and m'_{CW} is the weight per unit length of the wire [kg/m]. The output from Equation 2.2 is in kilometers per hour, which is because of the pre-multiplied value "3.6".

As a reference value, the operating speed should not exceed $0.7c$. Consider the norwegian system 25 as an example: For a contact wire tension of 15kN, with a cross sectional area of 120mm^2 and mass per unit length equal to 1.09kg/m (Jernbanekompetanse (2014)), the maximum operating speed would be $v_{\text{operating}} = 0.7 \cdot 422$ km/h = 296 km/h. As mentioned earlier, system 25 has a cap speed of 250km/h, which is a conservative value in comparison to the maximum operating speed.

It should be noted that Equation 2.2 is a simplified version of the wave-propagation speed. The complete version includes the bending properties of the wire (Ambrósio et al., 2012):

$$c = 3.6\sqrt{\frac{\pi^2 EI}{m'_{CW}L^2} + \frac{H_{CW}}{m'_{CW}}} \tag{2.3}$$

where E is the Young's modulus [N/m^2], I is the second moment of inertia about the strong axis [m^4], and L is the beam (span) length [m]. Due to research carried out by Poetsch et al. (1997), the effect of bending stiffness will hardly influence simulations with respect to low-frequency behavior. As the frequency exceeds 50Hz, the bending term becomes more important.

The first natural frequency of a catenary system is strongly related to the wave propagation speed, and is given as (Kiessling et al., 2009):

$$f_1 = \frac{\bar{c}}{2L} = \frac{\sqrt{\frac{(H_{CW}+H_{MW})}{(m'_{CW}+m'_{MW})}}}{2L} \tag{2.4}$$

where $\bar{c}$ is the mean wave propagation speed, and where the bending term has been neglected.

2.4 The eigenvalue problem

Consider the undamped, free vibration of a system, where the damping matrix and the external loads are zero ($\mathbf{C}=\mathbf{0}$, $\mathbf{P}(t)=\mathbf{0}$). The equation of motion may thus be written as (Mathisen, 2014):

$$\mathbf{M\ddot{r}} + \mathbf{Kr} = \mathbf{0} \tag{2.5}$$

where $\mathbf{M}$ is the mass matrix, $\mathbf{K}$ is the stiffness matrix and $\mathbf{\ddot{r}}$, $\mathbf{r}$ are the acceleration and displacement vectors, respectively. The solution to Equation 2.5 may be written in the frequency domain as:

$$\mathbf{r} = \mathbf{\Phi}_n e^{i\omega_n t} \tag{2.6}$$

By substituting Equation 2.6 into Equation 2.5, the eigenvalue problem is obtained as:

$$\left(\mathbf{K} - \lambda_n \mathbf{M}\right)\mathbf{\Phi}_n = \mathbf{0} \tag{2.7}$$

where $\lambda_n = \omega_n^2$ is the n$^{\text{th}}$ eigenvalue, $\mathbf{\Phi}_n$ is the corresponding eigenvector (mode shape), and ω_n is the n$^{\text{th}}$ natural frequency [rad/s]. By assuming that the eigenfrequencies are independent of damping, the solving of the eigenvalue problem gives both the natural frequencies and the accompanying mode shapes of a system.

2.5 Free vibration of systems with damping - the modal method

In this chapter, some basic consepts about multi-degree of freedom (NDOF) dynamic systems with damping will be derived, as a prequel to the later derivation of Rayleigh damping. Due to Chopra (2007), the equation of motion in original degrees of freedom $\mathbf{r}$ may be formulated as:

$$\mathbf{M\ddot{r}} + \mathbf{C\dot{r}} + \mathbf{Kr} = \mathbf{P}(t) \tag{2.8}$$

When the external load, $\mathbf{P}(t) = 0$, Equation 2.8 represents free vibrations with damping included.

It is possible to represent any set of N independent vectors by any other vector of order N, which leads to the possibility of modal expansion of any displacement vector $\mathbf{r}$ as the following:

$$\mathbf{r} = \sum_{n=1}^{N} \phi_n q_n = \mathbf{\Phi} \mathbf{q} \tag{2.9}$$

where q_n are the modal coordinates, ϕ_n are the accompanying mode shape, and $\mathbf{q}$ is a vector of order N. $\mathbf{\Phi}$ is often referred to as the mode shape matrix (Strømmen (2014)), which is a N x N sized matrix. Thus, by inserting Equation 2.9 into Equation 2.8 (for $\mathbf{P}(t) = 0$), and pre-multiplying the entire equation by $\mathbf{\Phi}^T$, it will render:

$$\mathbf{\Phi}^T \mathbf{M} \mathbf{\Phi} \ddot{\mathbf{q}}(t) + \mathbf{\Phi}^T \mathbf{C} \mathbf{\Phi} \dot{\mathbf{q}}(t) + \mathbf{\Phi}^T \mathbf{K} \mathbf{\Phi} \mathbf{q}(t) = \mathbf{0} \tag{2.10}$$

Equation 2.10 may be slightly re-written into the following:

$$\tilde{\mathbf{M}} \ddot{\mathbf{q}}(t) + \tilde{\mathbf{C}} \dot{\mathbf{q}}(t) + \tilde{\mathbf{K}} \mathbf{q}(t) = \mathbf{0} \tag{2.11}$$

In Equation 2.11, $\tilde{\mathbf{M}}$, $\tilde{\mathbf{K}}$ are referred to as the modal mass and modal stiffness matrices, which are diagonal, positive definite matrices. $\tilde{\mathbf{C}}$ are the modal damping matrix, which may or may not be diagonal, depending on the distribution of damping in the system (Chopra, 2007). If $\tilde{\mathbf{C}}$ is diagonal, which will be assumed in all further derivations, Equation 2.11 represents N uncoupled differential equations:

$$\tilde{M}_n \ddot{q}_n + \tilde{C}_n \dot{q}_n + \tilde{K}_n q_n = 0 \tag{2.12}$$

Equation 2.12 is now on the same form as a single degree of freedom (SDOF) system with damping, where $\tilde{M}_n$, $\tilde{C}_n$ and $\tilde{K}_n$ are defined as:

$$\tilde{M}_n = \phi_n^T \mathbf{M} \phi_n \qquad \tilde{C}_n = \phi_n^T \mathbf{C} \phi_n \qquad \tilde{K}_n = \phi_n^T \mathbf{K} \phi_n \tag{2.13}$$

With anology to SDOF systems, the relation between modal stiffness and modal mass for each mode is defined as:

$$\tilde{K}_n = \omega_n^2 \tilde{M}_n \tag{2.14}$$

and the damping ratio, ζ_n, for each mode can be defined as:

$$\zeta_n = \frac{\tilde{C}_n}{\tilde{C}_{n,\text{critical}}} = \frac{\tilde{C}_n}{2\tilde{M}_n\omega_n} \tag{2.15}$$

2.6   Rayleigh damping

Mass- and stiffness-proportional damping may be defined as:

$$\mathbf{C} = \alpha\mathbf{M} \quad \text{or} \quad \mathbf{C} = \beta\mathbf{K} \tag{2.16}$$

Classical damping is assumed, which means that the modal damping matrix $\tilde{\mathbf{C}}$ is assumed diagonal, and that the system possess the same natural modes as those of an undamped system (Chopra, 2007). Each of the components in the modal damping matrix $\tilde{\mathbf{C}}$ can thus be expressed as:

$$\tilde{C}_n = \alpha\tilde{M}_n \quad \text{or} \quad \tilde{C}_n = \beta\tilde{K}_n \tag{2.17}$$

In Equation 2.17, α and β are constants that relates to the mass- and stiffness-proportional damping, respectively. For the mass-proportional damping, the damping ratio can be obtained by inserting Equation 2.15 into $\tilde{C}_n = \alpha\tilde{M}_n$:

$$\zeta_n = \frac{\alpha}{2}\frac{1}{\omega_n} \quad \Rightarrow \quad \alpha = 2\zeta_n\omega_n \tag{2.18}$$

The similar can be done for the stiffness-proportional damping, by inserting Equation 2.14 and 2.15 into $\tilde{C}_n = \beta\tilde{K}_n$:

$$\zeta_n = \frac{\beta}{2}\omega_n \quad \Rightarrow \quad \beta = \frac{2\zeta_n}{\omega_n} \tag{2.19}$$
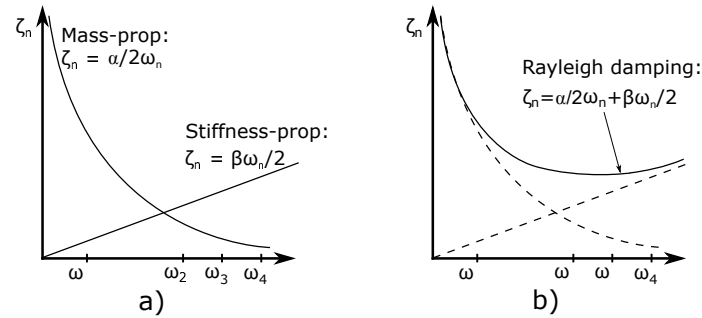
Figure 2.17: Variation of modal damping ratios with respect to natural frequency, a) both mass- and stiffness-proportional damping, b) Mass- and stiffness-proportional damping combined to Rayleigh damping.

Figure 2.17 a) shows how the mass- and stiffness-proportional damping ratio develops with natural frequency, while b) shows the combination of mass- and stiffness-proportional damp-

ing. This leads to the definition of the damping ratio for the nth mode due to Rayleigh damping (Chopra, 2007):

$$\zeta_n = \frac{\alpha}{2}\frac{1}{\omega_n} + \frac{\beta}{2}\omega_n \tag{2.20}$$

If two damping-ratios for the ith and the jth mode and their corresponding natural frequencies are known, Equation 2.20 may be used to create the following set of equations:

$$\frac{1}{2}\begin{bmatrix} \frac{1}{\omega_i} & \omega_i \\ \frac{1}{\omega_j} & \omega_j \end{bmatrix}\begin{bmatrix} \alpha \\ \beta \end{bmatrix} = \begin{bmatrix} \zeta_i \\ \zeta_j \end{bmatrix} \tag{2.21}$$

The two algebraic equations shown in Equation 2.21 can be solved to determine α and β. If both mode i and j are assumed to have the same damping ratio, ζ, the coefficients may be computed directly as:

$$\alpha = \zeta\frac{2\omega_i\omega_j}{\omega_i + \omega_j}, \qquad \beta = \zeta\frac{2}{\omega_i + \omega_j} \tag{2.22}$$

After computing the coefficients α and β, the damping matrix due to Rayleigh damping is known as:

$$\mathbf{C} = \alpha\mathbf{M} + \beta\mathbf{K} \tag{2.23}$$

2.7   Experimental estimation of damping

For experimental data, it is common to use logarithmic decrement to estimate damping. Due to Chopra (2007), the logarithmic decrement for lightly damped systems can be expressed as:

$$\delta = \frac{1}{m}\ln\left(\frac{r_1}{r_{1+m}}\right) \approx 2\pi\zeta \tag{2.24}$$

where m is the number of peaks in the data set, and r_1 is the first peak. r denotes the amplitude of a peak, as shown in Figure 2.18.
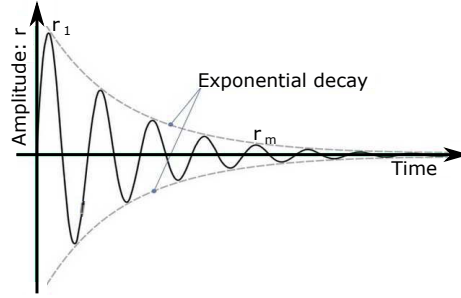
Figure 2.18: Estimation of logarithmic decrement.

However, if the scatter of peaks is too large to get reliable results from the logarithmic decrement, an alternative way of estimating the damping is to use exponential curve fitting of the peaks (Dep. of Structural Engineering, 2014):

$$\begin{aligned}
y_i &= \ln\left(r_{\mathrm{peak}}(t_i)\right) \\
&= \ln\left(r_0 e^{-\zeta\omega_n t_i}\right) \\
&= \ln\left(r_0\right) + \ln\left(e^{-\zeta\omega_n t_i}\right) \\
&= A - B \cdot t_i
\end{aligned} \tag{2.25}$$

The slope, B, in Equation 2.25 may be obtained by curve fitting, and the damping ratio is then given by:

$$\zeta_n = \frac{B}{\omega_n} \tag{2.26}$$

2.8 Frequency domain analysis

2.8.1 Discrete Fourier transform

Throughout this thesis, the fast Fourier transform (FFT) will be used to express time signals in the frequency domain. The FFT is an algorithm to compute the discrete Fourier transform (DFT) in a fast and efficient way. Therefore, it is of essence to understand how the DFT is established, and how it may be useful in data acquisition and treatment. This chapter will explain the background theory of the DFT.

A random time domain record of acceleration, $\ddot{r}$, may for instance be as Figure 2.19 shows.
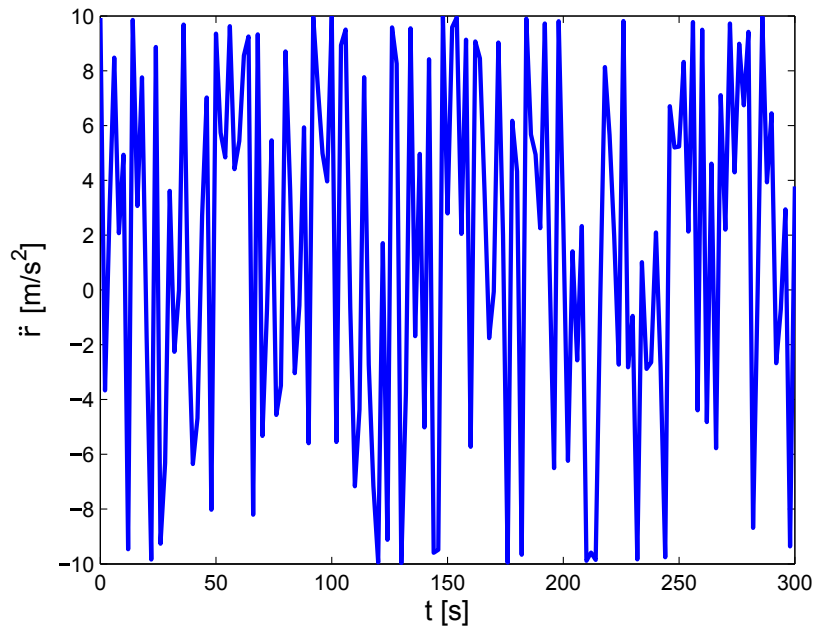
Figure 2.19: Random time-acceleration plot.

The following theory presented, about the Fourier transform, can be found in the book *Introduction to coastal engineering and management* (Kamphuis, 2010). The time signal of $\ddot{r}$ a can be expressed in terms of frequency, by the use of a Fourier series summation for each value $\ddot{r}_j$:

$$\ddot{r}_j = a_0 + \sum_{n=1}^{\infty} a_n cos(2\pi f_n t_j) + \sum_{n=1}^{\infty} b_n sin(2\pi f_n t_j) \tag{2.27}$$

where a_0, a_n and b_n are constants, and f_n is the frequency for the nth term.

By applying Euler's relationship: $e^{i\theta} = cos(\theta) + i \cdot sin(\theta)$ (θ being a random angle), Equation

2.27 can be re-written to:

$$\ddot{r}_j = \sum_{n=-\infty}^{\infty} C_n e^{i\left[2\pi(f_n t_j)\right]} \tag{2.28}$$

where C_n is a complex coefficient. Equation 2.28 is known as the DFT. Note that the limits in Equation 2.28 are infinite. The record of data, for instance the acceleration in Figure 2.19, are neither infinite nor continuous. The acceleration is sampled at N points, with ΔT as distance between each time-sample. This makes the frequency-domain likely as discontinuous, where the smallest frequency that can be defined is equal to $f_{\min} = \frac{1}{t_R}$, t_R being the length of the record.

The Nyquist frequency is an important definition, which defines the highest frequency that can be extracted from a data set, and is defined as:

$$f_N = \frac{1}{2\Delta t} = \frac{N}{2}\Delta f \tag{2.29}$$

where $\Delta f = \frac{1}{t_R}$, which is the lowest frequency increment possible, and $\Delta t = t_n \text{-} t_{n-1}$ is the time increment of the sampled data. Thus, Equation 2.28 may be slightly re-written, which results in the finite discrete Fourier transform (FDFT):

$$\ddot{r}_j = \sum_{n=-\frac{N}{2}+1}^{\frac{N}{2}} F_n e^{i\left[2\pi(f_n t_j)\right]} \tag{2.30}$$

In Equation 2.30, F_n is a complex frequency function with a useful property: $F_n = F_{-n}^*$ (i.e the complex conjugate of F_N is equal to F_N). This leads to another definition of the finite discrete Fourier transform, where the limits in the summation are re-written:

$$\ddot{r}_j = \sum_{n=0}^{N-1} F_n e^{i\left[2\pi(f_n t_j)\right]} \tag{2.31}$$

In practice, only positive, real valued frequencies are of interest, and only the frequencies lower than the Nyquist frequency can be defined. Therefore, Equation 2.31 can be re-written to (for the details of this derivation, see Kamphuis (2010)):

$$\ddot{r}_j = \sum_{n=0}^{N-1} |F_n| cos(2\pi f t - \theta_n)$$
$$= \sum_{n=0}^{N/2} 2|F_n| cos(2\pi f t - \theta_n) \qquad (2.32)$$
$$= \sum_{n=0}^{N/2} |A_n| cos(2\pi f t - \theta_n)$$

In Equation 2.32, θ_n is called the phase spectrum, and $|A_n|(=2|F_n|)$ is called the amplitude spectrum. By the use of Parseval's Theorem (Kamphuis, 2010), the variance at any frequency can be exressed as:

$$S(f_n)df = \frac{1}{2}|A_n|^2 \quad or \quad S(f_n) = \frac{1}{2df}|A_n|^2 \qquad (2.33)$$

where $S(f)$ is called the *spectral density function*. The spectral density function is then plotted against frequency, to be able to see which frequencies that occurs the most in a data set. An example of such a spectra will be shown in the next chapter.

The fast Fourier transform (FFT) is simply a faster algorithm than the finite DFT (see Equation 2.30), which reduces the number of computations needed for N points from $2N^2$, to $2N\lg_2(N)$, where $\lg_2$ is the base-2 logarithm (Weisstein, Eric W, 2015). For instance, for N=1000 points, the DFT needs $2\cdot1000^2=2\cdot10^6$ computations, while the FFT needs $2\cdot10^3\lg_2(10^3)$ $\approx 2\cdot10^4$ computations. As a result of the use of the base-2 logarithm, the N number of points used in the FFT, should preferrably be a power of two, to ensure the wanted speed of the transform.

2.8.2 Nyquist frequency and aliasing

Frequencies that exceed the Nyquist frequency (Equation 2.29) can be misinterpreted in the spectral analysis. The energy in these frequencies are superimposed in the spectrum by *aliasing*. The phenomenon is best explained by an example:

A wave of frequency 1.1Hz is sampled with Δt=1.0s. Figure 2.20 shows that the signal which is sampled with Δt=1.0s (red curve, with dotted points) has a frequency of 0.1Hz instead of the wanted 1.1Hz.
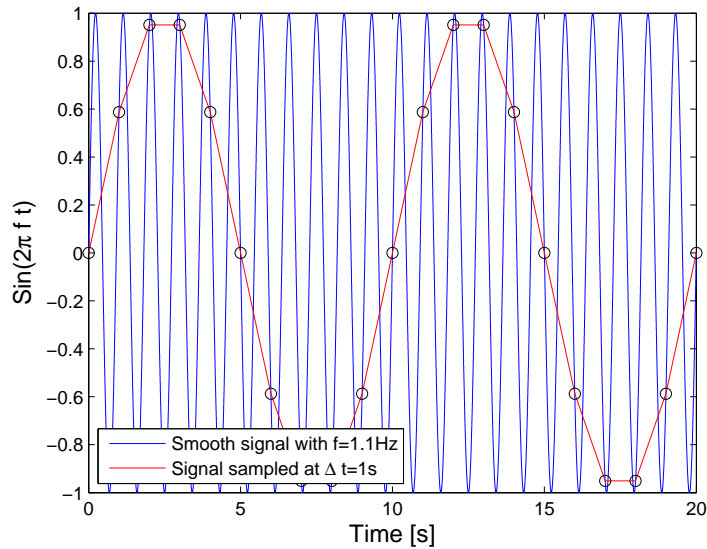
Figure 2.20: Aliasing example, too low sampling frequency.

To prevent aliasing, i.e obtaining non-present frequencies in the spectral density function, the sampling frequency should always exceed the Nyquist frequency. To get the wanted 1.1Hz, it is thus necassary to sample the data with $\Delta t \leq \frac{1}{(1.1 \cdot 2)\text{Hz}}$=0.45s. Figure 2.21 shows the result when the dataset is sampled at Δt=0.40s.
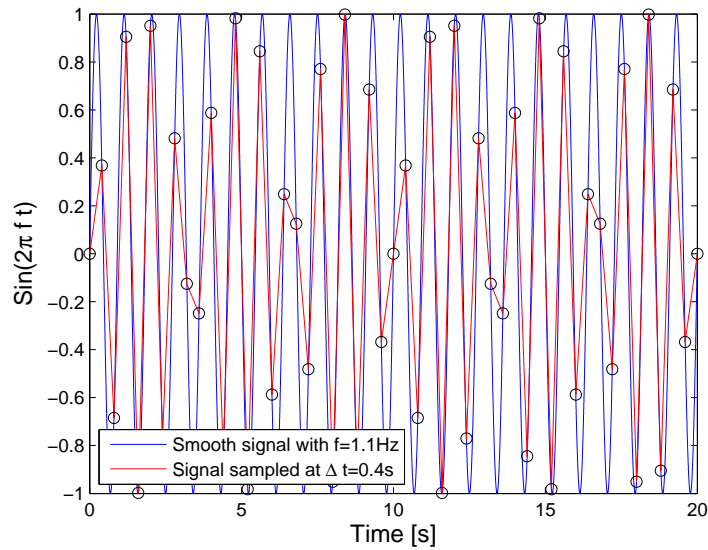
Figure 2.21: Aliasing example, enough sampling frequency.

It is not obvious that Figure 2.21 shows that the frequency of 1.1Hz can be obtained in a spectral analysis. Therefore, the spectral density function has been computed with the use of the FFT in Matlab$^®$ (The MathWorks Inc, 2015), for the data sampled at Δt=1s and Δt=0.4s. The latter is shown in Figure 2.22, and it clearly states the importance of the Nyquist frequency due to aliasing.
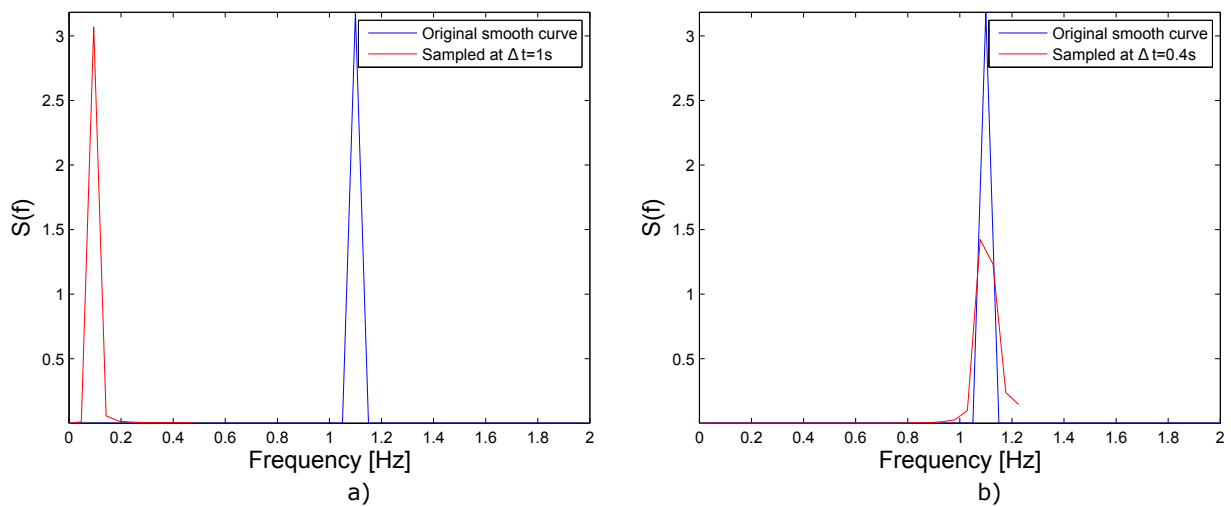
Figure 2.22: FFT of the two curves shown in a) Figure 2.20, b) Figure 2.21.

Figure 2.22 a) shows that if the wanted curve is sampled with too low frequency, aliasing may cause wrong estimations of the frequency-content in the data. In Figure 2.22 b), the data is sampled with a small enough time increment, such that the wanted frequency is obtained in the FFT-plot.

The method of extracting the frequency-content in a data set (which are shown in Figure 2.22) is based on the theory presented in Chapter 2.8.1, and how the FFT is applied can be found in the Mathworks Documentation (The MathWorks Inc, 2015). This method has been used to extract natural frequencies of the laboratory model.

2.9   Temperature and force dependency of a beam

The theory in this chapter can be found in a various number of mechanics textbooks, for instance in Hibbeler (2013). Hooke's law, for an elastic bar in one dimension, can be expressed as:

$$\sigma = E\epsilon = \frac{N}{A} \tag{2.34}$$

where σ is the stress [Pa], E is Young's modulus [Pa] and ϵ is the strain. N is the axial force through the bar [N], and A is the cross sectional area [m^2]. The strain may further be defined as percentage change of length of the bar, or as a function of the temperature expansion coefficient and the temperature change:

$$\epsilon = \frac{\Delta L}{L} = (\Delta T)\alpha \tag{2.35}$$

where α is the temperature expansion coefficient for the material [K^{-1}], and ΔT is the temperature change in the bar. By combining 2.34 Equation and 2.35, a relationship between force, length and temperature change may be obtained:

$$N = EA\epsilon = EA(\Delta T)\alpha \tag{2.36}$$

Equation 2.36 shows that the relationship between force and temperature in a bar is not dependent on the length of the bar. For linear elastic materials, with a constant temperature coefficient, the relationship between force and temperature develops linearly.

Chapter 3

Laboratory model

In this chapter, the laboratory setup, the test equipment, and the methods of measurement related to the laboratory model are explained.

The laboratory model consists of two spans, each with a length of approximately 15m. The model is a combination of system 25 which are related to the contact wire, messenger wire and droppers, and system 20 which relates to the support (for details about the two systems, see (Jernbanekompetanse, 2014)). The model is built without stitch wire, which makes it even less comparable to system 20 or 25 as single systems. Each end of both the contact and messenger wire are connected to two cantilevered beams, which are supported by external wires connected to the wall. The support in the middle consists of a top anchor, cantilever tube, registration arm, registration arm dropper and a steady arm (identical to Figure 2.11). A 3D view of the model is given in Figure 3.1.

A horizontal cut of the system is shown in Figure 3.2. As Figure 3.1 and Figure 3.2 shows, the system contains four droppers, which throughout this thesis are named dropper 1-4. On the right side of the system, jacks are mounted on the contact and messenger wire. The jacks are used to create tension in both the contact and messenger wire, and are fastened with steel chains. On the left side of the system, sensors are connected to the contact and messenger wire to measure how much tension that is applied in the wires.
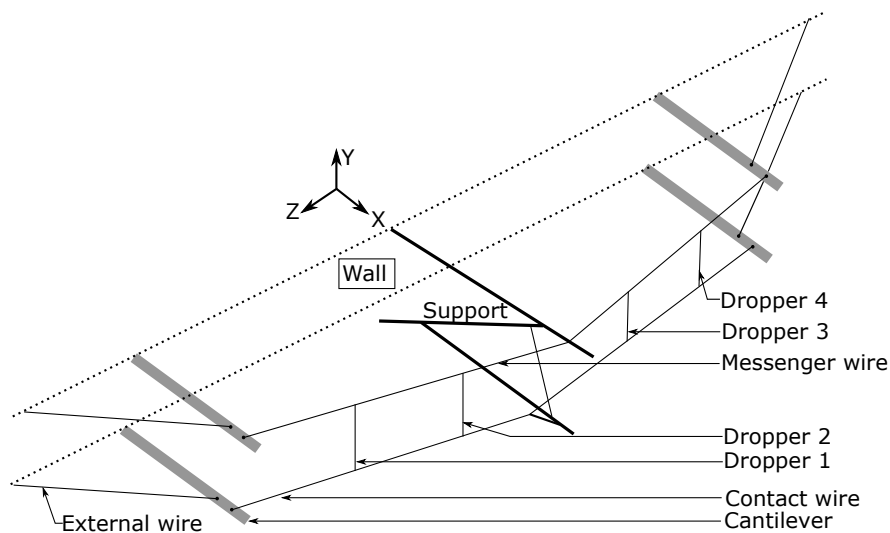
Figure 3.1: Laboratory model, 3D view.
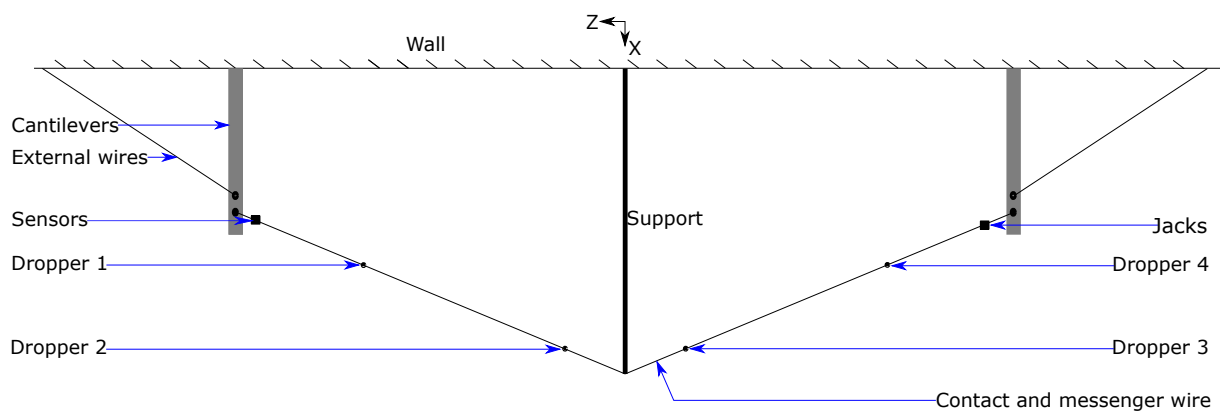
Figure 3.2: Top view of laboratory model.

3.1 Geometry

The initial geometry was measured when the system was slack, i.e there was not applied tension in the contact or messenger wire. The different distances were measured with laser, which had an accuracy of millimeters. Figure 3.3 shows the system from a vertical cut, where the slack measurements are included. In the following figures, 3.3-3.7, the measurements are given in meters.
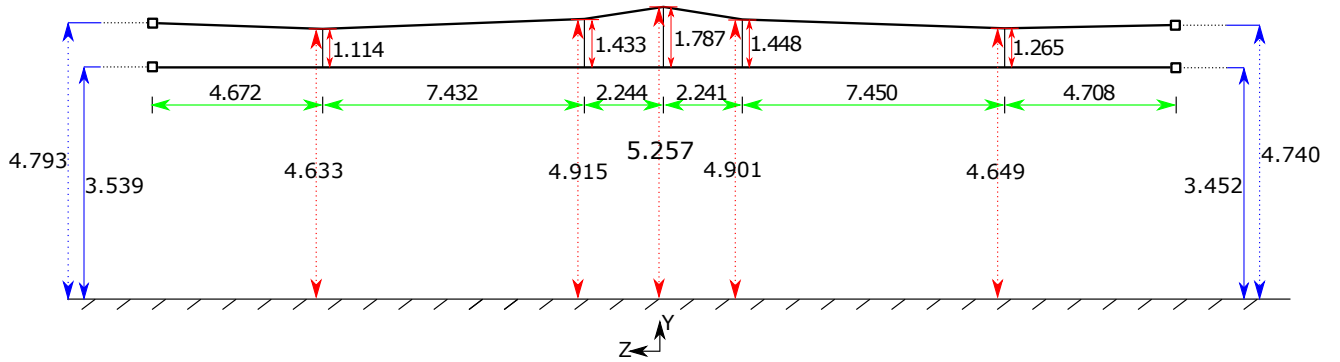
Figure 3.3: Sideview of the laboratory model, distances measured center-to-center.

Note the coordinate system used in Figure 3.3. This coordinate system will be used as global coordinates throughout the thesis. The positive x-axis are pointing out of yz-plane, due to the right-hand rule. The measured values in Figure 3.3 have been edited to represent center-to-center distances between the components. Because of this, all the geometric measurements shown in this chapter will relate to distances center-to-center of the components.

The solid-drawn and dotted blue lines in Figure 3.3 marks the distance from the floor to the cantilevers, at their respective midpoints. The dotted red lines marks the distance from the floor to the midpoint of the messenger wire, where the droppers are connected. The dropper height is measured from the midpoint of contact wire to the midpoint of messenger wire, and is marked with solid-drawn red lines.

The green horizontal lines shows the distance between the midpoints of the cantilevers, droppers, and to the point where the contact/messenger wire is connected to the support. The latter is further emphasized in Figure 3.4.
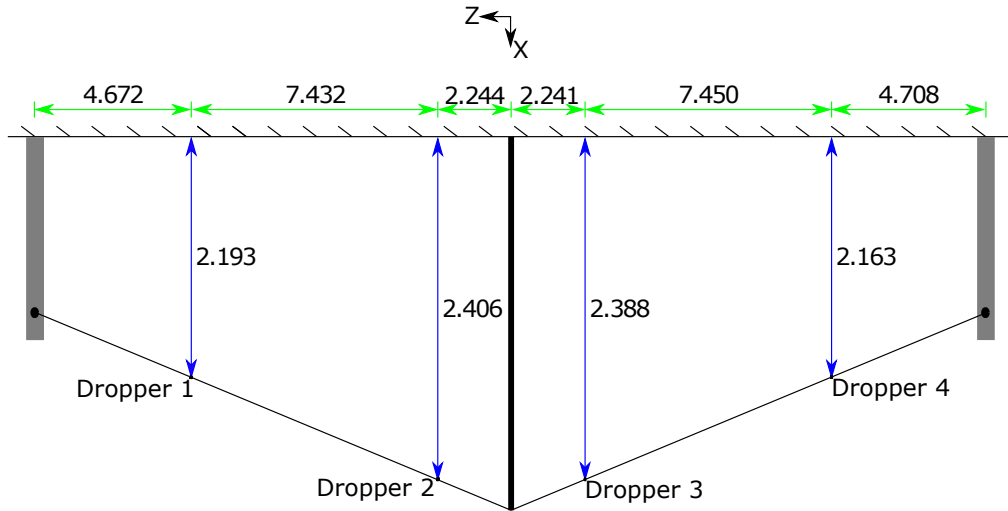
Figure 3.4: Top view of the laboratory model, where the blue arrows represent the distance from the droppers to the wall. Distances measured center-to-center or center to wall.

Figure 3.4 shows the same as Figure 3.3, but in the xz-plane. It primarily shows the distances from each dropper to the wall, which are marked with the solid-drawn blue lines. The measurements of the cantilevers are not included since it may include ambiguity due to the horizontal cut. The geometry of the cantilevers are therefore presented in Figure 3.5.
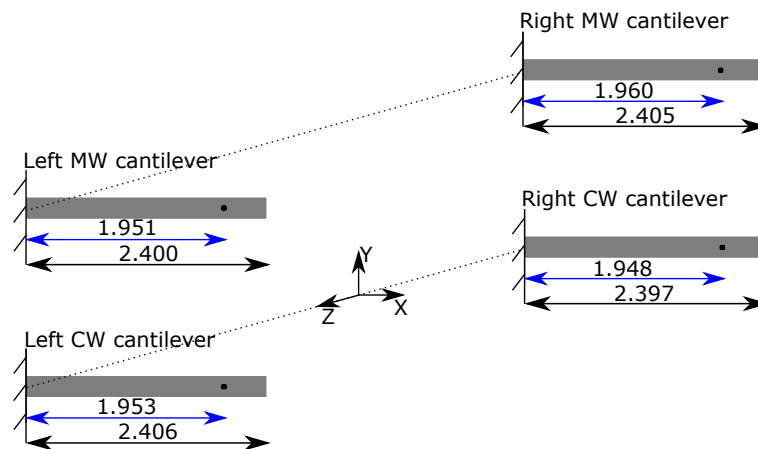
Figure 3.5: Length of the cantilevers, and distance from the wall to the connection of the contact and messenger wire.

In Figure 3.5, the blue lines represent the distance from the wall to the center of the contact or messenger wire. The black lines shows the total length of each cantilever. It should be mentioned that the cross section of the 'Right CW cantilever' (see Figure 3.5) is rotated 90 degrees in the laboratory setup, which for future setups should be edited to the same position as the other cantilevers. The geometry of the external wires connected to the cantilevers are shown in Figure 3.6.
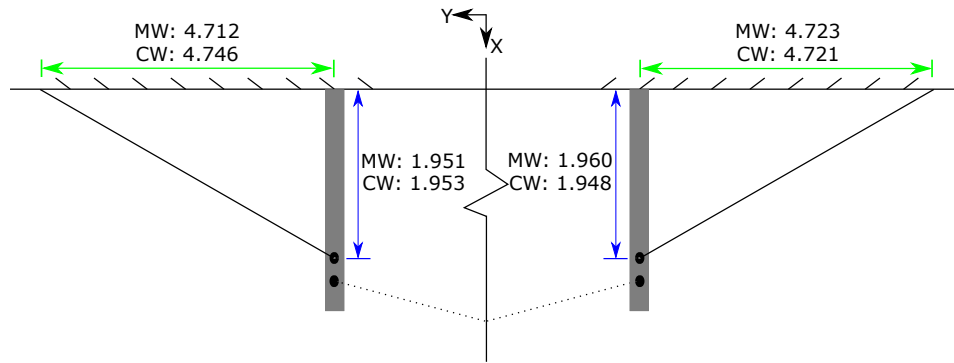
Figure 3.6: Wires connected to the cantilevers, distances measured center-to-center.

To avoid ambiguities when interpreting Figure 3.6, each of the distances shown are marked either as MW or as CW. MW is related to the wires connected to the same cantilever as the messenger wire, and CW is related to the wires connected to the same cantilever as the contact wire. Note that this way of referring to the contact and messenger wire (CW and MW, respectively) will happen regularly throughout this thesis.

The geometry of the support is shown in Figure 3.7.
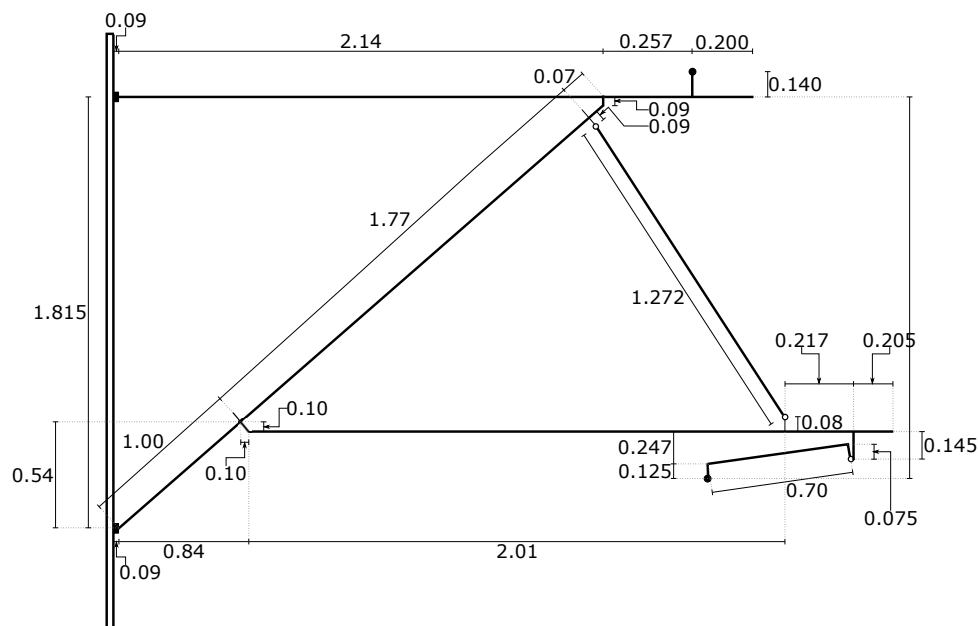
Figure 3.7: Geometry of support, distances measured center-to-center.

3.2   Materials

As mentioned, the original setup in the laboratory was a combination of System 20 and System 25. The material data used in the laboratory setup is given in Table 3.1 and 3.2.

Table 3.1: Material data for wires used in the laboratory (System 25) (NKTCables, 2008), (Jernbanekompetanse, 2014).

Component	Type	Density [N/m]	Diameter [mm]	Area (effective) [mm^2]	E [GPa]	ν
Messenger wire	Bz ‖ 70/19	5.96	10.5	65.81	120	0.34
External wires[1]	Bz ‖ 70/19	5.96	10.5	65.81	120	0.34
Contact wire[2]	RiS 120 CuAg	10.70	13.20	120.00	120	0.34
Dropper	Bz ‖ 10/49	0.89	4.50	9.62	120	0.34

In Table 3.1, E is the youngs modulus, and ν is the Poisson's ratio.

Table 3.2: Material data for support (System 20)

Component	Material	Profile	Area [mm^2]	Thickness [mm]	Width x height [mm x mm]
Top anchor	Aluminium[3]	Pipe	990.4	6.5	-
Cantilever tube	Aluminium	Pipe	990.4	6.5	-
Registration arm	Aluminium	Pipe	477.5	4.0	-
Registration arm dropper	Steel[4]	Circular	28.3	6.0	-
Steady arm	Aluminium	Rectangle	325	-	13 x 25

The data given in Table 3.2 are obtained from drawings created by the Norwegian National Rail Administration, Jernbaneverket (HMH, 1992). Two important material specifications have not been mentioned in Table 3.1 or 3.2, which are:

- The cantilevers at the each end of the contact and messenger wire are made of aluminum. The cross sectional properties for the cantilevers are given in Appendix B.1.

- The thermal expansion coefficient for the contact wire and the messenger wire is: $\alpha=17\cdot10^{-6}$ (NKTCables, 2008).

---

[1] Wires connected to the cantilevers at each end of the system, which are of the same type as the messenger wire.

[2] Specific data for the contact wire cross section is given in Appendix B.2.

[3] Material data for aluminium: Youngs modulus: 70GPa, density: 2700kg/m^3 and Poissons ratio: 0.35.

[4] Material data for steel: Youngs modulus: 210GPa, density: 7800kg/m^3, Poissons ratio: 0.3.

Note that in Table 3.1, the diameter of the wires does not correspend to their respective effective area. The messenger wire and the droppers both consists of a set of wires twirled together (stranded wires). Figure 3.8 shows the correct cross sections of the dropper and messenger wire.
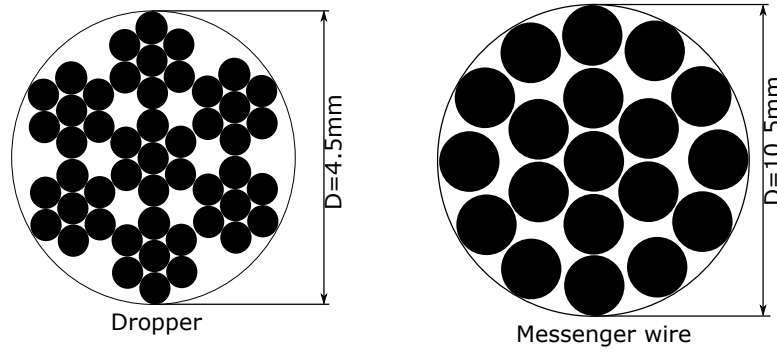
Figure 3.8: Dropper and messenger wire cross section

The droppers consist of 49 twirled wires, each with a diameter of 0.5mm, and the messenger wire consist of 19 twirled wires, where the diameter of each wire is 2.1mm.

The contact wire does neither have a perfect circular cross section. It grooves in the side, to enable the fastening of the droppers. The geometry of the contact wires cross section is shown in Figure 3.9.
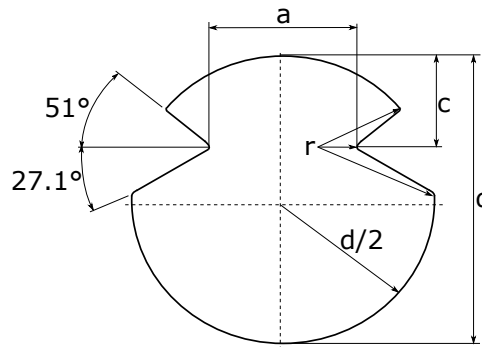
Figure 3.9: Contact wire cross section (not in scale).

In Figure 3.9, a=5.16mm, d=13.2mm, c=4.0mm, and r=0.4mm (Kiessling et al., 2009). The cross sectional properties for the contact wire, that are shown in Appendix B.2, have been computed by PhD candidate at Department of Structural Engineering, Petter Røe Nåvik.

3.3   Connections

3.3.1   Support

The support used in the laboratory is shown in Figure 3.10, and the names of the main components are included.
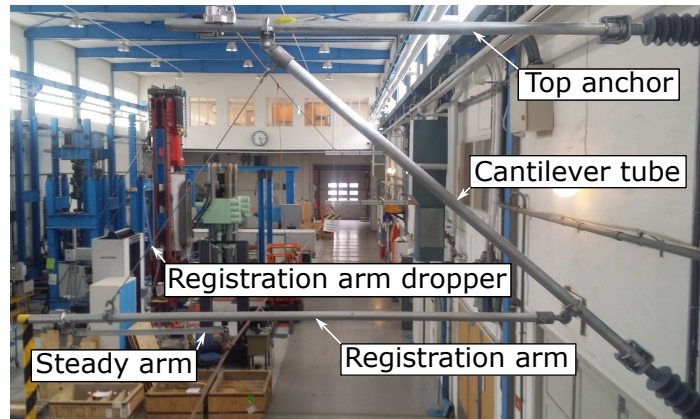
Figure 3.10: Support in the laboratory.

The components at the support are connected with different types of connections, which will be shown and explained subsequently. How the contact wire is attached to the steady arm is shown in Figure 3.11.

Figure 3.11: Connection between steady arm and contact wire.

As seen in Figure 3.11, the contact wire is connected with a clamped connection to the steady arm. This is done with the use of a groove stud at the end of the steady arm, which is attached to the contact wire by the use of a U-pin (Kiessling et al., 2009).

The steady arm is connected to the registration arm as Figure 3.12 shows. The part of the connection that is bolted to the registration arm is called a drop bracket (Kiessling et al., 2009). The drop bracket ensures an important feature related to the movement of the steady arm. Note the red circle in Figure 3.12: This part is created to unable the steady arm to come in contact with the registration arm, as the train passes. If the steady arm is elevated high enough, the drop bracket will unable the contact between the the registration arm and the steady arm, and instead force both components to elevate simultaneously.
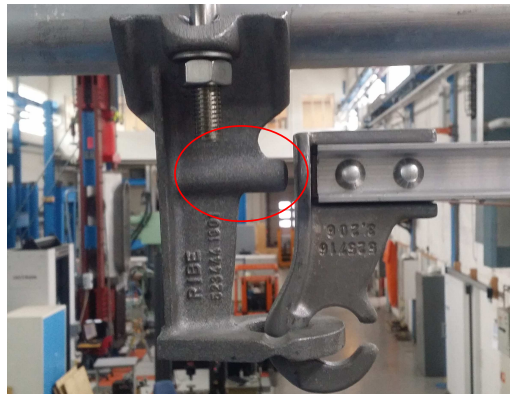
Figure 3.12: Connection between steady arm and registration arm.

How the registration arm dropper is connected to a) the registration arm, and b) to the cantilever tube, is showed in Figure 3.13. This connection is made by the use of a hook clip, which is bolted to the registration arm and the cantilever tube, and the registration arm dropper is attached in both ends with the use of a thimble.
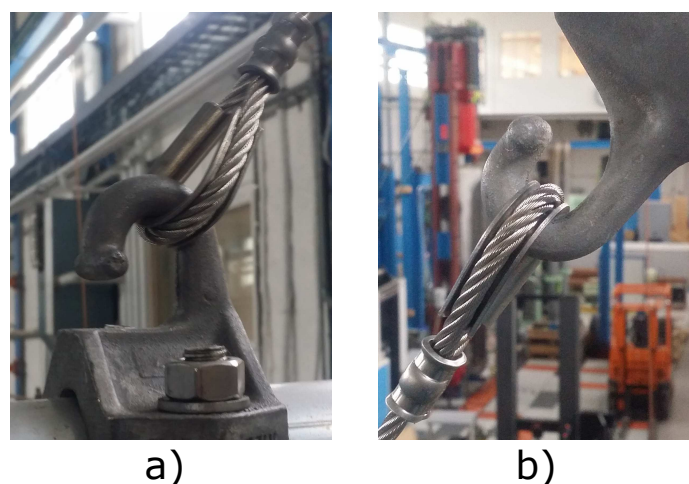
Figure 3.13: Registration arm dropper connected to a) Registration arm, b) cantilever tube.

The registration arm is connected to the cantilever tube with the use of a combination of a hook end clipping, and an eye clamp. As seen in Figure 3.14, the hook end clipping goes through the eye clamp, which makes the registration arm more or less free to rotate in all directions except rotation about its own longitudinal axis (torsional rotation). A free rotational connection is preferable, both due to movement in the longitudinal (along track) and vertical direction. The free rotation enables the registration arm to rotate vertically, which may happen if the steady-arm is elevated high enough.
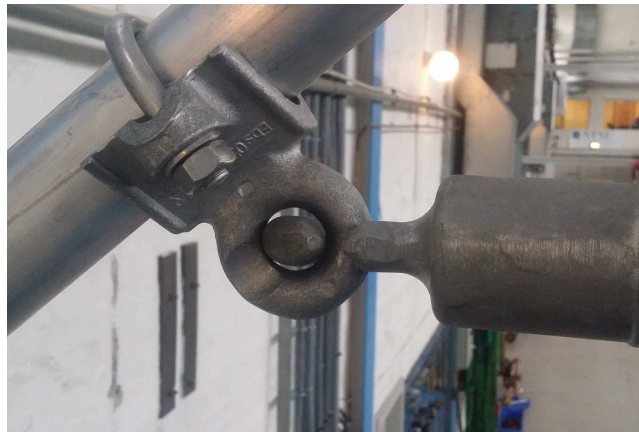
Figure 3.14: Registration arm connected to the cantilever tube.

A clevis end fitting is used to connect the cantilever tube to the top anchor. The clevis end fitting works as a hinge, which enables the cantilever tube to rotate in the vertical direction, as Figure 3.15 shows.

Figure 3.15: Cantilever tube connected to the top anchor.

The messenger wire is connected to the top anchor as Figure 3.16 shows, which is called a messenger wire support clamp (Kiessling et al., 2009). This design of this connection is primarily created to keep the messenger wire from slipping off the support and fall down on the ground, and to transfer the vertical load obtained from the self-weight of the messenger wire, contact wire and the droppers to the support.

It may not be obvious by looking at Figure 3.16, but the messenger wire is supposed to be able to move in the longitudinal direction (along track), which may occur due to temperature changes.
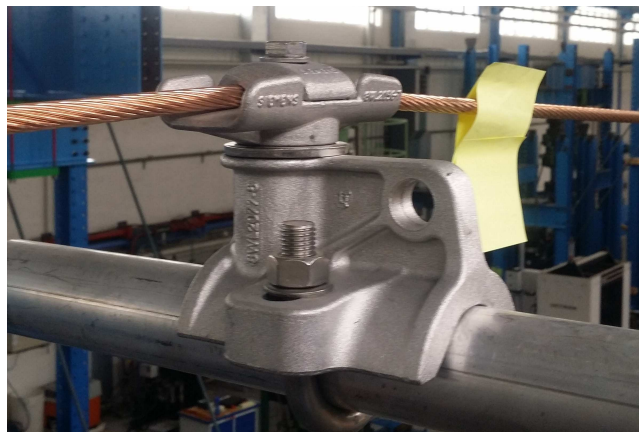
Figure 3.16: Messenger wire connected to the top anchor.

Finally, the cantilever tube and the top anchor are connected to the wall as Figure 3.17 shows. Only the connection of the top anchor is showed, since the connection of the cantilever tube is identical.

Figure 3.17: Top anchor connected to the wall.

Close to the connection to the wall, an insulating sheat are covering the top anchor and the cantilever tube. This insulator can either be made of porcelain, plastic or composites (Kiessling et al., 2009).

3.3.2 Wires and cantilevers

The jacks that was installed to create tension in the contact and messenger wire are showed in Figure 3.18.

Figure 3.18: a) Jack, b) steel chain connecting the jack to the contact wire.

By the use of the jacks, the system has a maximum capability of achieving up to approximately 15kN tension in both the contact and messenger wire. The length of the steel wire chain is approximately 1m, depending on how much tension that is applied in the wires.

The droppers are connected to the contact and messenger wire as shown in Figure 3.19.
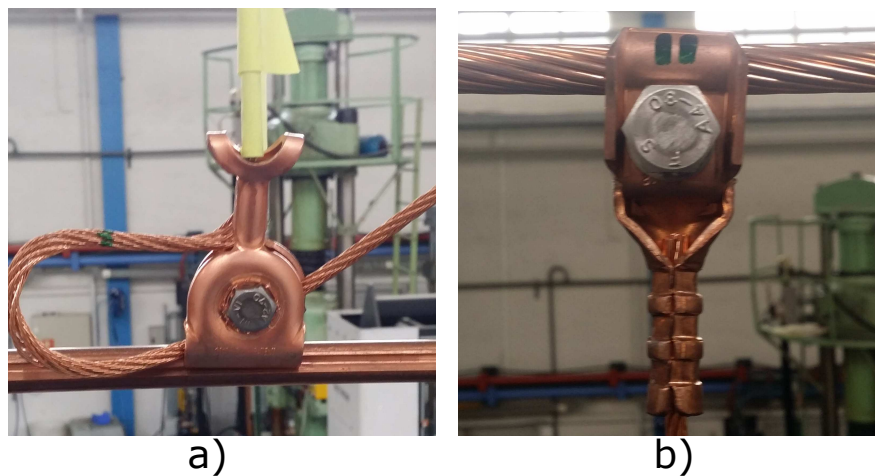
Figure 3.19: a) Dropper connected contact wire, b) dropper connected to messenger wire.

Note that the droppers are connected differently to the contact and messenger wire, due to the passing of the train. This also emphasizes the primary reason for the crosse sectional geometry of the contact wire. It is essential to connect the droppers in a way that they do not interfere with the passing of the train, which is ensured by the bolted clamp showed in Figure 3.19 a). Also note that in Figure 3.19 a), the end of the dropper is not ensured a secure fastening. Preferably, this end piece should be fastened to the nut, to secure the dropper

from being disconnected from the contact wire. As seen in Figure 3.19 b), the dropper is ensured a secure fastening to the messenger wire.

The external wires, which are connected to the cantilevers in each end of the model (see Figure 3.2), are showed in Figure 3.20.
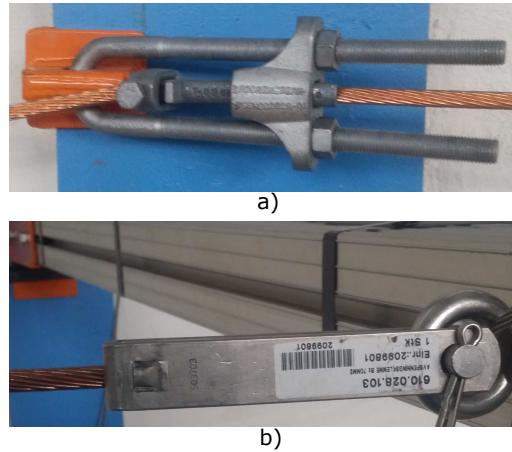
Figure 3.20: External wire connected to a) the wall, b) a cantilever.

Figure 3.20 a) clearly emphasizes that the external wires are introduced for one sole purpose, which is to support the cantilevers in the longitudinal direction, and to transfer the tension applied in the contact and messenger wire to the wall.

The last connection worth mentioning is showed in Figure 3.21, which shows how the cantilevers are connected to the wall.
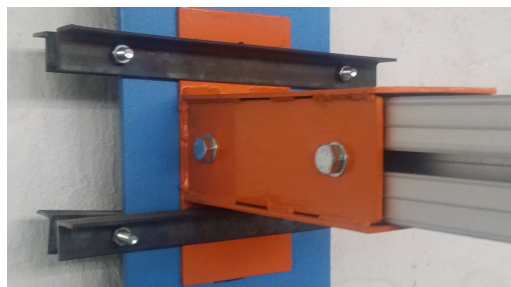
Figure 3.21: Cantilever connected to the wall.

The connection shown in Figure 3.21 is designed to make it easy to adjust the height of the cantilever, which can be done by loosing bolts connected to the steel L-profiles.

3.4 Test equipment

The equipment used to perform measurements on the laboratory model are introduced in this chapter. A general setup for modal hammer dynamic tests is showed in Figure 3.22.
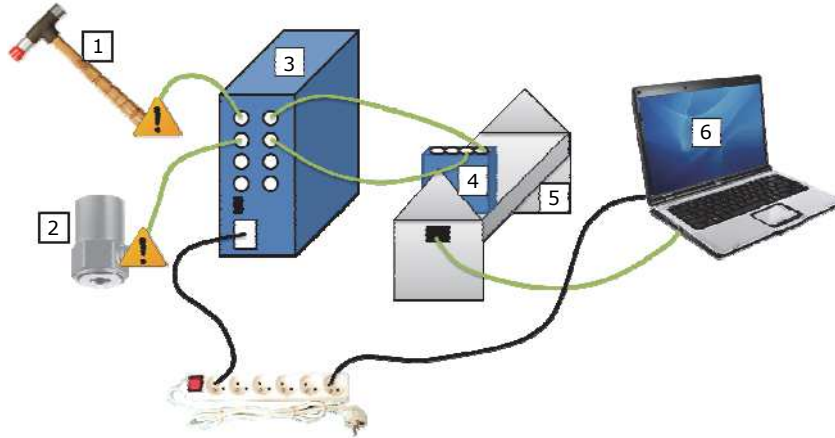
Figure 3.22: Example of modal hammer dynamics equipment setup (Labonnote, 2012). The legends 1-6 are: 1: Modal hammer, 2: Accelerometer, 3: Power supply/signal conditioner, 4: NI dynamic module, 5: NI chassis, 6: Laptop.

Since the modal hammer has not been used in any of the measurements performed in this thesis, it will not be explained any further. For further details about the modal hammer, see *Modal dynamics for dummies* (Labonnote, 2012).

The accelerometer used is showed in Figure 3.23. This type of accelerometer has very small strain sensitivity, which makes it appropriate to use on extremely flexible structures.
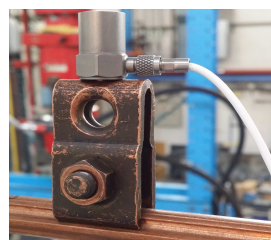
a)   b)

Figure 3.23: a)Accelerometer, Kistler type 8770A (Kistler, 2014), b) Accelerometer connected to the contact wire, in the laboratory model.

The accelerometer was mounted on the contact wire with the use of a bolted clamp similar to the one that was used to connect the dropper to the contact wire. The accelerometer had a restriction of measuring magnitude of acceleration, which means that it could not measure acceleration in three dimensions. Optimally, the accelerometer should have been mounted

as vertically aligned as possible, to measure vertical acceleration accurately. The latter was however not possible, due to skewness in the contact wire.

The signal cable attached to the accelerometer (see Figure 3.23 b)) was connected to the power supply/signal conditioner, which was further wired to the NI dynamic module. The signal cable is very fragile, and should be treated carefully, since it easily can be damaged.

The NI dynamic module was mounted inside the NI chassis, and both components are shown in Figure 3.24.

Figure 3.24: a) Power supply/signal conditioner, Kistler Type 5134 (Labonnote, 2012), b) NI dynamic module mounted inside NI chassis type cDAQ-9174 (National Instruments, 2015).

The NI dynamic modules main function is to digitize the signal obtained from the accelerometer. It has four input channels, which can digitize signals at rates up to 51200 Hz per channel, and it contains anti-aliasing filters (Labonnote, 2012). After the signal is digitized, it is sent to a computer where it is processed with the use of Matlab. In Matlab, the data acquired (magnitude of acceleration) can be treated to find both natural frequencies and damping ratios, which will be further explained in Chapter 3.5.

The sensors used to measure tension contact and messenger wire are shown in Figure 3.25.
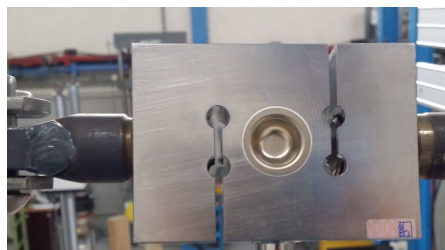
Figure 3.25: Sensor used to measure tension in the contact and messenger wire.

3.5   Methods of measurement

This chapter includes the methods of how to perform measurements in the laboratory, and how to treat the acquired data from these measurements. The objective with the measurements was primarily to gain data to use in the validation of the finite element model, but is was also of interest to investigate how the system responded to different tensions in the contact and messenger wire, and to determine how the laboratory model was behaving in relation to existing OCLs. In general, three tests were made:

Test 1:   Exciting the first expected *vertical* natural frequency of the model.

Test 2:   Exciting the second expected *vertical* natural frequency.

Test 3:   Measure the elasticity-variation along the span.

Test 1 and test 2 may also be referred to as *free decay tests* or as *free decay measurements*. This is because the model was set into motion, and the measurements were done on the free vibrations of the model, after the load was removed.

In addition, both test 1 and 2 were done with two different system configurations. The first configuration included the entire laboratory model, as shown in Figure 3.1, and in the other configuration dropper 2 was removed (see Figure 3.2 for dropper specification). The measurements without dropper 2 present in the model was done for two reasons. First of all it was done to gain more results to compare with the numerical model. The other reason was due to the lack of research that has been carried out on missing droppers related to catenary systems. As mentioned in Massat et al. (2006), missing droppers should be further looked into, to see how it affects the behavior of catenary systems.

3.5.1 Free decay

For the tests where the system was excited into its expected first and second vertical natural frequency, the accelerometer was mounted between dropper 1 and dropper 2, which is shown in Figure 3.26.
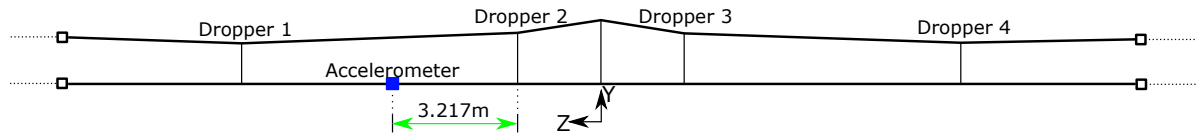
Figure 3.26: Position of the accelerometer, measurement shown along the contact wire.

The idea behind these tests was to physically force the system into its first two vertical natural frequencies, by applying an initial harmonic load, prior to the registration in the accelerometer was initiated. The harmonic load was manually applied by a person, who shook the system as steadily as possible.

In the first test, the contact wire was excited at its connection to the steadty arm, forcing the model into the shape as shown in Figure 3.27. This shape resembles the mode of the first expected vertical natural frequency. It is similar to the shape of the first natural frequency of a uniform denisty wire (Chopra, 2007), since it resembles a half-sine deflection along the entire model.
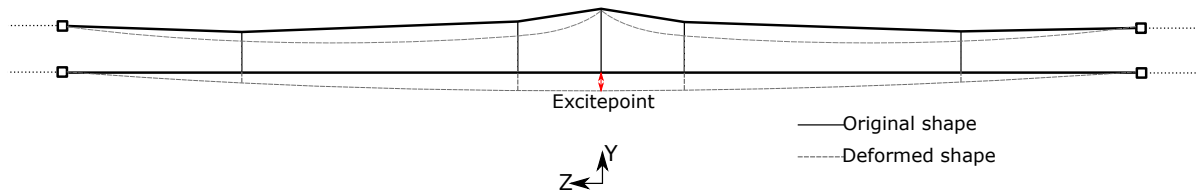
Figure 3.27: Test 1: First expected vertical mode shape, manually excited.

In the second test, the contact wire was excited in the same point as the accelerometer was mounted. This is shown in Figure 3.28, which was supposed to represent the expected second vertical natural frequency. Also in test 2, the mode shape looked similar to the second mode of a uniform density wire, taking the shape as a full-sine deflection along the model.
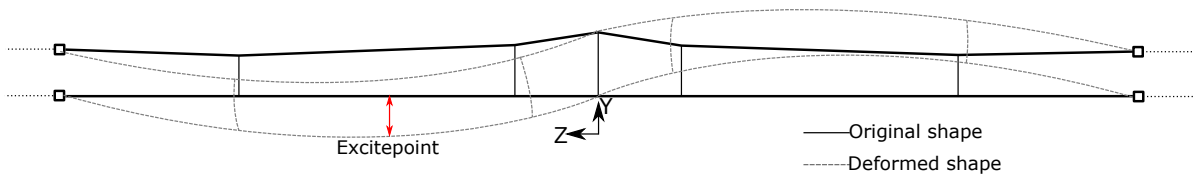
Figure 3.28: Test 2: Second expected vertical mode shape, manually excited.

For both test 1 and test 2, the contact wire was set in motion by exciting it for a few seconds, until it felt like the model was shaking in the appurtenant frequency of each wanted mode shape. When the person responsible for exciting the contact wire, and the person responsible for running the analysis on the computer, agreed that the vibration of the model looked like the wanted shape, the registration in the accelerometer begun. Initially, the measurements were done with a one minute window. Since results showed that the system had very small damping, all the measurements was re-done with a four minute window. In total, it was done 100 free decay measurements, where five different tension-combinations in the contact and messenger wire were used:

- CW-7.1kN - MW-7.1kN (Common for Norwegian system 35).

- CW-7.1kN - MW-10kN (Used to include different tension in the two wires).

- CW-10kN - MW-7.1kN (Used to include different tension in the two wires).

- CW-10kN - MW-10kN (common for Norwegian system 20B).

- CW-15kN - MW-15kN (common for Norwegian system 25).

This way of referring to a tension-combination will be used frequently throughout this the-sis: CW-xxkN - MW-yykN means that the contact wire is applied xx kN tension, and the messenger wire is applied yy kN tension. For each of the five tension-combinations, the following four measurements were done:

- First vertical natural frequency

  1. All droppers included.

  2. Dropper 2 removed.

- Second vertical natural frequency

  3. All droppers included.

  4. Dropper 2 removed.

Finally, each of the four mentioned measurements were done five times to secure more accurate results. An example of a specific measurement may explain the procedure better. For instance, one measurement could be defined as follows:

- *Tension*: CW-10kN - MW-10kN.

- *System configuration*: All droppers included.

- *Wanted shape/frequency*: First.

  → Five measurement were done for the three specifications given.

→ Since there in total were five tension-combinations, two system configurations and two wanted natural frequencies, a total of 100 measurements were performed.

The measurements were done with a sampling frequency of 2048Hz. This means that the acceleration was registered every $4.88 \cdot 10^{-4}$s, which is a rather high sampling rate in relation to the frequencies of interest. The latter was known due to earlier studies made on the model (Valle, 2014).

Since the FFT was meant to be used on the acquired data, it was necessary to sample N points, with N being equal to a of power 2 (see Chapter 2.8.1). This is the reason for choosing 2048Hz instead of for instance 2000Hz, as sampling rate. With the sampling rate specified, frequencies up to 1024Hz could be determined accurately (Nyquist frequency, see Chapter 2.8.2), and the risk of aliasing was thus most likely excluded.

In the subsequent part of this chapter, the methods of treating the aquired data from the laboratory measurements will be explained.

Extraction of natural frequencies

The results obtained after each measurement in the laboratory was a time-acceleration plot. An example of the output from a measurement is shown in Figure 3.29.
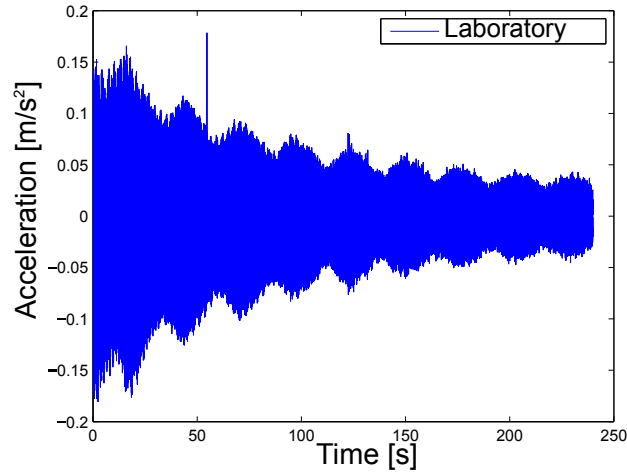
Figure 3.29: CW-10kN - MW-10kN, first vertical natural frequency, all droppers included.

Finding the natural frequencies from the time-acceleration plot was done by the use of the FFT, which background theory was described in Chapter 2.8.1 and 2.8.2. Continuing with the example in Figure 3.29, the FFT returned the spectra shown in Figure 3.30, which interval on the x-axis was re-sampled to include frequencies up to 25Hz. This was done since the natural frequencies of interest was expected to be below 25Hz, due to earlier studies (Valle, 2014).
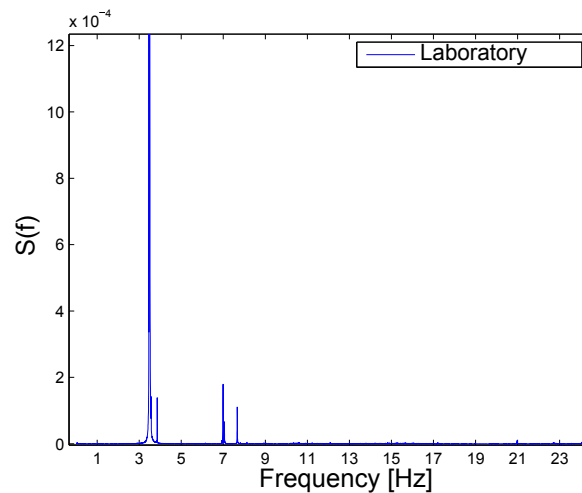
Figure 3.30: FFT spectra of the same data as shown in Figure 3.29.

From the FFT spectra, it was possible to extract the frequencies of interest. Most likely, for both the first and the second vertical mode shape, this related to the highest peak in the

spectra, which were the values extracted for all the measurements made. The latter statement will be validated by the use of the finite element model, in Chapter 6.2.

Damping extraction

In addition to the extraction of the natural frequencies, the damping of the first two vertical modes were also attempted to estimate. Initially, logarithmic decrement was meant to be used as measurement of damping. However, since the scatter of data measured was very dense, due too the high sampling rate, the damping was measured by exponentially curve fitting the peaks in the dataset, as Equation 2.25 describes. This was done by finding all the positive peaks in the time-acceleration plot, as seen in Figure 3.31.
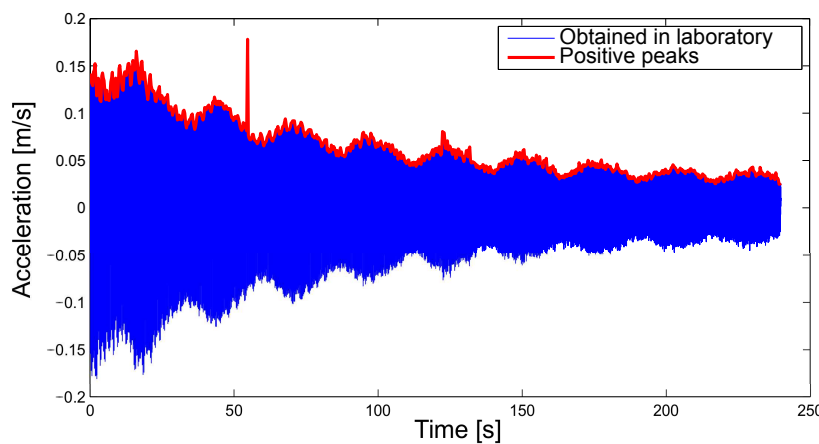
Figure 3.31: Same plot as shown in Figure 3.29, with positive peaks marked with red.

To estimate the damping from the peaks shown in Figure 3.31, Equation 2.25 was used for three different intervals in each measurement:

1. Application to the entire time series.

2. Application to the first half of the time series.

3. Application to the second half of the time series.

An example of the exponential fit generated is shown in Figure 3.32, which data originate from the same tension-combination as in Figure 3.29.

As mentioned in Chapter 2.7, the damping ratio could be estimated by finding the magnitude of the slope of the fitted curves (see Equation 2.26). The advantage of using the method described, is that if abrupt distortions are present in the measurements, it does not contribute to wrong calculation, as long as the distortions does not occur too frequently. For instance,
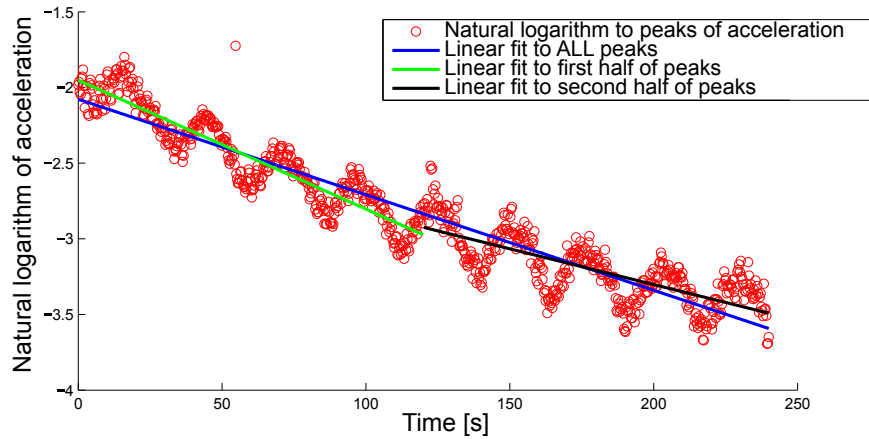
Figure 3.32: Scatter of natural logarithm of peaks, and linear fits tho the scatter-points.

the distorted value shown in Figure 3.31 (when $t \approx 50$s) will only contribute to a single point in the logarithmic plot. As the scatter of data is rather dense, this single distorted point will not have much affect on the linear fit. Thus, as long as the acceleration is not too distorted, the method of estimation of damping should be applicable.

The reason for dividing the calculation of damping in the three different intervals explained is because the excitement of the system in the laboratory was inconsistent. For many of the measurements, the vibration of the system went out of the wanted mode shape some time into the measurement. The phenomenon was physically observed by looking at the vibrating shape during the free vibration of the model. This was especially the case when exciting the system into the second vertical mode shape (see Figure 3.28). Thus, when the damping of the second vertical mode shape is considered, the values obtained for the first half of the data set are the most trustworthy values, since they most likely are related to the correct vibrating shape.

3.5.2 Elasticity along span

As mentioned in Chapter 2.1.2, it is common to plot the elasticity-variation along the span of OCLs. This chapter will go through the method used to measure the elasticity along the span of the laboratory model.

The procedure of how to measure the variation of elasticity was based on the relationship between elasticity, force and displacement, which is explained by Equation 2.1. By the use of a dynamometer and a laser, and physically excite the contact wire vertically in several points along the span, the vertical displacement for a given applied force could be measured. This would give the elasticity in displacement per force. The dynamometer used is shown in Figure 3.33.

Figure 3.33: Dynamometer used to measure elasticity (Pesola (2008)).

The procedure was performed by two persons, where one person excited the contact wire, while the other person measured the deflection with the laser.

By doing the measurements this way, the elasticity relates to a local elasticity in each of the measured points, in the vertical direction. Hence, by measuring the deflection in one point for a given applied force, the resulting elasticity will only be valid for that particular point. Since the elasticity is expected to take lower values in the position of the droppers and the cantilevers, at least one point between these components was essential to include, to get a good representation of the elasticity-variation. The points used in this procedure are showed in Figure 3.34.
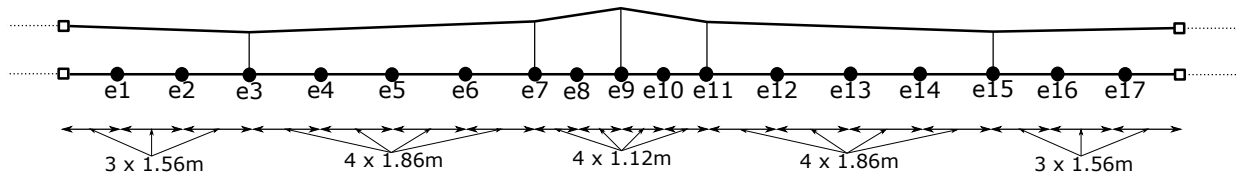
Figure 3.34: Points used to measure elasticity along the laboratory model, with measurements included along the contact wire.

The distances shown in Figure 3.34 are center-to-center measurements, along the contact wire. In each of the points e1-e17, the contact wire was excited with a vertical, downward, force equal to 5.0kg, which approximately corresponds to 49.1N (gravitational acceleration set to g=9.81m/s^2).

Chapter 4

Finite element modelling

This chapter involves the modelling of the laboratory system in Abaqus/CAE, and the method used to reconstruct the free decay measurements performed in the laboratory.

The modelling was performed by a combination of: Creating a Python script to use as input, and *manual modelling* with the use of the Abaqus/CAE GUI (Graphical User Interface).

This chapter is thus split in two parts. The first part (Chapter 4.1) relates to the Python scripting of the geometry and materials included, while the second part includes the modelling choices made to create the numerical model (Chapter 4.2), and the method (Chapter 4.3) used to reconstruct the free decay measurements explained in Chapter 3.5.

4.1   Python script

The main purpose of creating a Python script of the model was to be able to make changes in the physical model, and implement these changes in a fast and efficient way in the numerical model. These changes were primarily related to geometry or material definitions. The laboratory model was, as mentioned in Chapter 3, a combination of the norwegian system 20 and system 25. In the future, it is desirable to change the components of the model, to make it resemble either a complete System 20 or 25. The creation of the script may thus increase the efficiency of the modelling, since its purpose is to avoid using the Abaqus/CAE GUI to change material and geometric values manually. Instead, it would be possible to type the new coordinates and material definitions directly in the Python code, or in separate files.

Before creating the script, the basics of the Python language was important to under-

stand. For the objectives in this thesis, the most important was to know how the language is built up, and how vectors (arrays) are manipulated. Since Abaqus/CAE is based on Python, the input and output files can be manipulated by the use of Python coding (SIMULIA, 2012). It should also be noted that all Python code mentioned in this thesis are compatible with Abaqus/CAE version 6.14 primarily.

4.1.1 Geometry: Scripting procedure

Initially, the geometry of the model was created manually in the Abaqus/CAE GUI. Whenever something is edited in the GUI, these changes are saved in the journal file (.jnl). The understanding of the changes that appeared in the journal file helped getting started on the Python coding of the model, since it was possible to see how Abaqus/CAE interpreted changes made in the GUI.

It is possible to save the journal file as a Python file, to ise as input file in Abaqus/CAE. The idea was thus to create a general input file for the geometry and material properties with use of the journal file. A flowchart of how the initial scripting procedure was done is shown in Figure 4.1.
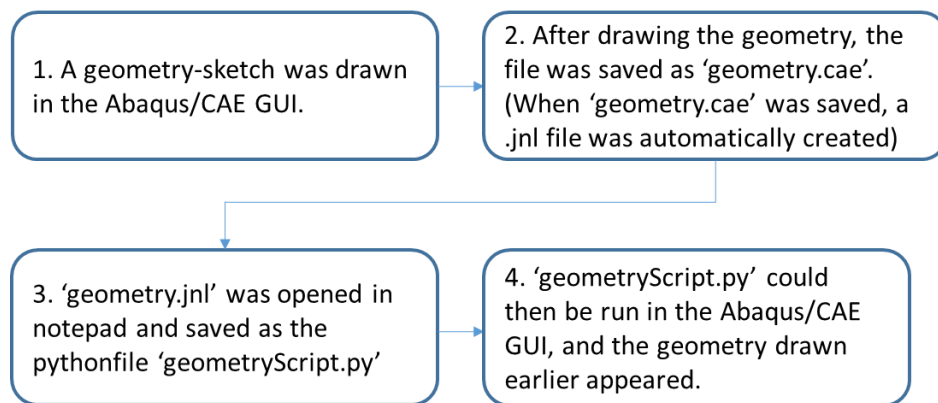
Figure 4.1: Initial procedure for creating the Python script.

A textfile with the coordinates of the contact wire, messenger wire, and the support was created. This file is shown in Appendix C.1. The input coordinates that were used for the contact and messenger wire are showed in Figure 4.2, which numbering coincide with the values given in Appendix C.1.

Note that in Figure 4.2 b), the messenger and contact wire coincide from a viewers perspective. On behalf of the contact wire and messenger wire coordinates, the majority of the model
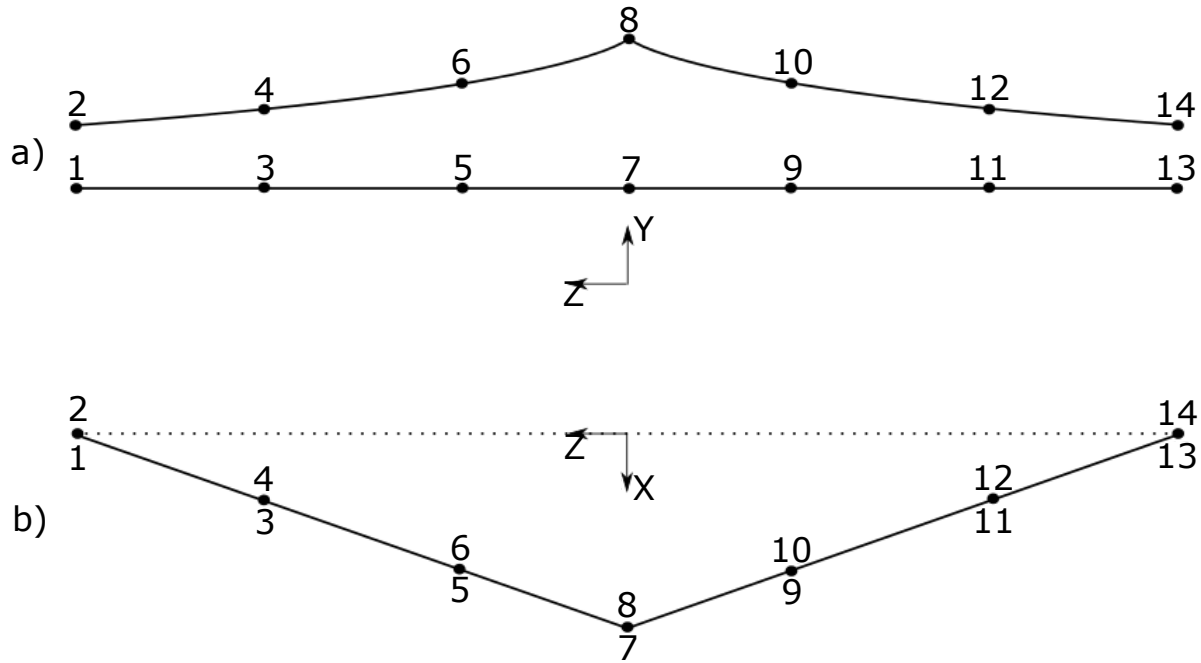
Figure 4.2: Coordinate points for contact and messenger wire: a) Sideview of the model, b) top-view of the model.

could be created in the script, since many of the other components in the model (droppers, cantilevers, external wires), was directly dependent on the coordinates given in Figure 4.2.

In Figure 4.2, the points 3-6 and 9-12 resemble the points where the droppers are connected to the contact and messenger wire. The dropper coordinates were thus added directly from the contact and messenger wire coordinates. In addition, the droppers were given a sinusoidal deflection of 5mm at their respective midpoints, to introduce some form of geometric error. The latter had to be done, since numerical computations with the use of the finite element method will treat a straight line as a perfectly straight line, with no geometrical errors at all.

Due to Ambrósio et al. (2012), it is common to use 4-6 elements along each dropper when modelling with the use of the finite element method. Since the laboratory model is small compared to real OCLs, and only four droppers were included in the model, the sinusoidal generation of the droppers was done with the use of 50 points. This was primarily done to get a smooth and physically correct deformation pattern of the droppers.

The Cantilevers and supporting wires (see Figure 3.2) were added to the script by the use of the endpoint coordinates (point 1,2 and 13,14 in Figure 4.2) of the contact and messenger wire as basis, in combination with offset values to get the components included correctly.

The support was created by the coordinates A-R in Figure 4.3, which correspond to the

coordinates given in Appendix C.1. Note that point C in Figure 4.3 coincide with point 8 in Figure 4.2. The registration arm dropper (point H to J), was given a sinusoidal deflection like the droppers.
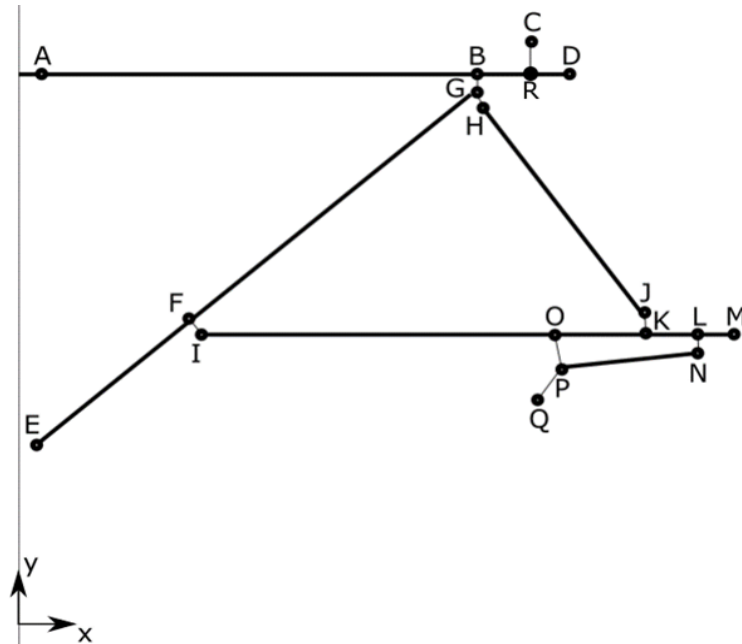
Figure 4.3: Coordinates assigned to the the support in the Python script.

After including all the geometry in the script, an additional feature was added, which related to the possibility of excluding droppers from the model. By changing an input in the Python script, a dropper could be suppressed, and thus not be part of the generation of the model geometry. This was done to easily create models where one or more droppers were excluded. The part of the Python script regarding geometry is added as Appendix D.1, which include all geometric inputs and creation of sets. Figure 4.4 shows a flowchart of how the geometry-version of the script is built up, and how it is meant to be used.
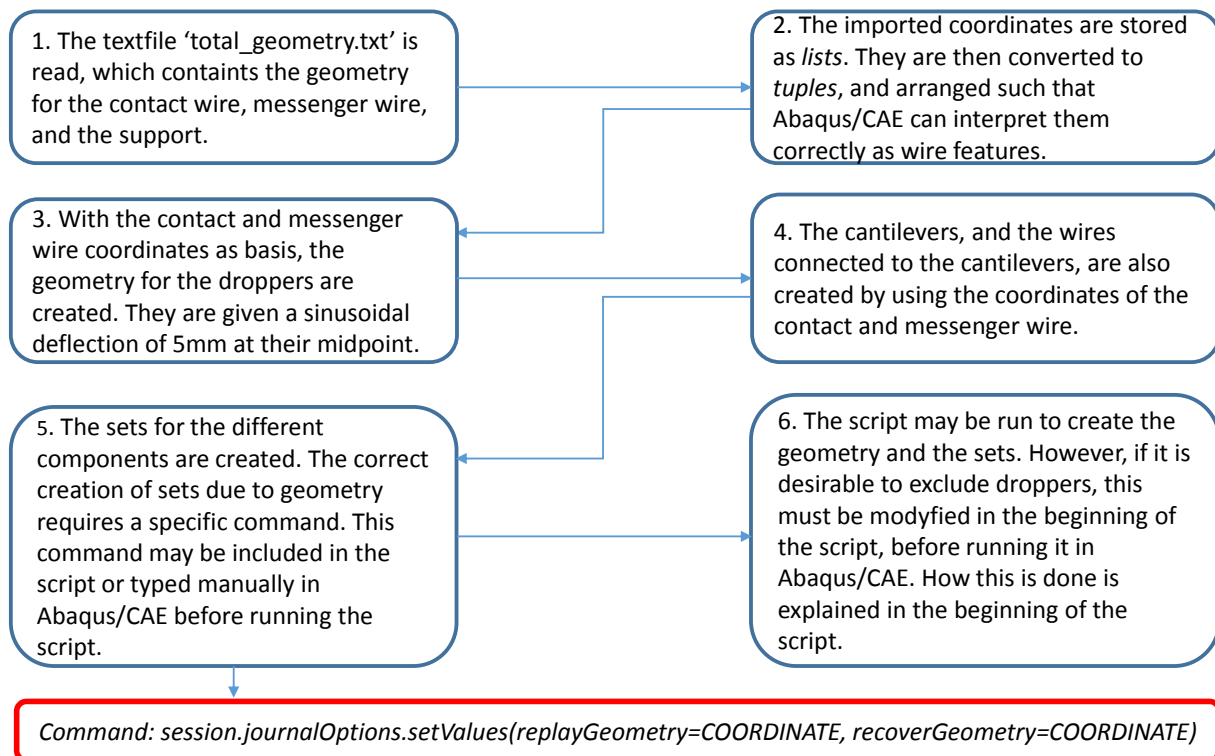
Figure 4.4: Sequence of how the geometry is manipulated in the Python script.

The second box in Figure 4.4 mentions that the coordinates must be stored as tuples. This is done both to make all coordinates consistent, and to make sure Abaqus/CAE is able to process the data correctly.

The following theory regarding Python can be read about in the manual Van Rossum (2015). In Python, there are several ways to treat vectors/matrices, commonly more known as arrays. One type is lists, which is a 1D version of an array. When using lists, it is possible to store both strings, floats and integers in any way desirable. In addition to lists, there are tuples. Tuples can be built up the same way as lists, but are *immutable*, which means that after creating them they are not modifyable. Thus, all the coordinates were converted to tuples, to make sure Abaqus/CAE interpreted the coordinates correctly.

Note the command given in the red box in Figure 4.4. This command will enable the creation of sets by the use of coordinates, instead of the default way of creating sets. The default way of creation of sets in Abaqus/CAE is done by the use of geometric faces (SIMULIA, 2012).

A couple of other things are important to be aware of before running the Python script attached in Appendix D.1. First of all, the code should by stored as a .py file, to create a Python file. Secondly, the user must confirm the correct spacing in the code, since Python is an indentation type of programming language. Especially when statements like *for, if* and

while are used, the indentation is important to use correctly. Last but not least, always make sure that the total_geometry.txt-file is in the same folder as the script is meant to be run from.

4.1.2   Materials and profiles: Scripting procedure

After the geometry and sets were made, the script was developed further to include materials and profiles. The material specifications that were included in the model was read from a textfile called materialprop.txt, which is shown in Appendix C.2. This file contains the name of each material, Young's modulus, density and Poisson's ratio. The shear modulus was generated in the script, by the use of the Young's modulus and Poisson's ratio.

Further, the profiles were created. Since the different components have big variation in profile type (pipe, circular, rectangle, see Table 3.2), it was not made any textfile that contained the different profiles. The profile data was therefore manually typed into the script, which can be seen in Appendix D.2, under '## PRFOLES INPUT'.

As a result of the manual typing of the profiles, the creation of sections became a bit more tedious than planned. It was therefore made an additional textfile to assign the correct materials to their respective profiles. This file was called section_MaterialAndName.txt, and is shown in Appendix C.3.

After sections were assigned to the different materials, beam section orientation was created. All components were assigned a local orientation such that their respective cross sections was rotated the correct way. The latter may not be important for circular cross sections, since they have the same properties in all directions. However, for cross sections like the contact wire (shown in appendix B.2), which has different properties in different directions, it is necessary to include the correct beam orientation.

Figure 4.5 shows a flowchart that sums up the how the materials and profiles were included in the Python script.

1. The material properties are read from the textfile 'materialprop.txt', which contains all material properties needed in the model.	2. Profile dimensions and types are written manually in the script.
3. Assigning the correct profiles to its respective materials is done with the help of another textfile: 'section_MaterialAndName.txt'	4. Beam section orientation are assigned to all materials, to get the correct cross sectional directions of each component.

Figure 4.5: Sequence of how the materials and profiles was included in the Python script.

After generating both the geometry input and the material input in the python script, the script was manually finished the same way as it was started; by creating model choices in the GUI, saving the model to obtain the updated journal file, and storing the choices in the Python script.

The complete script was meant to be a basis for the model, which could be altered as wanted. Being able to change geometry, steps and loads, and whether to include droppers was now possible to do efficiently by the use of the script. The complete main script, with a *READ-ME* file of how to run it correctly, has been attached as an external file, as supplement to the thesis.

4.2   Modelling choices in Abaqus/CAE

After generating the geometry and material properties from the Python script, the modelling was primarily done manually in the GUI. The changes made in the GUI were continuously saved to the Python script, to keep the script as up to date with the model as possible.

This chapter will mainly focus on modelling choices made to make the model as close to the physical system as possible. The following assumptions were made before continuing the modelling:

- In all analysis related to natural frequency or free vibration, the contact between the steady arm and the registration arm has not been taken into account. Hence, the possible contact between the steady arm and the drop bracket (see Figure 3.12) was excluded. Contact is a nonlinear phenomenon (see Cook et al. (2002)). Since the eigenvalue problem is defined as a linear analysis, the contact between the steady arm and the drop bracket will not be interpreted correctly in the natural frequency analysis (SIMULIA (2014)). If the contact definition was included, the eigenvalue problem would still be calculated in the state the model was prior to the solving of the eigenvalue problem. The latter means that if the two components were in contact before running the frequency analysis, they would stay in contact throughout the analysis, which was considered more wrong than to exclude the contact formulation entirely.

- The steel chains that are connected to the jacks on the right end of the contact and messenger wire was not included in the model.

- Since the slack geometry of the system was used as input in the model (see Chapter 3.1), the gravitational acceleration was altered to 1% of the conventional standard value[1]. The reason for including 1 % of the gravitational field was to avoid unphysical geometry (straight lines), by introducing some form of sag in the contact and messenger wire.

- All material definitions in the model has been assumed to be linear and elastic, with no fracture or yielding limit included. The reason for this is that the system will not be applied external loads that may cause yielding nor fracture.

---

[1]Conventional standard value assumed to be equal to: g=9.81m/s^2

4.2.1 Geometric assumptions

Some simplifications were made due to the geometry of the different components in the model. The cantilevers, the contact and messenger wire, and the droppers were modelled slightly modified due to their respective cross sectional data.

Cantilevers and contact wire

The cantilevers and the contact wire was modelled as beam elements, where generalized beam profiles were used. The cross sectional data used were the same as shown in Appendix B.1 and B.2. This simplification was done to avoid the complicated geometry that is related to both these cross sections, and at the same time being able to model the geometry as beam elements instead of solid elements, which would reduce the computational cost significantly.

Messenger wire and droppers

The droppers and messenger wire cross sectional geometry was showed in Figure 3.8. In the numerical model, the nominal area was used both for the droppers and the messenger wire. This assumption was made to avoid the complicated modelling of stranded wires. However, this simplification lead to far greater cross sectional area (as much as $\approx$30% [2] higher cross sectional area for the messenger wire).

4.2.2 Mesh and element formulation

All the components in the numerical model were modelled as beam elements. As mentioned in Ambrósio et al. (2012), it is common to model catenary systems with Euler-Bernoulli beam elements (which is called *B33* in Abaqus/CAE (SIMULIA, 2014). However, the element formulation used was based on Timoshenko beam theory, which is named *B31* in Abaqus/CAE.

Even though it is sufficient to use Euler-Bernoulli beam elements in the analysis of catenary systems (due to the neglection of shear deformation), the analysis run did not converge with these elements. The analysis did however run with Timoshenko beam formulation, which was kept as element formulation in all analysis made.

The mesh was generated with element lengths of approximately 0.2m. However, since the droppers and the registration arm dropper was divided into small segments in the geometry input, the smallest elements in the model were approximately 0.02m. Figure 4.6 shows how the mesh was generated.

---

[2]Messenger wire as example: $A_{\text{effective}}$=65.81mm^2, A_{nominal}=$\pi \cdot \left(\frac{10.5}{2}\right)^2$=86.59mm^2 $\Rightarrow \frac{A_{\text{nominal}}}{A_{\text{effective}}}$=1.32
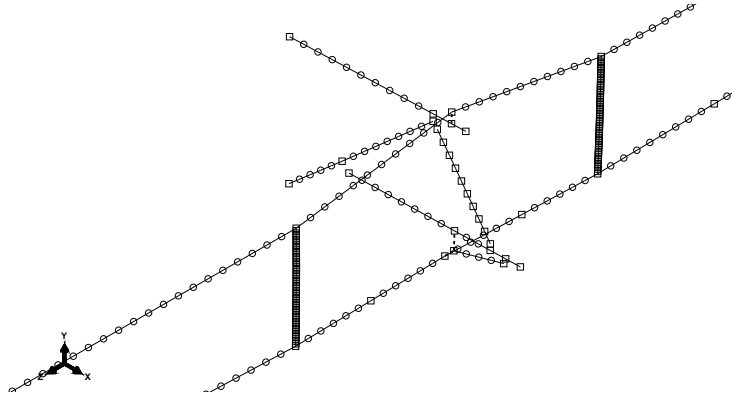
Figure 4.6: The mesh used in the finite element model. Included in the figure: The support, dropper 2 and 3, and the contact and messenger wire.

4.2.3   Boundary conditions

All the boundary conditions prescribed in the model relates to the components that are fastened to the wall. This is shown in Figure 4.7, where the cantilevers, the support and the external wires was set fixed to the wall. In relation to the physical model, the assumption of fixed boundary condition is most accurate for the cantilevers (see Figure 3.21). The boundary condition of the support may have been given free rotations in all directions, in relation to Figure 3.17, but this was ignored as a simplification.
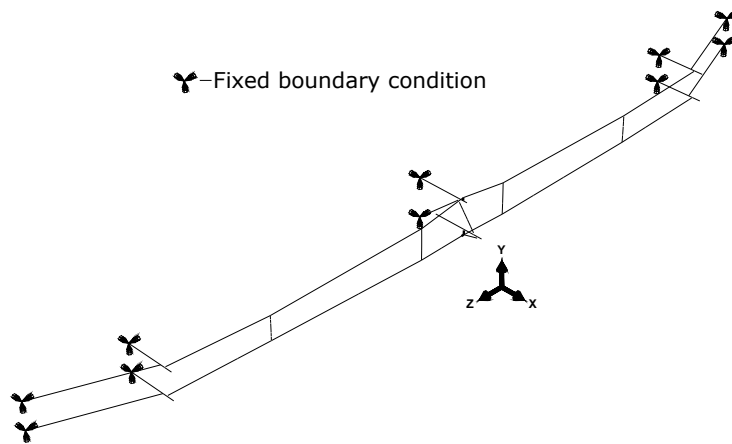
Figure 4.7: Boundary conditions used in the numerical model.

The boundary conditions related to the external wires are more comparable to hinges in the physical system (see Figure 3.20). But, since the element mesh was made rather fine (small elements), and since the external wires only were meant to include axial forces, the assumption of fixed boundary condition would not contribute to much difference from the physical behavior. Free rotations in all directions may have been used as an alternative

boundary condition for the external wires.

4.2.4 Connections between components

The connections between all the components at the support has were by the use of kinematic coupling constraints, which theoretical backgound can be found in Cook et al. (2002), SIMULIA (2014). The connections at the support can be seen in Figure 4.8.
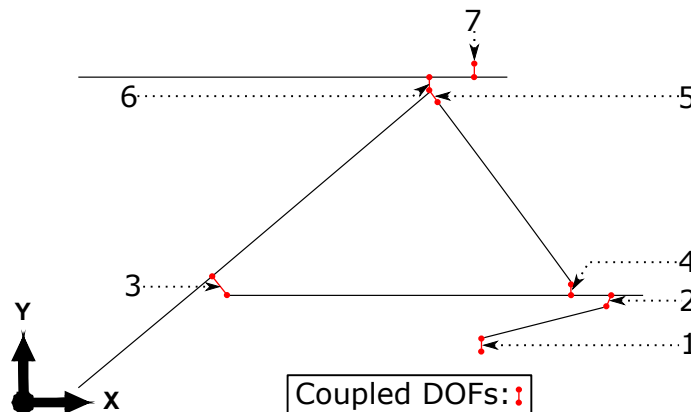
Figure 4.8: Connections of the different components at the support.

The reason for modelling the connections as Figure 4.8 shows, was to avoid the detailed inclusion of the real connections in the model. Hence, all the physical hinges and fastening points between the components were replaced by a gap, and the DOFs at these specific positions were coupled. The constraints at the support were defined as follows, where each number in the list correspond to the same position as shown in Figure 4.8:

1. The steady arm was set fixed to the contact wire, making all translational and rotational DOFs in this coupling constrained (see Figure 3.11 for comparison with laboratory model).

2. The steady arm was connected to the registration arm with all translational DOFs constrained, making the connection free to rotate in all directions (see Figure 3.12).

3. The registration arm was connected to the cantilevered tube with all DOFs constrained, except free rotation about the global z-axis. As seen in Figure 3.14, this is not entirely true. The registration arm is also allowed to rotate about the global y-axis. This was not taken in to account, to get the analysis to converge.

4. The Registration arm dropper was connected to the registration arm with fixed translations, and with free rotations in all directions (see Figure 3.13).

5. The registration arm droppers connection to the the cantilever tube was supposed to be the same as its connection with the registration arm, but it was necessary to add a rotational constraint about the global x-axis to get the model to run properly. This may be because the point assigned to the cantilever tube in this connection was also used to connect the cantilever tube to the top anchor. Kinematic constraints should, optimally, not be specified differently in the same point (SIMULIA, 2014). This was circumvented by the choice of two different control points for the constraints. It may however have been better to use two different nodes when distinguishing between these two connections.

6. The top anchor and the cantilever tube were connected in the same way as the cantilever tube and the registration arm (point number 3 in Figure 4.8), where all DOFs were constrained except rotation about the global z-axis (see Figure 3.15).

7. The messenger wire was connected to the top anchor by constraining all DOFs except translations in the global z-direction, and rotation about the global x-axis (see Figure 3.17).

The contact wire, the messenger wire and the external wires were set fixed to the cantilevers, based on the same assumption as explained in Chapter 4.2.3, related to the boundary conditions of the external wires. The droppers were set fixed to the contact and messenger wire. However, as a result of of the initial sinusoidal deflection created in the droppers, and due to the number of elements used, the actual behavior of the dropper connection should more or less resemble a hinged connection, even though they were modelled with fixed connections.

4.2.5   Steps and load history

The modelling of wires/cables require a special application of loads, to avoid singularities in the stiffness-matrix calculation (as mentioned in Chapter 2.2). Since both the contact wire and the messenger wire can be compared with highly flexible cables, where the bending stiffness is much smaller compared to the geometric stiffness, the load history in the modelling procedure are of great importance. The sequence of steps used may be summed up as:

Step 1.   The first step included a pre-tension load, to activate the geometric stiffness of the contact and messenger wire. This was done simply by applying a load in the axial direction in both ends of the contact and messenger wire, equal to 0.1% of the wanted level of tension in the wires. The reasons for not applying all of the wanted tension in the wires in the first step were 1) to avoid numerical error that may be introduced due to a sudden application of load, and 2) since the gravitational field was supposed to be applied in a subsequent step, the tension in the wires would have been altered to an erroneous value. Hence, the pre-tension was only applied to activate the geometric stiffness of the wires, to avoid a singular tangent stiffness-matrix (Mathisen, 2014).

Step 2.   After applying the pre-tension load, the gravitational field was applied. Initially, the gravitational acceleration was set to g=9.81 m/s^2. Since the input geometry was taken for the system in a slack state (see Chapter 3.1), the gravitational acceleration was altered to 0.01g.

Step 3.   In the third step, the wanted amount of tension in the contact and messenger wire was applied. Originally, this was done the same way as for the pre-tension made in step 1, by applying point loads in each end of the contact and messenger wire. However, this method of applying tension did not resemble the behavior of the system as wanted. Instead, a temperature-field was assigned to the contact and messenger wire, to create tension. The application of the temperature field will be further explained in Chapter 4.2.6.

⇒   All the first three steps were created as static, general steps in Abaqus/CAE. The settings were set to the default values, except the inclusion of nonlinear geometry. This was included by letting *NLgeom* be switched on, in each step. The first three steps were included in all analysis done in the finite element model. Depending on which analysis that was done, other steps was added after step 3:

Frequency step.   To calculate the natural frequencies of the model, a linear perturbation, frequency step was created. In this step, a prescribed value of eigenvalues

were chosen, and the rest of the settings were set to the default values.

Dynamic step   To simulate the excitation of the first two mode shapes performed in the laboratory (see Chapter 3.5.1), a modal dynamic step was created. In order to create this step, it was necessary that the eigenvalue-problem was solved prior to the creation of this step. The modelling method related to the reconstruction of the free decay measurements performed in the laboratory will be further explained in Chapter 4.3.

Elasticity step   To calculate the elasticity along the system, a general, static step was created. This was done after step 3, and was independent of the frequency and modal dynamic steps.

Since the analysis of this type of model is of nonlinear art, the step sequence is not possible to take at random. Neither is it possible to superimpose solutions gained in different steps. Note that the first three steps are the main sequence of steps. All succeeding steps can be varied and selected for the specific analysis wanted. This was the reason for including the first three steps in the main version of the python script. In this way, the python script could be run as a basis before editing the model to fit the specific analysis wanted. For instance, the script was run twice to create to models; one that was assigned to the frequency-analysis, and one that was assigned to find the elasticity along the span.

4.2.6   Applying tension

As mentioned in Chapter 4.2.5, the tension in the contact and messenger wire was first applied by introducing forces at the endpoints of the wires. This choice was however rejected, and a temperature-field was instead used to create tension. The temperature field was assigned to the contact and messenger wire as a predefined field, with a negative magnitude to create tension in the wires. Figure 4.9 shows the difference in model behavior due to choice of tension-application. The dotted lines in Figure 4.9 shows which state the system was in, *before* tension was applied.

The actual behavior of the system will look more like Figure 4.9 a). Since the jacks are installed to create tension by pulling on the wires, the deformation will make the cantilevers move slightly *inwards*. On the contrary, by applying point loads in the endpoints, the cantilevers will be pulled slightly *outwards*. The latter is seen in Figure 4.9 b), marked by the blue
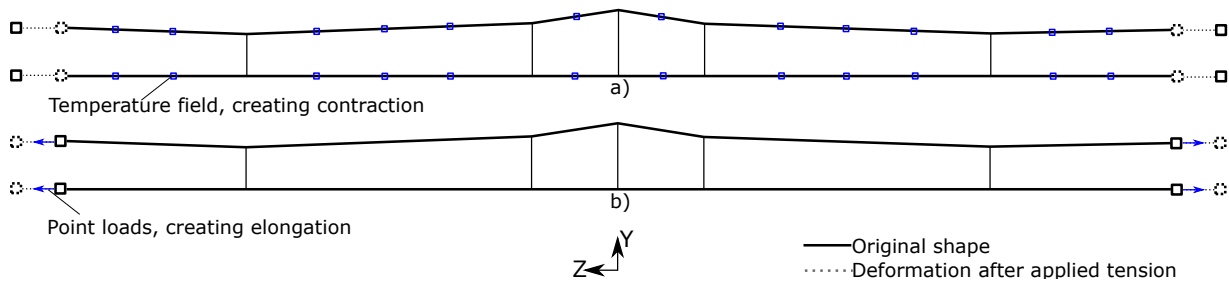
Figure 4.9: Influence of force-application: a) Temperature-field assigned to CW and MW, b) applied force in endpoints of the wires.

arrows. The application of a predefined temperature-field was thus considered as a better method of applying tension in the contact and messenger wire, since it better resembles the physical behavior of the system.

As it was of interest to find many combinations of tension in the contact and messenger wire, the use of temperature-field as force-application demanded some further optimization. Each choice of temperature-gradient in the wires led to one specific tension-combination.

Initially, the idea was to handcalculate how much temperature that had to be applied to obtain a specific tension in both wires. The basic theory for this calculation is given in Chapter 2.9. Since the system showed a nonlinear trend in tension-development for different temperature changes, the theory explained was not applicable directly. Instead, an optimization of varying tension as a result of different temperature changes was done by the use of an iteration-scheme. This was done by either setting the contact or the messenger wire to hold a specific value of tension, and altering the tension in the other wire. Chapter 4.2.7 explains how the temperature-gradients for many different tension-combinations were acquired by introducing an iteration scheme.

4.2.7 Iteration scheme to find tension-combinations in CW and MW

The objective with the iteration-scheme was to find general expressions for how the temperature gradients in the contact and messenger wire had to be varied to achieve the wanted development of tension in the wires, in the numerical model. The scheme will be explained with the contact wire set to 10kN (all droppers included in the model), and by varying the tension in the messenger wire as example:

- Initially, six different tension-combinations were chosen, where the values of tension

in the messenger wire was set to [5,7,9,11,13,15]kN[3], and the contact wire tension was kept at 10kN. The accompanying temperature-gradients for each tension-combination were found by manual iteration, until the correct tensions and corresponding temperature changes were acquired in Abaqus/CAE.

- After finding the corresponding temperature changes for the six mentioned tension - combinations, the corresponding values were fitted to second order polynomials to get a general development. The fitting of CW=10kN with varying tension in the messenger wire is showed in Figure 4.10.

- After fitting the temperature changes as shown in Figure 4.10, it was possible to extract a tension in the messenger wire in the interval 5-15kN, and combine it with the prescribed 10kN tension in the contact wire, and thus use these values as input to the finite element model.
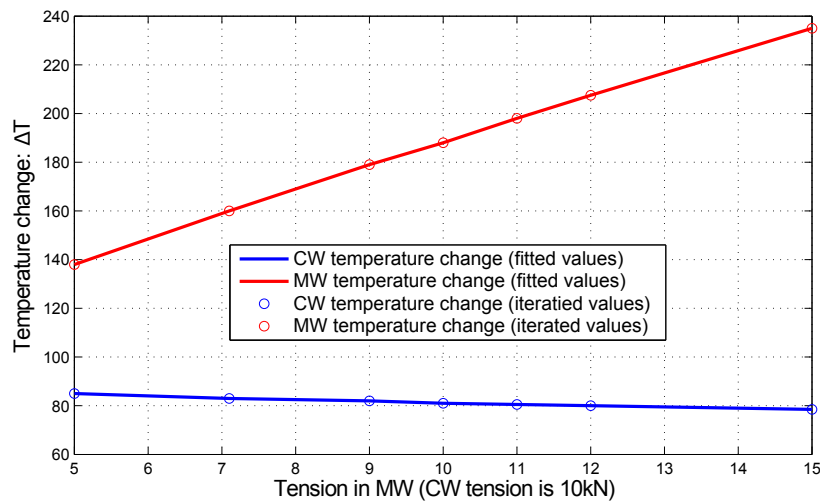
Figure 4.10: Temperature change plotted against tension in messenger wire. Contact wire tension is set to 10kN, all droppers included.

---

[3]The interval was chosen between 5-15kN, as a result of the wanted tension-combinations explained in Chapter 3.5.1

The difference between the background theory and the iteration scheme is best shown by an example: Consider the tension-combination CW-10kN - MW-10kN (all droppers included). The simplified hand calculation (Equation 2.36) of the temperature change resulted in the following values[4] of tension in the contact and messenger wire:

$$\Delta T_{CW} = \frac{N_{CW}}{EA\alpha_{CW}} = \underline{40.85K} \quad \text{and} \quad \Delta T_{MW} = \frac{N_{MW}}{EA\alpha_{MW}} = \underline{56.61K}$$

In comparison, by looking at Figure 4.10, the actual temperature change needed to achieve 10kN tension in both wires are $\Delta T_{CW} \approx 80K$ and $\Delta T_{MW} \approx 190K$. This shows that the iteration scheme is necessary, since the temperature change can not be achieved by simple hand calculatons in this model. This also emphasizes that the model must be considered as a system, not as separate wires, and that it includes nonlinear effects due to the application of tension with the use of a predefined temperature-field.

---

[4]In this calculation, the Young's modulus and cross sectional area are taken from Table 3.1. For the messenger wire, the nominal area is used. The thermal expansion coefficient is set to α=17·10^{-6} for both wires.

4.3   Free decay - Modelling method

In this chapter, the modelling method performed to reconstruct the free decay tests done in the laboratory (see Chapter 3.5.1) is explained. In particular, two things were of interest to achieve by doing the reconstruction:

- Produce a similar time-acceleration plot as the laboratory tests gave.

- Verify that the assumption made about the first two vertical natural frequencies obtained in the laboratory measurements: They were related to the highest peak in the FFT obtained from the time-acceleration plot.

If the second bullet-point above proved right, it would be possible to compare the first two vertical natural frequencies in the finite element model with the results obtained in the laboratory tests.

As mentioned in Chapter 3.5.1, the free decay tests were performed by exciting the contact wire into harmonic motion, until the system went into its expected vertical free vibrating mode. In Abaqus/CAE, a simplification of this method was performed. Instead of exciting the contact wire into harmonic motion, it was applied a vertical force in:

1. the same point as the *excitepoint* shown Figure 3.27, to reproduce the first vertical mode shape.

2. two points: Between dropper 1 and 2, and between dropper 3 and 4 on the contact wire (see Figure 3.26). This was done to reproduce the second vertical mode shape, and the two forces were applied in opposite directions. This is further visualized in Figure 4.11.
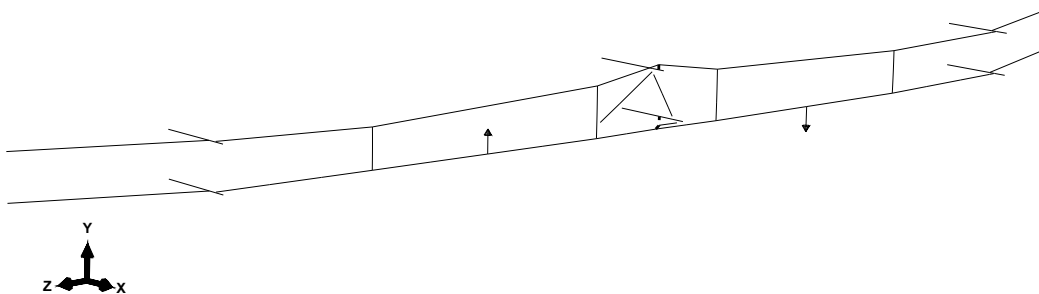
Figure 4.11: Forces applied in the numerical model to reproduce the second vertical mode shape.

After applying the force(s), which led to an excitation of the model, it was removed rapidly, forcing the system into free vibration.

The acceleration could thus be measured in the same way as in the laboratory tests. The measurement of acceleration was done in the same point as in the laboratory tests (see Figure 3.26), and the time period of interest was set to the same; 240s. The difference between the laboratory tests and the finite element modelling can be summed up as:

- Vertical force-and-release instead of harmonic excitation, to set the system into motion.

- Sampling frequency was set to 1000Hz in Abaqus/CAE (in contrast to 2048Hz in the laboratory).

- The acceleration was only measured in vertical direction in the finite element model, in contrast to the measurements done with the accelerometer. The accelerometer in the laboratory could only measure magnitude of acceleration, which may be related to all three dimensions. As the accelerometer was mounted with a slight skewness, relative to the vertical plane, the amplitude of acceleration was thus less comparable.

Finally, the procedure used to verify that the vertical natural frequencies obtained by solving the eigenvalue-problem in Abaqus/CAE, could be compared with the results obtained in the laboratory measurements, may be summed up as:

1. Started with obtaining a rough estimate for the Rayleigh coefficients from the laboratory results, to use as input in the finite element model. This was primarily of aesthetic reasons, since a good approximation of damping proved hard to achieve.

2. After running the modal dynamic simulation, the time and acceleration was obtained in the same point as the accelerometer was mounted (see Figure 3.26).

3. The time-acceleration plot was then analyzed in the same way as was done for the laboratory results, by the use of the FFT.

4. In the resulting spectra gained from the FFT, the frequency that had the highest peak in the spectra was of interest. The idea was to check whether the frequency with the highest peak was similar to the frequency of the wanted mode shape, which was obtained by solving the eigenvalue-problem in Abaqus/CAE.

This method will be used to perform the reconstruction of the free decay measurements performed in the laboratory. It will primarily be used to validate that the first two vertical

natural frequencies obtained by solving the eigenvalue-problem in Abaqus/CAE, relates to the highest peak in the time-acceleration plot gained from the modal dynamic analysis.

Chapter 5

Laboratory results and discussions

5.1 Natural frequencies

By the use of the methods explained in Chapter 3.5.1, the natural frequencies for the first two vertical mode shapes were registered for the 100 measurements done in the laboratory. The results are given in Table 5.1 and 5.2, where the average frequency and the respective standard deviation of the five measurements done for each combination of tension is showed.

Table 5.1: Average value of first natural frequency obtained in laboratory.

Tension-combination	All droppers included		Dropper 2 removed	
	f_1 [Hz]	σ [Hz]	$f_{1,\text{dr2rem}}$ [Hz]	σ_{dr2rem} [Hz]
CW-7.1kN - MW-7.1kN	3.0683	0.0023	2.7208	0.0000
CW-7.1kN - MW-10kN	3.3058	0.0023	2.8500	0.0000
CW-10kN - MW-7.1kN	3.2583	0.0000	2.9433	0.0023
CW-10kN - MW-10kN	3.4958	0.0000	3.0958	0.0000
CW-15kN - MW-15kN	4.0292	0.0000	3.5983	0.0023

Table 5.2: Average value of second natural frequency obtained in laboratory.

Tension-combination	All droppers included		Dropper 2 removed	
	f_2 [Hz]	σ [Hz]	$f_{2,\text{dr2rem}}$ [Hz]	σ_{dr2rem} [Hz]
CW-7.1kN - MW-7.1kN	3.3700	0.0019	3.3108	0.0023
CW-7.1kN - MW-10kN	3.5750	0.0000	3.4908	0.0019
CW-10kN - MW-7.1kN	3.6425	0.0019	3.6158	0.0019
CW-10kN - MW-10kN	3.8550	0.1626	3.7958	0.0000
CW-15kN - MW-15kN	4.4942	0.0023	4.4442	0.0023

All the frequencies given in Table 5.1 and 5.2 are obtained as an average value related to peaks obtained in the FFT. The inclusion of four decimals in Table 5.1 and 5.2 is done to be able to show the standard deviation of the measurements. The standard deviation presented are low relative to the accompanying natural frequency. The latter indicates that for all the five measurements performed for each tension-combination, the peak value in the FFT related to the same natural frequency.

For the results presented, it is noticed that for an equal increase in tension in both wires, the natural frequency will increase. This is intuitive, since for increased tension, the geometric stiffness of the contact and messenger wire will increase (see Equation 2.4).

The natural frequencies obtained in the laboratory ranged between 2.7-4.5Hz for the different tension-combinations, with or without dropper 2 present in the system. To set these values in perspective, consider the first natural frequency, for the CW-15kN - MW-15kN (all droppers included) as an example. The average value for this tension-combination was equal to roughly 4Hz (see Table 5.1). In comparison, the first natural frequency of System 25 (with 15kN in both wires, and the material definitions for the wires as given in Table 3.1), with a span length of 30m, is equal to:

$$f_1 = \frac{\sqrt{\frac{(H_{CW}+H_{MW})}{(m'_{CW}+m'_{MW})}}}{2L} = \frac{\sqrt{\frac{(15000+15000)\text{N}}{(\frac{10.7}{9.81}+\frac{5.96}{9.81})\text{kg/m}}}}{2\cdot30\text{m}} = \underline{2.22\text{Hz}}$$

This indicates that the laboratory model is stiffer than real catenary systems. However, note that the span length used in the example above was set to 30m. The use of this length may not be correct, since the laboratory models *total* length is approximately 30m. Because of how the laboratory model is designed, it may be more correct to separate it in to two spans, and thus use 15m as span length in the theoretical comparison. By doing so, the first natural frequency of System 25, with a 15m span would be 4.44Hz, which is closer to value obtained in the laboratory model. The latter is however not comparable, since the contact wire is not fastened in the vertical direction at the support (see Figure 3.11 and 3.12). It is thus possible to assume that the laboratory model are likely to resemble something between one and to spans, compared to real centenary systems.

The effect of removing dropper 2, due to natural frequency, is showed in Figure 5.1 and 5.2. The black lines in these figures resemble the difference between the natural frequency obtained with and without dropper 2 included in the system. As Figure 5.2 shows, the second

natural frequency seems to be less affected by the removal of dropper 2, than the first natural frequency. Note that the x-axis in Figure 5.1 and 5.2 is not a common, continuous axis. It is only valid at the specific points where the tension in the contact and messenger wire are assigned to it.
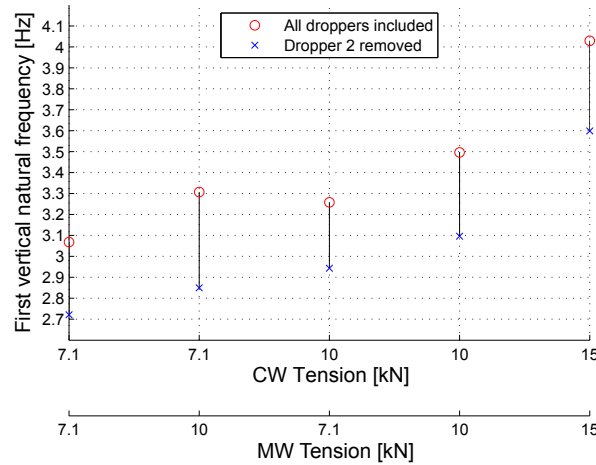
Figure 5.1: First natural frequency for the different tension-combinations, comparison with and without dropper 2 included in the system. X-axis only valid for the tension-combinations included.
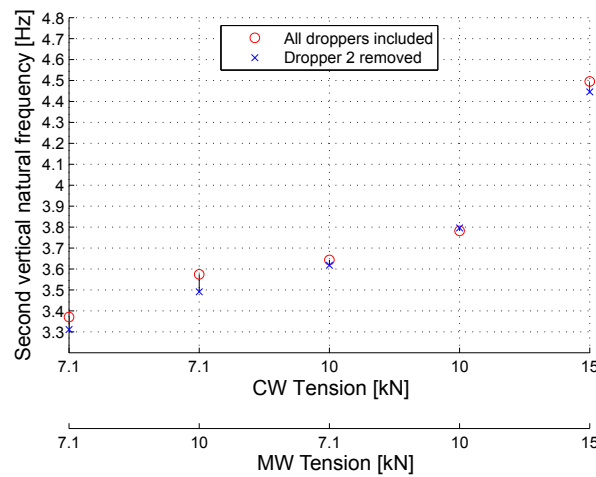
Figure 5.2: Second natural frequency for the different tension-combinations, comparison with and without dropper 2 included in the system. X-axis only valid for the tension-combinations included.

Further, the results showed that both the first and second natural frequency was slightly lower when dropper 2 was removed, compared to when all droppers was included. This makes sense, since the primary reason for including droppers are to support the contact wire vertically, and even out the elasticity-variation along the span. Thus, the presence of

the droppers will increase the stiffness of the model, and removing a dropper should there-
fore decrease the vertical stiffness of the model.

It seems like the first natural frequency is more affected by the removal of dropper 2 than
the second natural frequency. This is observed by comparing Figure 5.1 and 5.2 , and it may
be explained due to the first and the second mode shape. The excitation of the first mode
shape (see Figure 3.27) will lead to biggest displacement close to the support, which motion
makes dropper 2 and 3 the *main droppers* contributing to the vertical stiffness. This is not
the case for the second mode shape (see Figure 3.28), where the biggest displacement is
somewhere between dropper 1 and 2 (or 3 and 4). For the second mode shape, dropper 2
does not need to support the contact wire as much in the vertical direction as it had to do
in the first mode shape. The removal of dropper 2 will thus create bigger sag around the
support in the contact wire, than for instance the removal of dropper 1. The latter is best
explained visually, see Figure 5.3.
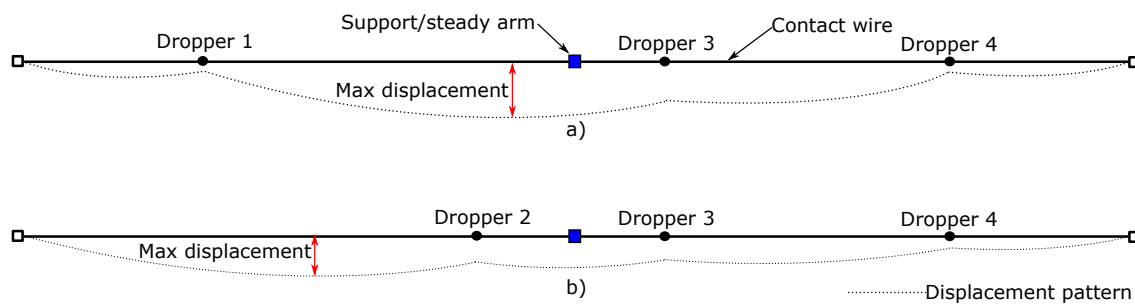
Figure 5.3: System displacement for a) Removal of dropper 2, b) removal of dropper 1.

As Figure 5.3 a) shows, the removal of dropper 2 will make the system be most slack around
the support, which emphasizes that the stiffness contribution to the first mode shape most
likely goes down as a result of this. In Figure 5.3 b) the displacement pattern when remov-
ing dropper 1 is shown, primarily to tell the difference between removing either one of the
two droppers. *It is likely that the removal of dropper 1 will have more effect on the second
vertical natural frequency, than the removal of dropper 2 seemed to have.* The latter state-
ment/hypothesis will be looked further into in a later parameter study, by the use of the
numerical model.

To sum up:

- The laboratory model seems to be more stiff than existing catenary systems, which is
  reasonable due to the model setup.

- In general, the removal of droppers seems to *decrease* the natural frequency, as a result of decreased stiffness in the model.

- The contribution to stiffness in the vertical direction, in relation to a specific mode shape, may be the reason why the removal of dropper 2 primarily affects the first natural frequency, and why the second natural frequency is almost unaffected.

5.2   Damping ratio estimates

With the use of the estimation-procedure for damping explained in Chapter 3.5.1, three different estimates of the damping ratio were calculated for each measurement.

Table 5.3-5.6 shows the average damping ratio for each tension-combination, with and without dropper 2 present in the system. The tables also includes how much the five measurements varies, by showing the standard deviation, in percent of the average damping ratio. The reason for showing the standard deviation as percent of the average damping ratio is due to the values; it may be easier to relate to percentage values, than to the actual standard deviation, for this particular result. Also note that for each tension-combination, three different damping ratios were calculated. This is due to the method of obtaining the damping ratio, as explained in Chapter 3.5.1.

Table 5.3: Damping ratios[1] for first natural frequency, all droppers included.

Tension-combination	ζ $(\cdot 10^{-3})$	$\frac{\sigma}{\zeta} \cdot 100$	ζ_{fh} $(\cdot 10^{-3})$	$\frac{\sigma_{fh}}{\zeta_{fh}} \cdot 100$	$\zeta_{sh}(\cdot 10^{-3})$	$\frac{\sigma_{sh}}{\zeta_{sh}} \cdot 100$
CW-7.1kN - MW-7.1kN	0.34	1.43	0.41	8.67	0.28	14.45
CW-7.1kN - MW-10kN	0.51	8.40	0.54	3.45	0.51	27.28
CW-10kN - MW-7.1kN	0.52	4.24	0.54	2.29	0.51	16.42
CW-10kN - MW-10kN	0.27	10.05	0.29	33.89	0.27	52.95
CW-15kN - MW-15kN	0.25	4.70	0.29	7.15	0.27	6.84

Table 5.4: Damping ratios for first natural frequency, dropper 2 removed.

Tension-combination	ζ $(\cdot 10^{-3})$	$\frac{\sigma}{\zeta} \cdot 100$	ζ_{fh} $(\cdot 10^{-3})$	$\frac{\sigma_{fh}}{\zeta_{fh}} \cdot 100$	$\zeta_{sh}(\cdot 10^{-3})$	$\frac{\sigma_{sh}}{\zeta_{sh}} \cdot 100$
CW-7.1kN - MW-7.1kN	0.48	2.75	0.47	9.55	0.51	21.03
CW-7.1kN - MW-10kN	0.73	34.58	0.59	18.57	0.86	42.82
CW-10kN - MW-7.1kN	0.34	8.95	0.39	9.66	0.28	8.03
CW-10kN - MW-10kN	0.27	5.59	0.29	6.89	0.25	4.58
CW-15kN - MW-15kN	0.43	3.96	0.47	4.32	0.35	13.06

---

[1]ζ_{fh} is the damping ratio for the first half of the acceleration vs time series, while ζ_{sh} is the damping ratio of the second half of the series. The same applies for the notation of the standard deviation. ζ was computed for the entire time series.

Table 5.5: Damping ratios for second natural frequency, all droppers included.

Tension-combination	ζ $(\cdot 10^{-3})$	$\frac{\sigma}{\zeta} \cdot 100$	ζ_{fh} $(\cdot 10^{-3})$	$\frac{\sigma_{fh}}{\zeta_{fh}} \cdot 100$	$\zeta_{sh}(\cdot 10^{-3})$	$\frac{\sigma_{sh}}{\zeta_{sh}} \cdot 100$
CW-7.1kN - MW-7.1kN	0.68	19.29	0.79	23.06	0.47	14.45
CW-7.1kN - MW-10kN	0.67	12.45	0.72	26.56	0.53	27.28
CW-10kN - MW-7.1kN	0.69	11.97	0.86	17.06	0.48	16.42
CW-10kN - MW-10kN	0.52	35.20	0.70	12.49	0.33	52.95
CW-15kN - MW-15kN	0.44	13.52	0.57	18.39	0.31	6.84

Table 5.6: Damping ratios for second natural frequency, dropper 2 removed.

Tension-combination	ζ $(\cdot 10^{-3})$	$\frac{\sigma}{\zeta} \cdot 100$	ζ_{fh} $(\cdot 10^{-3})$	$\frac{\sigma_{fh}}{\zeta_{fh}} \cdot 100$	$\zeta_{sh}(\cdot 10^{-3})$	$\frac{\sigma_{sh}}{\zeta_{sh}} \cdot 100$
CW-7.1kN - MW-7.1kN	0.68	18.34	0.84	17.41	0.32	49.64
CW-7.1kN - MW-10kN	0.58	19.20	0.72	15.52	0.40	27.12
CW-10kN - MW-7.1kN	0.60	12.03	0.99	8.14	0.13	49.85
CW-10kN - MW-10kN	0.55	10.57	0.69	2.40	0.26	34.84
CW-15kN - MW-15kN	0.39	2.08	0.47	3.45	0.33	8.86

Since natural frequency and damping ratio relate to each other (which for instance is shown in Equation 2.15), the values in Table 5.3-5.4 are related to the frequencies mentioned in Table 5.1, while the values presented in Table 5.5-5.6 are related to the frequencies presented in Table 5.2.

The calculation of the damping ratios were primarily done to find a rough estimate of Rayleigh damping, which could be used in the finite element model. The results showed big variation in damping ratio, for all the different tension-combinations. It was therefore hard to explicitly define the damping ratio for the first and the second mode shape. Also in earlier studies on real catenary systems, the damping has been mentioned difficult to estimate (Poetsch et al., 1997).

However, the order of magnitude of the damping ratio calculated may be commented. All the different damping ratio estimates showed in Table 5.3-5.6 had one thing in common: The damping ratio for both the first and the second mode shape were low compared to existing catenary systems. In earlier studies, the damping ratio has been calculated to $\zeta = 1 \cdot 10^{-2}$, which equals 1% of critical damping (Poetsch et al., 1997). This is more damping than what was achieved in the laboratory model, which damping ratios ranged between $\zeta \approx 10^{-4}$ - 10^{-3} (equivalent to 0.01% - 0.1% of critical damping). The practical meaning of this is that the model may be regarded as an undamped system, and that the frequencies obtained most likely are unaffected by damping.

To sum up:

- It is hard to explicitly define the damping ratio for one specific mode shape for the laboratory model, by the use of method explained in this thesis (see Chapter 3.5.1).

- The average magnitude of damping, both for the first and the second mode shape, was found to be in the range $\zeta \approx 10^{-4}$ - 10^{-3}, which is less than common values for existing OCLs.

- Since the damping ratio appeared to be small, it is reasonable to assume that small differences between each performed measurement, will have significant impact on the measurement of damping.

Chapter 6

Validation of the finite element model

The results obtained in the laboratory measurements were used to validate the finite element model. In the validation, the following has been investigated:

1. Validation of correct tension in the contact and messenger wire, and the distribution of forces at the support.

2. Validate that the finite element model could reproduce the free decay tests mentioned in Chapter 3.5.1, and verify that the first two vertical natural frequencies can be compared with the laboratory measurements.

3. Comparison of first and second vertical natural frequencies.

4. Compare the elasticity-development along the span for a certain tension-combination.

6.1 Forces

This chapter will primarily focus on the validation of the tension applied to the contact
and messenger wire in the finite element model, but the forces at the support will also be
commented. The temperatures used to obtain the different tension-combinations are given
in Appendix A.2, which was obtained by the iteration-scheme explained in chapter 4.2.7.

6.1.1 Tension in CW and MW

By iteration in Abaqus/CAE, it was possible to extract the temperature field needed for the
contact and messenger wire to obtain the wanted tension in both wires. Figure 6.1 shows
an example of how the axial forces in the model was distributed for the CW-10kN - MW-
10kN combination, with all droppers included. The temperatures used to obtain the cor-
rect tension for this tension-combination can be extracted from Figure 4.10, which was
ΔT_{CW}=81K and ΔT_{MW}=188K. SF1 is short for section force in 1-direction, which is the ax-
ial direction for all components.
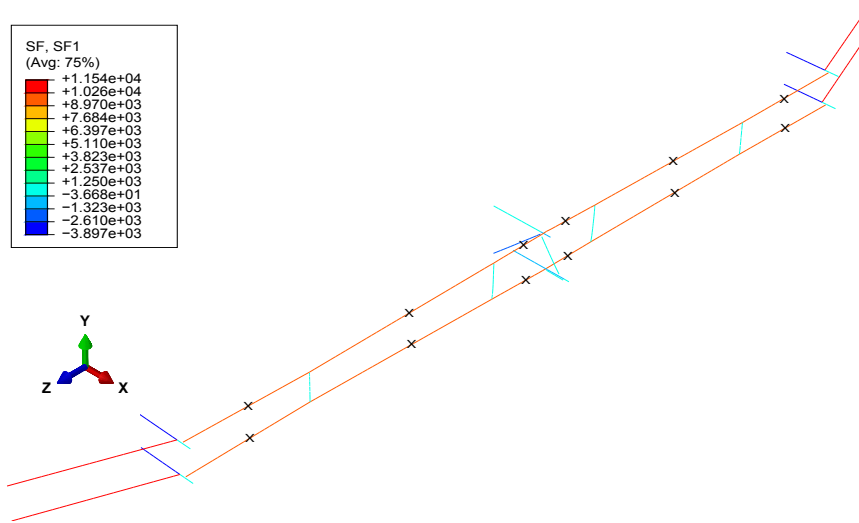
Figure 6.1: Axial force in all components, for the CW-10kN - MW-10kN combination, all
droppers included.

Figure 6.1 is meant to show that the forces in the contact wire and messenger wire was ap-
proximately 10kN. To verify that both wires had an axial force of 10kN, the force was checked
between each dropper, which is marked by black crosses in Figure 6.1. The average of these
forces was then calculated, which resulted in an axial force in the contact wire of 9.975kN,
with a standard deviation of 0.003kN. The average force in the messenger wire was com-

puted to 9.955kN, with a standard deviation of 0.004kN. Both of these values were close to the wanted value of tension.

The same procedure as explained in relation to Figure 6.1 was done to check the other tension-combinations, and a maximum error of tolerance, relative to the wanted value of tension, was set to 1%. The error of tolerance was chosen, primarily to get an as good representation of the tension in the wires as possible, related to the wanted value of thension. The verification of the forces for the five tension-combinations are summed up in Table 6.1, where all droppers was included.

Table 6.1: Verification of tension in CW and MW, all droppers included, results from Abaqus/CAE.

Tension-combination	Wanted tension [kN]		Average tension [kN]	Standard deviation [kN]	Error in %
CW-7.1kN - MW-7.1kN	CW	7.100	7.077	0.002	0.3
	MW	7.100	7.072	0.003	0.4
CW-7.1kN - MW-10kN	CW	7.100	7.079	0.003	0.3
	MW	10.000	9.970	0.004	0.3
CW-10kN - MW-7.1kN	CW	10.000	9.978	0.002	0.2
	MW	7.100	7.101	0.003	0.0
CW-10kN - MW-10kN	CW	10.000	9.975	0.003	0.3
	MW	10.000	9.955	0.004	0.4
CW-15kN - MW-15kN	CW	15.000	14.981	0.004	0.1
	MW	15.000	15.004	0.006	0.0

It should be emphasized that the column called "Error in %" in Table 6.1, is the error of the average force obtained from the six points explained in Figure 6.1, in relation to the wanted force in a given combination[1]. The error has been rounded to one decimal. The reason for including three decimals for the tensions in Table 6.1 is to be able to include the standard deviation, which turned out to be low. This means that the tension along the span for both the contact and messenger wire was consistent.

---

[1] From table: Error in % = $\left| 1 - \frac{\text{Average [kN]}}{\text{Wanted [kN]}} \right| \cdot 100$

The verification of the tension-combinations without dropper 2 included has been done in the same way as explained in Figure 6.1 , and is given in Appendix A.3.

The tensions obtained in the laboratory model is shown in Table 6.2

Table 6.2: Verification of tension in CW and MW, obtained in laboratory.

Tension-combination	Wanted tension [kN]		All droppers included		Dropper 2 removed	
			Obtained tension [kN]	Error in %	Obtained tension [kN]	Error in %
CW-7.1kN - MW-7.1kN	CW	7.10	7.05	0.7	7.05	0.7
	MW	7.10	7.11	0.1	7.07	0.4
CW-7.1kN - MW-10kN	CW	7.10	7.23	1.8	7.21	1.6
	MW	10.00	10.02	0.2	10.10	1.0
CW-10kN - MW-7.1kN	CW	10.00	9.92	0.8	9.94	0.6
	MW	7.10	7.19	1.3	7.26	2.3
CW-10kN - MW-10kN	CW	10.00	9.98	0.2	10.06	0.6
	MW	10.00	10.03	0.3	9.97	0.3
CW-15kN - MW-15kN	CW	15.00	14.45	3.7	14.48	3.5
	MW	15.00	14.50	3.3	14.62	2.5

Note that the accuracy of the sensors measuring the applied tension was restricted to 10N, which is the reason for only including the force with two decimals in Table 6.2. It was more tedious to achieve the wanted values of tension in the laboratory, than it was in the numerical model. However, as Table 6.2 shows, most of the values of tension obtained in the laboratory had an error less than 2% in relation to the wanted values. The tension combination that had highest error was the CW-15kN - CW-15kN, which was approximately 3-4% in error.

Finally, a comparison between the forces obtained in the laboratory and in the numerical model are presented. The deviation between the forces are also included, as percentage of error in the numerical model, in relation to the laboratory model. The comparison is showed in Table 6.3. Note that in the comparison, the values have been rounded to include two decimals. This has been done due to the accuracy of the measurements in the laboratory.

Table 6.3: Tension in CW and MW, comparison between numerical and lobaroory values.

Tension-combination	Wire	All droppers included			Dropper 2 removed		
		Tension numerical [kN]	Tension lab [kN]	Error in %	Tension numerical [kN]	Tension lab [kN]	Error in %
CW-7.1kN-	CW	7.08	7.05	0.4	7.06	7.05	0.1
MW-7.1kN	MW	7.07	7.11	0.6	7.08	7.07	0.1
CW-7.1kN-	CW	7.08	7.23	2.1	7.07	7.21	1.9
MW-10kN	MW	9.97	10.02	0.5	9.98	10.10	1.2
CW-10kN-	CW	9.98	9.92	0.6	9.95	9.94	0.1
MW-7.1kN	MW	7.10	7.19	1.3	7.12	7.26	1.9
CW-10kN-	CW	9.97	9.98	0.1	9.95	10.06	1.1
MW-10kN	MW	9.96	10.03	0.7	9.97	9.97	0.0
CW-15kN-	CW	14.98	14.45	**3.7**	14.96	14.48	**3.3**
MW-15kN	MW	15.00	14.50	**3.4**	15.02	14.62	**2.7**

Discussion

The temperature field applied in Abaqus/CAE seemed to give a good representation of the force-distribution in both the contact and messenger wire. This was verified in Table 6.1, where the deviation of tension was kept under 1% for all the different tension-combinations.

An error in tension of 1% in comparison to the wanted value is not just a random criteria, it is a conservative criteria compared to actual tension deviations in real catenary systems. As mentioned in Chapter 2.1.3, real catenary systems may experience up to 10% of error in tension due to temperature deviations.

The magnitude of tension applied in the laboratory, which are shown in Table 6.2, was more tedious to get close to the wanted magnitude. This was because the adjustment with the jacks was not sensitive enough, to be able to apply the correct values of tension. The values given in Table 6.2 was obtained in the best manner possible, and it was concluded that they were accurate enough due to the purpose of the laboratory tests.

Further, the comparison between the numerical model and the laboratory model was given in Table 6.3. From the table, it is noticed that the percentage of error in the numerical model, in relation to the laboratory model, does not deviate by more than 2% for almost all the tension-combinations. The exception was when 15kN was applied in both the contact and messenger wire. This was not possible to achieve in the laboratory, and it is thus the main reason for the deviation.

- Pay special attention to this particular tension-combination (CW-15kN - MW15kN): It may be used to explain subsequent validations, as a result of lower tension in the

laboratory model compared to the numerical model.

The latter should have been taken in to account in the numerical model, since the tension easily could have been adjusted to be closer to the values in the laboratory.

To sum up:

- The applied tension in the numerical model is close to the wanted level of tension, which emphasizes that the method of applying tension may be applicable.

- To apply the wanted level of tension in the laboratory was not as easily done as in the numerical model, where the maximum deviation from the wanted level of tension was 3-4%.

- The difference in tension between the numerical and laboratory model was, for most of the tension-combinations, less than 2%. The exception was for the CW-15kN - MW-15kN tension-combination, which values of tension were not possible to obtain in the laboratory, as a result of the restriction in the jacks.

6.1.2 Force-distribution at the support

The main focus in this chapter is to validate that the forces in the support are distributed in a reasonable way, in relation to what is expected. Continuing to focus on the CW-10kN - MW-10kN combination as an example; the forces that was obtained at the support, after applying tension in the contact and messenger wire, is showed in Figure 6.2.
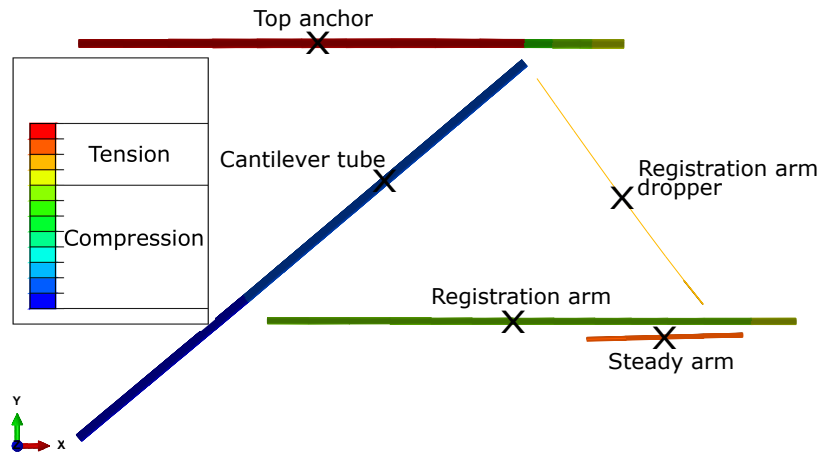
Figure 6.2: Axial force distribution in components at the support, for CW-10kN - MW-10kN combination.

Since the gravitational field was assumed to 1% of the actual gravitational field (see Chapter 4.2), the value of the forces in the components has been removed from Figure 6.2. This is done since the figure primarily are meant to mark which one of the components that are in tension or compression, as a results of the tension applied to the contact and messenger wire.

The values of tension/compression in the different members are summed up in Table 6.4, which was obtained in the positions marked with black crosses in Figure 6.2. As a result of wrong gravitational field, normalized forces are presented. The forces are normalized relative to the force in the cantilever tube, to express which components that were most affected.

Table 6.4: Axial forces at support, CW-10kN - MW-10kN

Component	Force [N]	Normalized force [-]
Top anchor	640.00	1.00
Cantilever tube	-1586.00	-2.48
Registration arm	-391	-0.61
Registration arm dropper	80	0.13
Steady arm	345	0.54

Discussion

Since the model is built with a push-off support in the middle, the registration arm should be in compression. The latter is visualized in Figure 6.2. In Table 6.4, it is emphasized that the most affected components due to the application of tension in the contact and messenger wire, are the top anchor and the cantilevered tube. This makes sense, since they are supposed to be the main load bearing components at the support. It also explains why the top anchor and the cantilever tube are the components with the largest cross sections at the support (see Table 3.2). Note that the cross section of the top anchor are in some OCLs made smaller compared to the top anchor mentioned here, due to the fact that the top anchor is in tension for push-off supports (Kiessling et al., 2009).

The magnitude of force in the components at the support are not comparable to the physical model, which is a result of the reduced gravitational field applied. To be able to compare these forces, the correct gravitational field should have been applied. This is a drawback with the use of the reduced gravitational field: The correct vertical component of forces will not be applied in the model, which may have influence on other results obtained.

To sum up:

• The correct representation of forces at the support seems to have been achieved, since it resembles the same characteristics as a push-off support.

6.2 Free decay

The goal in this chapter was to confirm that the first two vertical natural frequencies obtained in the laboratory measurements, and by solving the eigenvalue problem in Abaqus/CAE, could be compared. By performing the modelling procedure as explained in Chapter 4.3, the first and second vertical mode shape was attempted reconstructed in Abaqus/CAE. Since this type of analysis was rather time consuming, the comparison was only done for the tension-combination: CW-10kN - MW-10kN (first and second vertical mode shape, all droppers included).

The Rayleigh coefficients used, were calculated by the use of the damping ratio obtained for the first mode shape, and by assuming that the second mode had similar damping ratio. This assumption contradicts the results given in Table 5.3-5.6, but since the damping was low, and not particularly well defined, it is a reasonable assumption to make due to aesthetic purposes. The resulting coefficients were assigned to the analysis, both in the attempt to reconstruct the first, and the second vertical mode shape.

The calculation of the Rayleigh coefficients was done with the use of Equation 2.22, and the results are showed in Table 6.5. Still note that α is related to stiffness-proportional damping, and β is related to mass-proportional damping.

Table 6.5: Rayleigh damping

Tension-combination	$\zeta = \zeta_1$ $(\cdot 10^{-3})$	f_1 [Hz]	f_2 [Hz]	α $(\cdot 10^{-3})$ [Hz]	β $(\cdot 10^{-5})$ [s]
CW-10kN - MW-10kN (All droppers included)	0.2657[2]	3.4958	3.8550	6.1222	1.1508

The content in Table 6.5 shows which two values of frequency (f_1 and f_2), and which accompanying value of damping ratio (assumed that the second natural frequency has the same damping ratio as the first), that has been used to calculate α and β. Note that this is not a preferable way to calculate the damping ratio, but since this was the only two natural frequencies (first and second) that was obtained in the laboratory, it was the only values available to use. If a modal hammer analysis had been carried out, the mode shapes and accompanying natural frequencies of higher modes could have been achieved, which may have given better results. Preferably, to get a better representation of damping throughout

---

[2]This value can be found in Table 5.3, and is taken from the result obtained for the whole time series.

the entire range of frequencies, a higher mode of frequency should have been replaced with the second mode (Chopra, 2007).

6.2.1   First vertical mode shape

The results obtained for the tension-combination CW-10kN - MW-10kN is shown in Figure 6.3. The damping data used are taken from Table 6.5. One of the accompanying measurements done in the laboratory is shown in Figure 6.4.
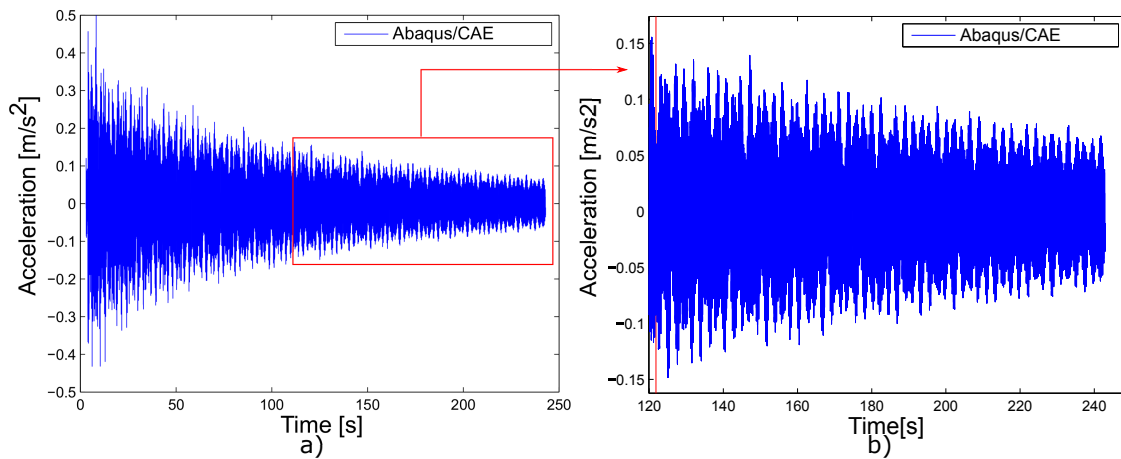
Figure 6.3: Acceleration vs time. CW-10kN - MW-10kN, excited into first expected vertical natural frequency (acceleration in pure vertical direction). a) whole time series, b) zoomed to last half of time series.
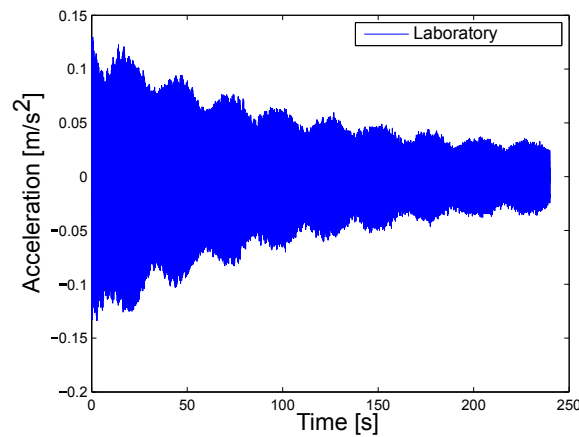
Figure 6.4: Acceleration vs time. CW-10kN - MW-10kN, excited into first expected vertical natural frequency (acceleration as magnitude).

The accompanying FFT spectras related to both Figure 6.3 and 6.4 are shown in Figure 6.5.
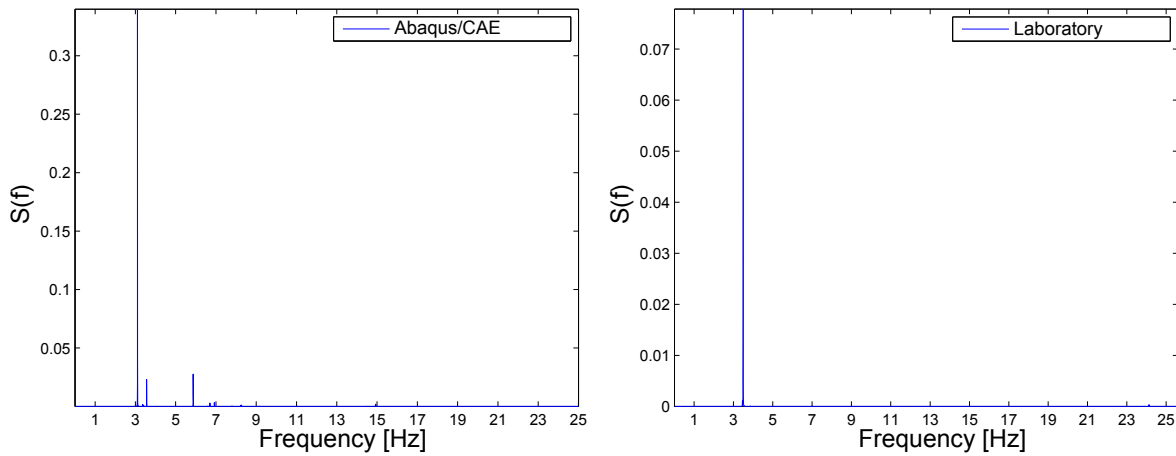
Figure 6.5: FFT spectra for CW-10kN - MW-10kN, first mode shape comparison, all droppers included.

As seen in Figure 6.5 both the spectra obtained in the Abaqus/CAE simulation and the laboratory results seem to have one distinct peak. The frequencies related to this peak are likely related to the same mode shape in both the results, which is expected to be the first vertical mode shape.

The frequency obtained in the FFT spectra, for the highest peak in the Abaqus/CAE free decay simulation, was 3.1Hz. The same value was obtained by solving the eigenvalue problem in Abaqus/CAE, which was done in an earlier step in the finite element model. The accompanying mode shape for this frequency is showed in Figure 6.6.
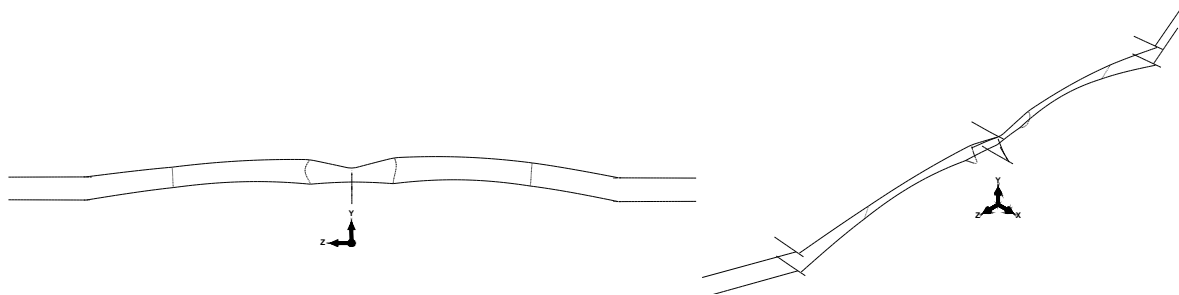
Figure 6.6: First vertical mode shape, shown in 2D (left) and 3D (right), obtained in Abaqus/CAE.

The mode shape shown in Figure 6.6 looks like the assumed first vertical natural mode. This indicates that it is possible to compare the first vertical natural frequency obtained in Abaqus/CAE with the laboratory results obtained for the first vertical natural frequency (for comparison of shapes, see Figure 3.27).

6.2.2   Second vertical mode shape

The same validation that was done in the previous Chapter 6.2.1 was done for the second vertical mode shape. Since the damping of the first vertical mode was assumed equal to the second mode, the same damping data (Table 6.5) were used to reconstruct the the acceleration vs time plot for the second vertical mode shape. The acceleration vs time obtained in the numerical simulation, and in one of the laboratory tests are shown in Figure 6.7 and 6.8, respectively.
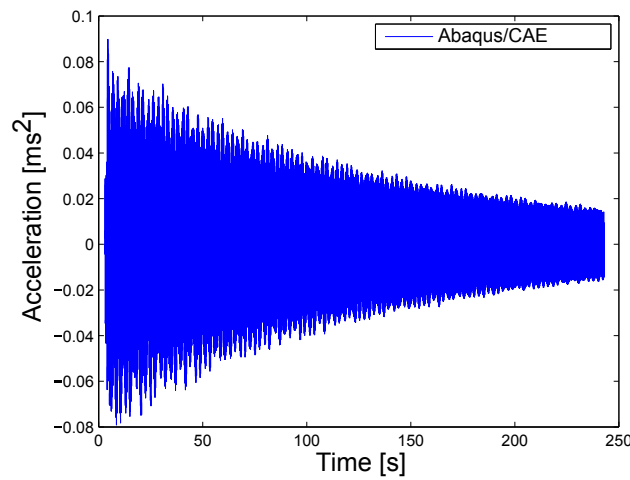
Figure 6.7: Acceleration vs time. CW-10kN - MW-10kN, excited into second expected vertical natural frequency (Abaqus/CAE).
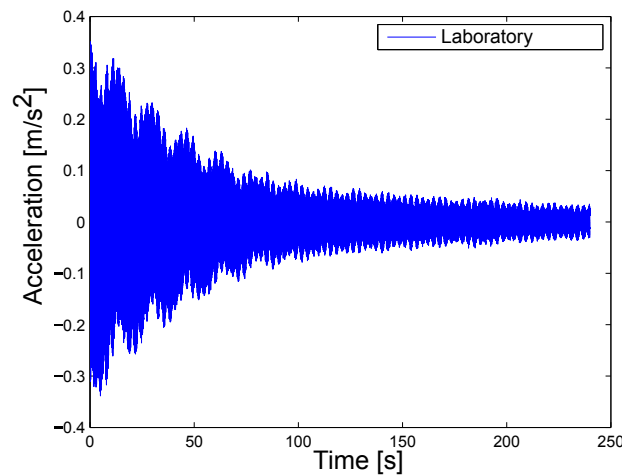
Figure 6.8: Acceleration vs time. CW-10kN - MW-10kN, excited into second expected vertical natural frequency (Abaqus/CAE).

The FFT spectras that relate to the the time-acceleration plots for the second vertical mode shape are shown in Figure 6.9.
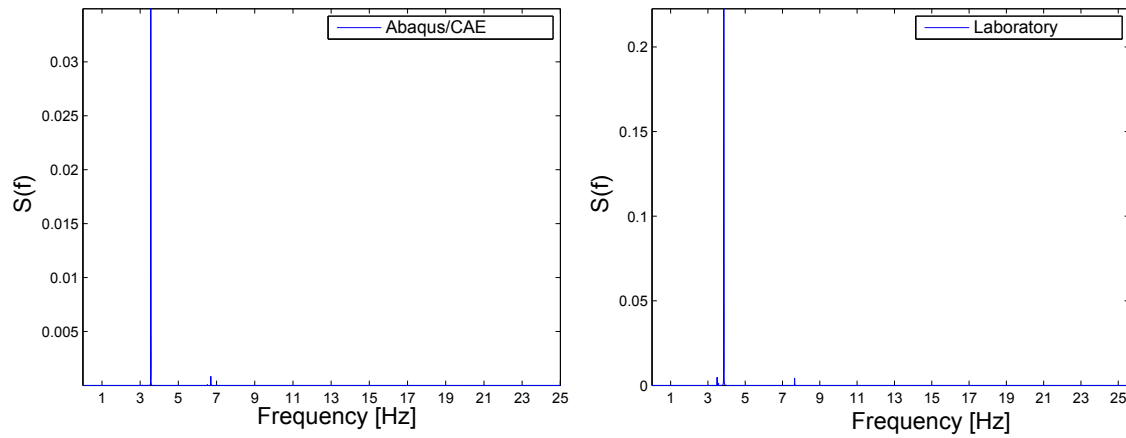
Figure 6.9: FFT spectra for CW-10kN - MW10kN, second mode shape comparison, all droppers included.

Like the first vertical mode shape, both the FFT spectras seem to have one distinct peak, which most likely relates to the same mode shape; the attempted second vertical mode shape shown in Figure 3.28.
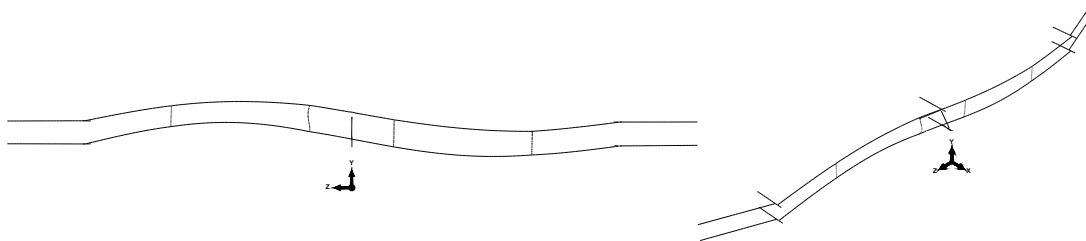
Figure 6.10: Second vertical mode shape, shown in 2D (left) and 3D (right), obtained in Abaqus/CAE.

The frequency of the highest peak in the FFT of the acceleration obtained by the free decay simulation was the same frequency that was obtained by solving the eigenvalue problem, which value was 3.6Hz. The mode shape obtained in Abaqus/CAE for this simulation is shown in Figure 6.10, which seems to resemble the wanted shape shown in Figure 3.28. As for the first vertical frequency, this indicates that the second vertical frequency can be compared with the resulting natural frequencies obtained in the laboratory.

6.2.3   Discussion

The method used reconstruct the free decay measurements has its drawbacks. By the use of the simplified method explained in Chapter 4.3, the amount of energy (i.e the amplitude of the measurements) applied in the simulation will deviate from the laboratory test explained in Chapter 3.5.1. This is because the excitement of the system in the numerical model was applied in a rapid excite-and-release motion, compared to the harmonic motion that was used to excite the laboratory model.

Since the accelerometer used in the laboratory tests measured magnitude of acceleration, and not the acceleration in three dimensions, it makes the amplitudes obtained even less comparable. By comparing Figure 6.3 and 6.4, it is however noticed that the amplitudes for the first natural frequency are in the same order of magnitude. This is especially visualized by the zoomed version shown in Figure 6.3 b), where the amplitude is similar to the amplitude obtained in the laboratory. However, since the prime interest was to extract the acceleration vs time series, and from that find the most occuring frequency in the free vibration, the amplitude was not a parameter that would have impact on the wanted results. The fact that the amplitude was in the same order of magnitude was considered good enough due to the wanted results for this type of analysis.

The damping applied in the analysis was primarily due to aesthetic fashion, but it shows that the order of magnitude is not that far off, in relation to the damping of the the laboratory model. For instance, by comparing the decay of acceleration for the first vertical natural frequency (see Figure 6.3 and Figure 6.4), the decay in acceleration seems to show the same trend. Take a better look at Figure 6.3 b), which resembles the second half of the time span shown in Figure 6.3 a) (time span of 120s). In this plot, the amplitude decays from $\approx$0.15m/s^2 to $\approx$0.7m/s^2. In the accompanying laboratory test (Figure 6.4), the amplitude decays from $\approx$0.13m/s^2 to $\approx$0.06m/s^2 for the first half of the time series (also here, a time span of 120s). This shows that the rate of decay may is plausible, for the first natural frequency.

The development of damping was not as comparable when simulating the second vertical natural frequency (see Figure 6.7 and 6.8). The reason for this may relate to the fact that the excitement done in the laboratory did not show consistency during the time of measurement. Initially, the motion seemed to take the wanted shape (as seen in Figure 3.28), but some time into the measurement, the vibrations started to oscillate in a different pattern. This means that if the damping was to be computed, the damping of the first half of the time

series would most likely relate to the correct mode shape. This also clarifies the reason for obtaining damping estimates for the three different time spans, as mentioned in Chapter 3.5.1.

The fact that the simulation was sampled at 1000Hz in Abaqus/CAE, in contrast to 2048Hz in the laboratory, was primarily due to aesthetic reasons of the plot. The simulation could have been sampled at a lower frequency, since the frequency-range of interest was 1-5Hz for both the first and the second vertical mode (which is because of the values obtained in the laboratory, see Table 5.1 and 5.2). If the highest frequency of interest was set to 5Hz, the Nyquist frequency would be 10Hz (Equation 2.29). Therefore, if the sampling was reduced from 1000Hz to for instance 100Hz, the number of points to calculate in the analysis would be reduced by a factor of 10, and there would still be no need to worry about aliasing. The computational time could thus be drastically reduced.

The objective with the reconstruction of the free decay tests was primarily to validate that the first two natural frequencies could be compared with the laboratory results, by checking if the peak value in the frequency spectra was the same frequency as obtained in the prior frequency-step in Abaqus/CAE. This seemed to be true for both the validations done, since the frequency obtained by taking the FFT of the time-acceleration plots, was equal to the frequency obtained by solving the eigenvalue problem in Abaqus/CAE.

In addition, it should be noted that the second vertical natural frequency did not appear as the second mode when solving the eigenvalue problem in Abaqus/CAE; it appeared as the fourth mode. The second and the third natural frequency obtained in the simulation were related to motion out of the vertical plane, which modes are shown in Appendix A.1.

The fact that the second vertical natural frequency appeared as the fourth mode shape in the eigenvalue problem, indicates that the excitement of the modes proceeding the first mode is easier done out of the vertical plane. The latter may be related to the stiffness of the system in the vertical direction: The stiffness of the system out of the vertical plane is likely to be lower than the vertical stiffness (primarily as a result of the droppers, which contributes to vertical stiffness). Both the second, third and fourth mode obtained in the eigenvalue problem were all related to the same shape; a *full-sine deflection* along the model. Since these three modes relate to the same deflection shape, in different directions, the assumption about lower stiffness out of the vertical plane is plausible for this motion. However, the two modes out of the vertical plane has not been given any consideration, since they could

not be directly compared with the laboratory measurements performed. The occurance of mode shapes out of the vertical plane should however not be ignored, especially in relation to real catenary systems. If for instance wind induced dynamics was of interest, the mode shapes out of the vertical plane may have been important to consider.

To sum up:

- The rough estimate of Rayleigh damping was calculated with an approximate magnitude for the first mode shape, due to an aesthetic fashion.

- By reconstructing the free decay tests performed in the laboratory, it was verified that the first two vertical natural frequencies relates to the highest peak in the resulting FFT spectra, obtained from the time-acceleration plot. This indicates that the first two vertical natural frequencies may be valid to compare with the results obtained in the laboratory measurements.

6.3 Natural frequencies

In Chapter 6.2.2, it was found plausible that the the simulated values of the first and the second vertical natural frequency could be compared with the laboratory results. This validation was however only done by considering the CW-10kN - MW-10kN (all droppers included) combination. It has further been assumed that the comparison was valid for all the other tension-combinations as well. Thus, both the first and the second vertical natural frequency, with and without dropper 2 included, will be compared in this chapter.

The shape shown in Figure 6.6 appeared as the first mode in the finite element model, which was expected to be the first mode shape. The shape shown in Figure 6.10 relates to the second vertical mode shape.

It should be noted that all the values of frequency that are mentioned in this chapter are the average values given in Chapter 5.1 (for the laboratory results), and the accompanying simulated values in Abaqus/CAE, which are given in Table 6.6. Hence, in the subsequent Figures 6.11-6.14, the values plotted are taken from Table 6.6 and Table 5.1-5.2.

Table 6.6: Natural frequencies obtained in Abaqus/CAE, for first and second vertical mode shape.

Tension-combination	All droppers included		Dropper 2 removed	
	f_1 [Hz]	f_2 [Hz]	f_1 [Hz]	f_2 [Hz]
CW-7.1kN - MW-7.1kN	2.65	3.02	2.39	2.99
CW-7.1kN - MW-10kN	3.03	3.26	2.53	3.22
CW-10kN - MW-7.1kN	2.88	3.30	2.62	3.29
CW-10kN - MW-10kN	3.10	3.56	2.79	3.54
CW-15kN - MW-15kN	3.75	4.34	3.38	4.33

6.3.1   First natural frequency

The first natural frequency, for all the five different tension-combinations, are shown in Figure 6.11. In this comparison, all droppers are included in the model.

Note: The Figures 6.11-6.14 only contain information in the specific values that are present on the x-axis. It is thus not possible to extract data between the tension-combinations shown on the x-axis.
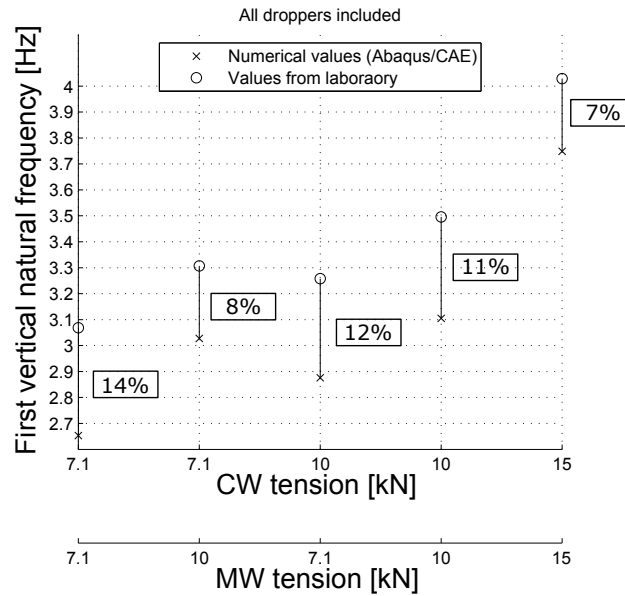
Figure 6.11: Tension in CW and MW plotted against first natural frequency, all droppers included.

In Figure 6.11, the circles represent the natural frequency obtained in the laboratory, and the crosses are the values obtained in the numerical model. The belonging tension-combination are given on the two x-axes; CW and MW tension, respectively. For instance, the natural frequency obtained for the tension-combination CW-7.1kN - MW-10kN is approximately 3.0 Hz for the numerical simulation, and 3.3 Hz for the laboratory test. The black line drawn between the numerical and laboratory values is created to show that the two frequencies are meant to be compared, and that the different tension-combinations should (preferably) represent the same difference in frequency, to ensure consistency in the magnitude of error.

The black boxes which contain a certain percentage next to each frequency-pair shows how much the simulated results differs from the laboratory results[3]. As seen in Figure 6.11, the error is between 7% and 14% for the first natural frequency, with all droppers included in the model.

---

[3]Numerical vs laboratory error $= (1 - \frac{f_{\text{Numerical}}}{f_{\text{Laboratory}}}) \cdot 100$

The first natural frequency when dropper 2 is removed is compared in Figure 6.12.
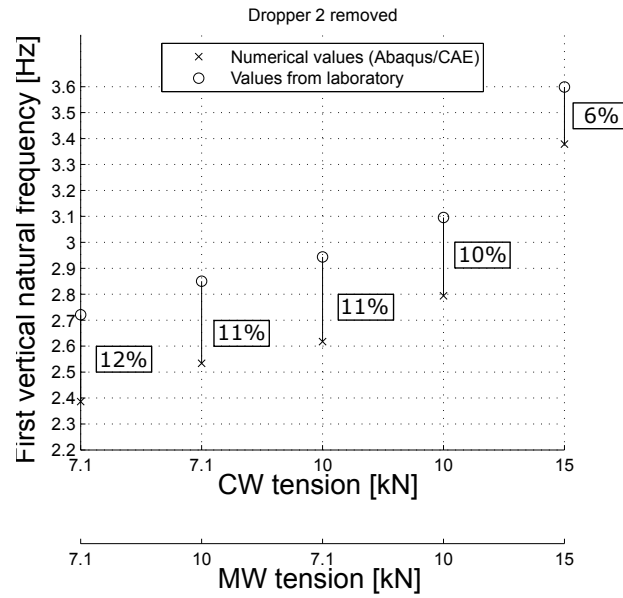
Figure 6.12: Tension in CW and MW plotted against first natural frequency, dropper 2 removed.

Also in Figure 6.12, the development in frequencies seems to follow the same trend for the laboratory results and the finite element model. The difference in the first natural frequency when dropper 2 is removed is between 6% and 13%.

6.3.2 Second natural frequency

The same comparison that was done in Chapter 6.3.1, has been done for the second natural frequency. Figure 6.13 shows the comparison where all droppers are included.
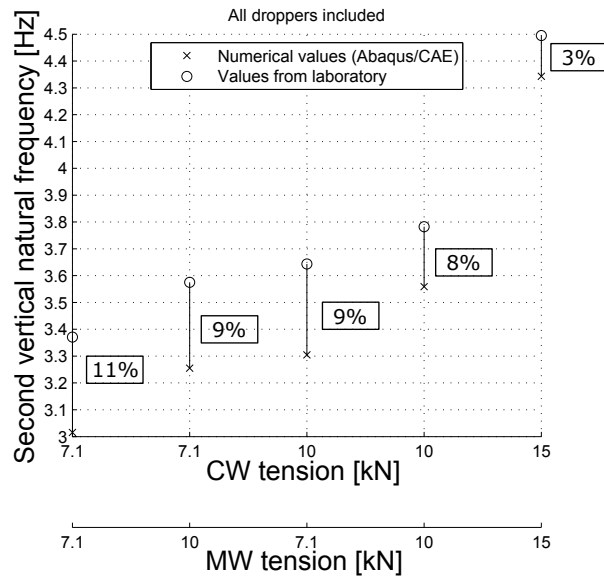
Figure 6.13: Tension in CW and MW plotted against first natural frequency, all droppers in-cluded.

The percent of error seems to be in the same order of magnitude as for the first natural fre-quencies, ranging from 3% to 11%. Finally, the comparison of the second natural frequency without dropper 2 is compared in Figure 6.14, where the error in frequencies are between 3% and 10%.
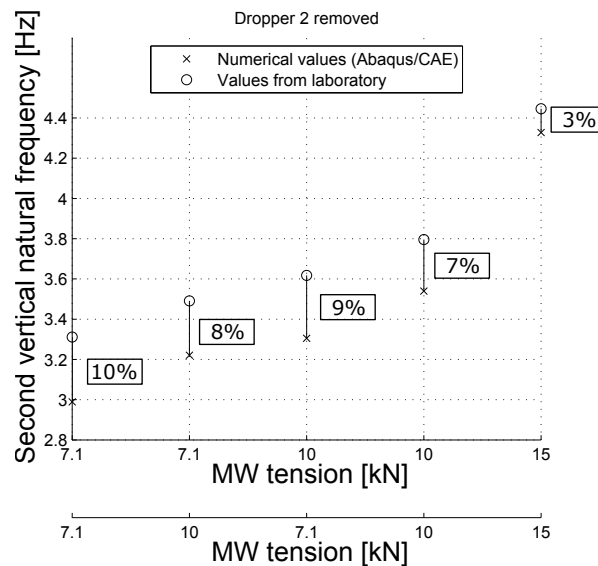
Figure 6.14: Tension in CW and MW plotted against second natural frequency, dropper 2 removed.

Table 6.7 sums up the percentage of error in natural frequency for all the different tension-combinations. As seen, the error ranges between 3% and 14% for all the different tension-combinations, with or without dropper 2 present in the system

Table 6.7: Percentage of error in natural frequencies, numerical vs laboratory

Tension-combination	First natural frequency		Second natural frequency	
	All droppers included	Dropper 2 removed	All droppers included	Dropper 2 removed
CW7.1kN-MW7.1kN	14%	12%	11%	10%
CW-7.1kN - MW-10kN	8%	11%	9%	8%
CW-10kN - MW-7.1kN	12%	11%	9%	9%
CW-10kN - MW-10kN	11%	10%	8%	7%
CW-15kN - MW-15kN	7%	6%	3%	3%

6.3.3   Discussion

All the natural frequencies calculated in Abaqus/CAE seems to be lower than the frequencies obtained in the laboratory, which is seen in Figure 6.11-6.14. This seems to be consistent, for all the different tension-combinations, with and without dropper 2 present in the system. However, the trend in frequency, for different tension-combinations, is of the same art for the numerical and the laboratory results.

A good example of the similar trend is shown for the first vertical natural frequency, with all droppers included (see Figure 6.11). In the figure, consider the change in frequency from the CW-7.1kN - MW-10kN combination, to the CW-10kN - MW-7.1kN combination. Both the laboratory results and the simulated results shows a drop in frequency due to this change in tension.

The mentioned drop in frequency happens when the tension in the contact wire is *increased* from 7.1kN to 10kN, while the messenger wire tension is *decreased* from 10kN to 7.1kN. This drop in frequency implies that the first natural frequency seems to take higher values when the tension in the messenger wire is higher than the tension in the contact wire. Since the natural frequency is directly dependent on the stiffness and the mass of the system (see Chapter 2.4), this drop in frequency may indicate that the applied force in the messenger wire contributes more to the system stiffness than the applied force in the contact wire does.

Hence, the global stiffness of the system may increase more for increased tension in the messenger wire than in the contact wire, which thus increases the natural frequency of the

model. This is reasonable, since the messenger wire supports the contact wire via the droppers, and carries more vertical load than the contact wire. Thus, a further increase in the contact wire tension may not affect the system stiffness as much as a further increase in tension in the messenger wire will do.

It was not only the first vertical natural frequency (all droppers included) that showed equal trend in the two models. The trend in natural frequency seemed to be the same for all the different tension-combinations mentioned in Chapter 6.3. The error for the different combinations that was summed up in Table 6.7 shows that the deviation between the numerical and laboratory results is rather consistent. The error was between 3-14% for all the different tension-combinations, with or without dropper 2 present in the system. Since the error was somewhat consistent, it implies that the modelling has been done in a reasonable way, and the error may relate to assumptions and simplifications made when creating the finite element model.

Note that the error in natural frequencies between the numerical and laboratory model was lowest when the tension in both wires were set to 15kN, for all the results presented. This is reasonable, particularly due to the applied tension in the models. The tension applied in the wires in the laboratory model, was slightly lower than the tension applied in the numerical model (see Table 6.3) for the CW-15kN - MW-15kN tension-combination. This results in a lower contribution to the geometric stiffness in the laboratory model, compared to the numerical model. The latter emphasizes the importance of correct tension in the wires, to achieve enough contribution from the geometric stiffness to the total stiffness matrix. It also proves that since the CW-15kN - MW-15kN tension-combination included the smallest percentage of error, the numerical model has been modelled slightly softer than the laboratory model.

The maximum error due to natural frequencies obtained in the numerical model and the laboratory model was approximately 14%. An explanation to this may be due to the simplifications made when modelling the cross sections of the messenger wire and the droppers. The cross sections of these components were modelled with nominal areas, which was greater than the effective areas. This would primarily influence the messenger wire and the droppers by:

- The axial stiffness (when considered as a beam) would increase, due to increased cross sectional area.

- The axial stiffness (when considered as a wire) would be unchanged, due to the application of the same axial force.

- The mass per unit length would increase due to increased cross sectional area.

Since the axial stiffness of the wires primarily is gained from the axial force in the wires ((Kiessling et al., 2009), (Ambrósio et al., 2012), (Poetsch et al., 1997)), it is reasonable to assume that the increase in mass of the messenger and the contact wire would be the main reason for the lower values of natural frequency in the numerical model compared to the laboratory model. A higher modal mass will reduce the natural frequencies of the system (see Equation 2.14).

To sum up:

- The natural frequencies obtained in the numerical model was *lower* than the values obtained in the laboratory.

- The same trend in natural frequency development was found in the numerical model as in the laboratory model.

- The wrong input of the mass in the numerical model, is likely the reason for the lower natural frequency obtained.

6.4   Elasticity along span

In chapter 3.5.2, it was explained how the elasticity along the model was measured in the laboratory, and the results obtained for the tension-combination CW-10kN - MW-10kN (all droppers included) are summed up in Table 6.8. The measurements for each point were done four times in the laboratory, and the average value for the four measurements in each point, and the respective standard deviation is presented.

Table 6.8: Elasticity along span, measured in laboratory

Point	Elasticity [mm/N]	Standard deviation [mm/N]	Point	Elasticity [mm/N]	Standard deviation [mm/N]	Point	Elasticity [mm/N]	Standard deviation [mm/N]
e1	0.0866	0.0102	**e7**	**0.1070**	**0.0102**	e13	0.2090	0.0102
e2	0.1274	0.0102	e8	0.1376	0.0102	e14	0.1733	0.0188
e3	**0.1070**	**0.0102**	e9	0.1172	0.0102	**e15**	**0.0663**	**0.0102**
e4	0.2141	0.0118	e10	0.1172	0.0102	e16	0.1427	0.000
e5	0.2294	0.0102	**e11**	**0.0866**	**0.0102**	e17	0.0815	0.000
e6	0.1886	0.0102	e12	0.1886	0.0102			

The points in Table 6.8 that are marked with bold letters relate to the points where the droppers are present along the span (see Figure 3.34).

In Abaqus/CAE, the same procedure as explained in chapter 3.5.2 was performed to compute the elasticity along the span. A vertical force of 49.1N was applied in each point, and the accompanying vertical displacement was registered. The comparison between the laboratory results and the results obtained in Abaqus/CAE is showed in Figure 6.15, where the values of elasticity obtained in the laboratory are taken from Table 6.8.
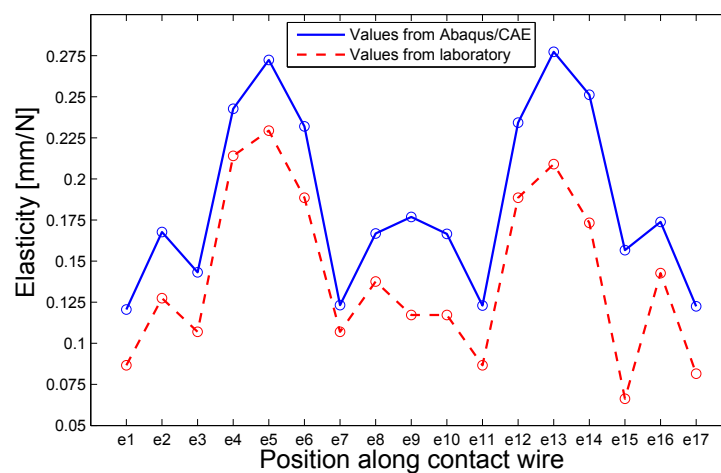
Figure 6.15: Comparison of elasticity along span, CW-10kN - MW-10kN as tension-combination.

6.4.1 Discussion

First of all, the droppers seems to generate a drop in elasticity along the span, which is equivalent to an increase in vertical stiffness. This is clearly shown in Table 6.8, where the values both prior to a dropper point, and after a dropper point are higher than the value in each dropper point. This also agrees with the theory of existing OCLs, which states that the droppers will increase the vertical stiffness (Kiessling et al., 2009).

Note that the cantilevers at the endpoints in the laboratory model has been excluded in the calculation of elasticity. This has been done since the cantilevers will be far more stiff than the rest of the system, and they would therefore have contributed to decrease the average elasticity of the laboratory model, which makes it less comparable to real catenary systems.

The average value of the elasticities shown in Table 6.8 was equal to ≈0.14mm/N. As mentioned in Chapter 2.1.2, the average elasticity for common high-speed OCLs was 0.5mm/N, which is approximately 3-4 times higher than the average elasticity of the laboratory model. Since the mass per unit length of the laboratory model is comparable to real OCLs (if the dropper spacing is assumed equal), this results insinuates that the laboratory model is roughly 3-4 times stiffer than existing OCLs, in the vertical direction.

As the Figure 6.15 shows, the elasticity obtained in the numerical simulation was greater than the elasticity obtained in the laboratory. This implies that the numerical model was less stiff in the vertical direction. The results also shows that the numerical model had more or less equal elasticity along both spans (left span: point e1-e9, right span: point e9-e17). The laboratory model did in contrast show a tendency of less elasticity for the right span.

The difference in stiffness in the two spans in the laboratory model may relate to: The position of the jacks relative to the sensors, and the steel chains that connects the jacks to the contact and messenger wire.

First of all, since the sensors that register the tension in the wires are installed on the left sided cantilevers (see Figure 3.2), it is possible that some of the tension applied by the jacks has been taken up at the support. This can however not be the case for the contact wire, which is free to move in the longitudinal direction due to the connection between the steady-arm and the registration arm (see Figure 3.12). By looking at the connection of the messenger wire to the top anchor shown in Figure 3.16, it is reasonable to assume that some of the tension in the messenger wire may have been lost/transferred to the top anchor as

friction.
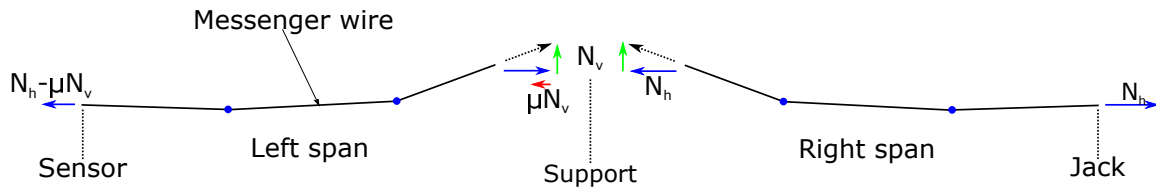
Figure 6.16: Loss of tension in the messenger wire, due to friction. μ: Friction coefficient, N_h: Horizontal force component, N_v: Vertical force component.

In Figure 6.16, N_h is the applied tension as a result of using the jack. N_h will then be a horizontally aligned force, which will be transferred through the messenger wire. Since the geometry of the messenger wire is irregular, a vertical force component will appear, market as N_v. This vertical component may thus contribute to fricton at the support, making the horisontal force in the left span less than in the right span. The loss of tension due to friction should however not be significant, due to the messenger wires possibility to be displaced in the longitudinal direction (along the model).

The steel-chains (see Figure 3.18) that connects the contact and messenger wire to the jacks may contribute to more stiffness in the right span, which seems more likely to be the reason for the deviation of elasticity between the two spans. The steel chains has not been included in the numerical model, where the elasticity seemed to be somewhat equal in both spans, which further substantiate this explanation.

The error between the elasticity obtained in the numerical model compared to the laboratory model is higher (see Figure 6.15) than it was in the comparison of natural frequencies. This may be related to uncertainties of the method performed (see Chapter 3.5.2). The method is quick and easy, but it includes several sources of error, which may be related to:

- Accuracy of the laser: The laser used in the measurements was only capable to perform measurements with an accuracy of millimeters.

- Weight/force: Keeping the dynamometer steady at exactly 5.0kg was not easy, and in addition to that, the dynamometer itself includes inaccuracy.

- Disturbance in the system: While doing the measurements, the contact wire may have been set into small motions, which could make the measurements less accurate.

- Human error: Both the person applying the force, and the person using the laser had to agreed when to take a measurement. Measurements may have been done for applied

forces that deviated from the wanted 49.1N.

Since the accuracy of the dynamometer used was restricted to millimeters, measuring with a larger vertical force than 5kg (49.1N) may have given better results, since the measured displacement may have been quantified more correctly, relative to the applied force.

Despite the error in elasticity, the trend seemed to be the same in both models. From Figure 6.15, it is easy to see which points that belongs to the droppers; the points with a slight drop in elasticity. This is also comparable to real OCL systems, where the droppers are included primarily to support the contact wire, and thus increase the vertical stiffness of the system. The fact that the elasticity shows consistency in both results, i.e the measured values in the laboratory stays below the simulated values along the entire model, indicates that the numerical model may be regarded as plausible due to the results of elasticity.

To sum up:

- Due to the measurements performed, the laboratory model seems to be 3-4 times stiffer than real OCLs.

- The elasticity obtained in the numerical model was higher than the values obtained in the laboratory, which indicates that the numerical model has been made softer than the laboratory model.

- The development in elasticity seems to be the same in both the numerical and the laboratory model.

6.5   Summary

The comparison of the elasticity along the span made in Chapter 6.4 showed that the numerical model was less stiff than the laboratory model in the vertical direction. In the comparison of the first and second natural frequency, the numerical model calculated lower frequencies than what was obtained in the laboratory. This further indicates that the numerical model may both be 1) less stiff, and/or 2) including higher mass, than the laboratory model. It was mentioned in Chapter 6.3.3 that the numerical model included a higher mass than the laboratory model, as a result of wrong inputs of different cross sectional properties. However, a lower mass included in the numerical model does not explain why the elasticity along the span appeared higher. The latter is likely related to the stiffness of the numerical model.

When using finite element calculations, a somewhat higher stiffness is expected due to the unnatural mathematical displacements forced by the interpolation functions (Cook et al., 2002). The latter statement contradicts the numerical model presented, and the question is then: Why is the numerical model less stiff than the laboratory model? There was not easy to find an obvious answer to this question, but one thing that may explain the reason is related to the following:

The beam section orientation of the beams created in the model. If the beam section orientation is chosen wrong, the cross sectional properties would not be represented correctly. This will most likely not have much impact if it was chosen wrong for the contact or the messenger wire, because 1) the stiffness obtained from the beam formulation of the wires will not contribute much to the global stiffness (Ambrósio et al., 2012), and 2) the cross sectional properties in the different directions are not differing significantly for these components (see Figure 3.8 and 3.9). However, the cantilevers at each end of the system has almost the double second moment of inertia about its strong axis, than about its weak axis (see Appendix B.1). When it was performed troubleshooting on the model, it was discovered that the beam section orientation of the cantilevers had been misinterpreted, and erroneously used in the model. The local cross sectional axes had been switched, making the strong axis become the weak axis (this mistake can be seen in Appendix D.2 under '## PROFILES INPUT→'# Cantilevers', where I11 has been switched with I22. This should have been the opposite, as shown in Appendix B.1). A test was performed with the correct beam orientation of the cantilevers, which increased vertical stiffness of the system. This may have been a reason for the numerical model being less stiff than the laboratory model. It also proves the importance

of using the correct beam orientation when modelling beams in Abaqus/CAE, and that the contribution to the vertical stiffness from the cantilevers at the endpoints may be significant.

Another factor that may have lead to a difference in stiffness between the two models is the calibration of the sensors that measured tension in the laboratory model. When troubleshooting the calibration of the sensors (see Fig 3.25), it was noticed that when the system was in a slack state (no tension applied in the wires), the tension given in the sensors was negative. This means that the sensors measured compression in the wires in a slack state, which intuitively is not possible. Thus, the actual tension applied in the wires may have been higher than what was registered in the sensors, which further may have contributed to a higher stiffness in the laboratory model than in the numerical model.

Further, the influence of assuming a reduced gravitational field should not have much impact on the analysis done. The altered gravitational field was, as mentioned, used to be able to model the correct initial conditions of the system in a slack state. Alternatively, one could have applied the correct gravitational field, and introduced an additional step in the analysis to *force* the geometry back to the wanted initial conditions. This was initially tried, but it was rejected due to the efficiency of the method: It is not easy to perform such an adjustment, and it is not certain that it actually has much effect on the results wanted to achieve.

Dispite the deviations in results, the development of both the natural frequencies and the the elasticity along the span showed the same trend in both the numerical and the laboratory model. Even though the numerical model seemed to be both less stiff, and more dense than the laboratory model, it may be regarded plausible, and it may be used to further investigate different trends and developments for the laboratory model.

Chapter 7

Parameter studies

In this chapter, two parameter studies are presented, which has been conducted with the use of the numerical model. These two studies involves:

- Development of natural frequency due to varying tension in the contact and messenger wire.

- Investigation of the effects the removal of either dropper 1 or dropper 2 have on the model, due to the first and the second natural frequency.

It should be mentioned that when referring to the first or second natural frequency, this means the first and second *vertical* natural frequency. This is important to notice, since not all the modes related to the first and second vertical natural frequency, was obtained as mode number 1 and 2 in the numerical model.

7.1   First natural frequency development

The idea with this parameter study was to investigate how the first vertical natural frequency was affected by varying the tension in the contact and messenger wire, and also investigate the results validity/difference due to theory of real OCL systems. Recall that the first natural frequency relates to the shape shown in Figure 3.27, where the system is vibrating as a half-sine curve in the vertical direction.

The tension-combinations chosen for this parameter study are related to common tension-combinations used in existing OCL systems, which are:

- CW-6.1kN - MW-5kN

- CW-7.6kN - MW-7.6kN (common for Table 54 (older versions))

- CW-10kN - MW-5kN (common for Table 54 (upgraded versions))

- CW-10kN - MW-10kN (common for System 20A and 20B)

- CW-15kN - MW-15kN (common for System 25)

The combinations mentioned in the list above are used as basis in the parameter study, since they relate to tensions that exist for real OCL systems, primarily used in Norway.

7.1.1   Method to obtain tension development

Since the tension in the contact and the messenger wire was created by applying a temperature field in the finite element model, it was necessary to use the method explained in Chapter 4.2.7 to find different combinations of tension in the contact and the messenger wire. Therefore, it is recommended that the reader gets familiar with the content in Chapter 4.2.7, before proceeding to read this chapter.

The iteration-scheme was performed by keeping either the contact or the messenger wire in constant tension, while the tension in the remaining wire was increased from 5kN to 20kN, with 0.5kN as increment. This leads to two definitions that are important to be aware of: When the expression *tension-combination* is used, this relates to a combination of tension in the contact and messenger wire in general. This can for instance be 5kN in the contact wire, and 7.5kN in the messenger wire. When the expression *tension-development* is used, this referres to a specific development in tension, when either the contact or the messenger

wire is set to take a constant value. For instance, a tension-development may relate to a contact wire tension of 5kN, and an increased messenger wire tension from 5kN to 20kN.

The tension-developments investigated in this parameter study are summed up in Table 7.1.

Table 7.1: Developments of tension

Development #	Wire with constant tension	Wire with increasing tension, from 5kN to 20kN
1	CW=6.1kN	MW
2	CW=7.6kN	MW
3	CW=10kN	MW
4	CW=15kN	MW
5	MW=5kN	CW
6	MW=10kN	CW
7	MW=15kN	CW

To explain the content in Table 7.1, take development #1 as example: The contact wire was applied 6.1kN tension, while the messenger wire was increased from 5kN to 20kN tension. For this specific tension-development, a total of ((20-5)·2-1)=31 tension-combinations had to be run in Abaqus/CAE.

As it was seven developments that was of interest, a total number of 7·31=217 analysis had to be run in Abaqus/CAE, where all the accompanying natural frequencies was extracted by solving the eigenvalue problem. To manually run 217 analysis is tedious work, which emphasizes the importance of being able to run several jobs after each other, without the need of manually starting all jobs. The latter was done by creating an additional python script, which could run many jobs in Abaqus/CAE. The mentioned Python script imported the values obtained in the iteration-scheme for the temperature changes needed, and run all the jobs subsequently after each other. To ensure that each increment in load was obtained correctly from the iteration scheme, each incremental tension-combination was checked manually in Abaqus/CAE. The procedure of how to 1) Gain the correct tension in the wires for each tension-combination, 2) Run all the different tension-combinations subsequently in Abaqus/CAE and 3) extract the wanted natural frequencies from each job, is explained in the flowchart shown in Figure 7.1.

1. The iteration-scheme created textfiles that contained the different values of temperature change needed, to obtain the correct value of tension.

2. The textfiles created was used as input to the Python script, which was created to run several jobs in Abaqus/CAE.

3. An additional code was written in the script, to extract the wanted natural frequencies. The natural frequencies was extracted from the .dat file Abaqus/CAE creates after running a job.

4. The natural frequencies obtained in each *tension-combination*, for all *tension-developments*, was written to new textfiles that could be treated efficiently.

Figure 7.1: Procedure to obtain the tension-developments and accompanying natural frequencies in Abaqus/CAE, with the use of Python.

7.1.2 Results

Note that all results in this chapter relates to the tension-developments explained in Chapter 7.1.1, and all droppers has been included in the model. The difference between increasing the tension in the contact wire and the messenger wire was inspected. This was initially done by letting either the contact or the messenger wire take a constant value of tension equal to 10kN, and increasing the tension in the remaining wire. Figure 7.2 a) and b) shows how the first natural frequency of the system develops as the tension in the contact and messenger wire are increased, respectively.
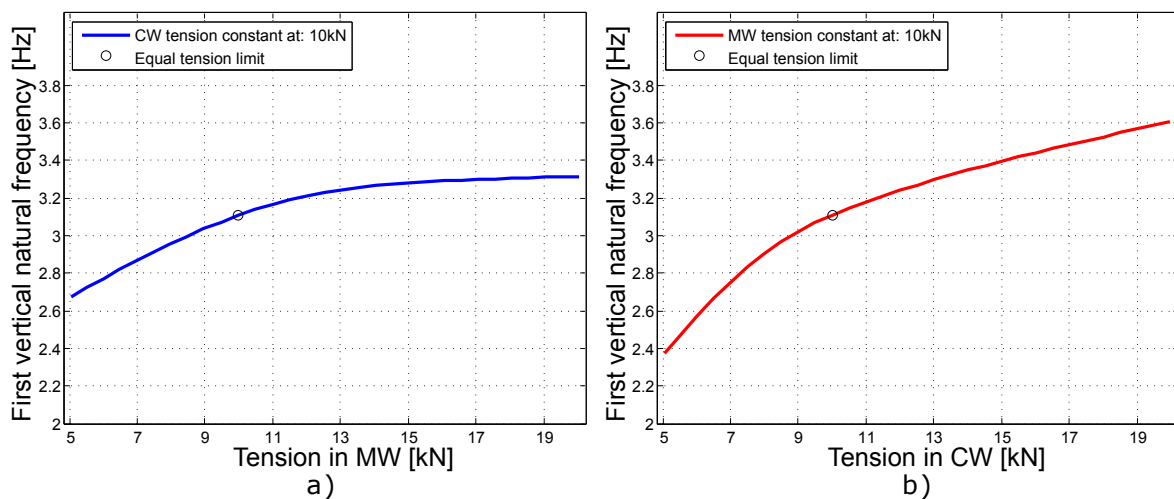
Figure 7.2: Tension in wires plotted against first natural frequency: a) CW constant at 10kN, MW increasing tension, b) MW constant at 10kN, CW increasing tension.

First of all, a definition due to Figure 7.2 has been made. The CW-10kN - MW-10kN combination has been defined as the "equal tension limit" in the figure. This definition will be used to sep-

arate the two developments as before and after the "equal tension limit". If the two graphs were plotted together, this limit would define the intersection between the two graphs.

In Figure 7.2 a), the curve represents the development in first natural frequency for a constant contact wire tension equal to 10kN, where the x-axis relates to the increased tension in the messenger wire. Figure 7.2 b) are plotted in the same fashion as Figure 7.2 a), but where the messenger wire is set to a constant tension of 10kN, while the contact wire tension is varied along the x-axis.

Inspect Figure 7.2 for tensions on the x-axis up to the point where both wires has equal amount of tension (hence, inspect the development *before* the "equal tension limit"). In this interval, the highest frequency is obtained by letting the contact wire tension be constantly equal to 10kN, and letting the messenger wire tension increase from 5-10kN. This indicates that the contact wire tension has more effect on the systems first natural frequency than the messenger wire, for tension-combinations below the "equal tension limit".

The roles are however changed if the second interval on the x-axis are inspected (hence, development *after* the "equal tension limit"). In this interval, the development of natural frequency due to constant contact wire tension seems to flatten out (Figure 7.2 a)), while the development in natural frequency for constant messenger wire tension seems to approach a linear trend (Figure 7.2 b)).

These two trends are thus inspected further, to investigate whether the trends randomly occured for the constant tension of 10kN, or if it can be made as a model characterization in general.

Thus, the first natural frequency development for different contact wire tensions, with increasing messenger wire tension, is showed in Figure 7.3.
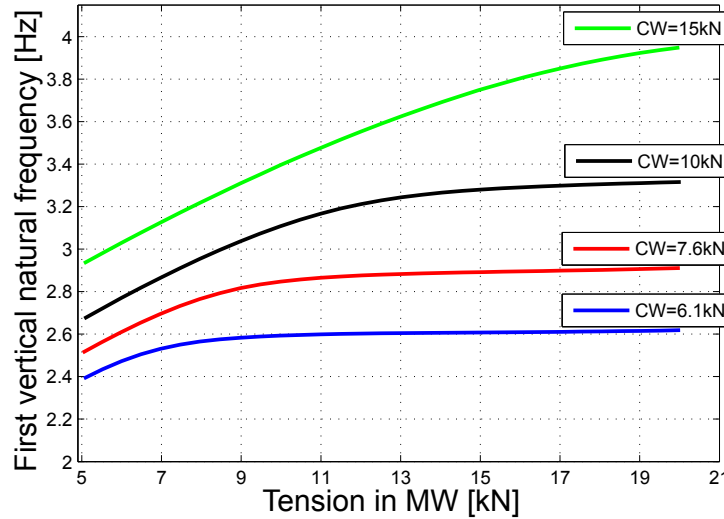
Figure 7.3: Increased tension in the MW plotted against first natural frequency, for different constant tensions in the CW (all droppers included).

In Figure 7.3, the contact wire tension has been set constant to four different values: 6.1kN, 7.6kN, 10kN and 15kN. The first natural frequency was plotted against the messenger wire tension. Note that the development for a constant tension in the contact wire of 10kN resembles the exact same development as shown in Figure 7.2 a).

Figure 7.3 shows that the development of the first natural frequency, due to a constant tension in the contact wire, is approaching a constant value for high values of tension in the messenger wire. The flattening trend is especially visualized when the contact wire is set to 6.1kN, 7.6 and 10kN. It is not visualized as clearly for a contact wire tension equal to 15kN, but this is most likely related to the maximum range of tension in the messenger wire. If tensions beyond 20kN in the messenger wire were accounted for, it is reasonable to assume that the same trend would have appeared for a constant tension of 15kN in the contact wire as well.

Further, the development of the first natural frequency, for different constant messenger wire tensions are showed in Figure 7.4.
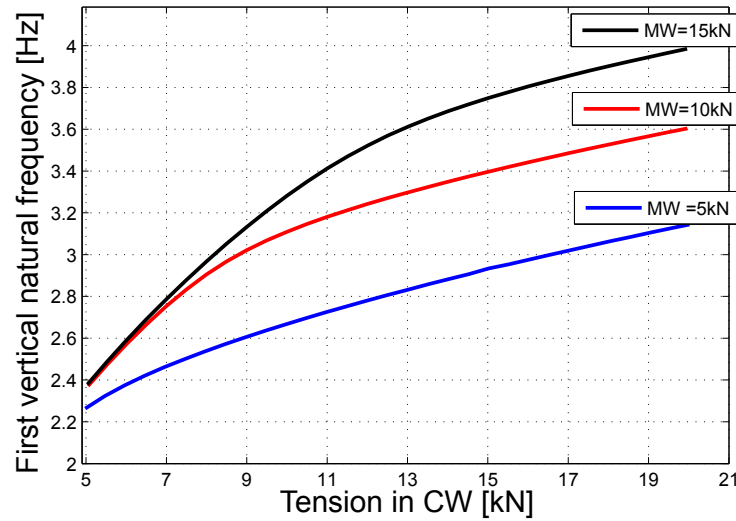
Figure 7.4: Increased tension in the CW plotted against first natural, for different constant tensions in the MW (all droppers included).

In Figure 7.4, the messenger wire has been set constant to three different values: 5kN, 10kN and 15kN. The first natural frequency was plotted against the contact wire tension. The linear trend mentioned earlier seems to be consistent for all the three different values of tension in the messenger wire.

It is of further interest to compare the developments obtained in the numerical model, with theoretical calculations. In the theory presented in Chapter 2.3, a simplified method of calculating the first natural frequency for real OCLs was presented (see Equation 2.4). The development obtained by the use of the theoretical expression is showed in Figure 7.5, where the contact wire tension was kept at 10kN and the messenger wire tension was increased along the x-axis. It was not necessary to plot several curves (as was done in Figure 7.4 and 7.3) to see this development, since the only difference would be a shift of the plot along the natural frequency axis. Hence, the development in natural frequency obtained in the theory would be unchanged, whether the constant value of tension in the contact wire was set to 5kN,10kN or any other value.
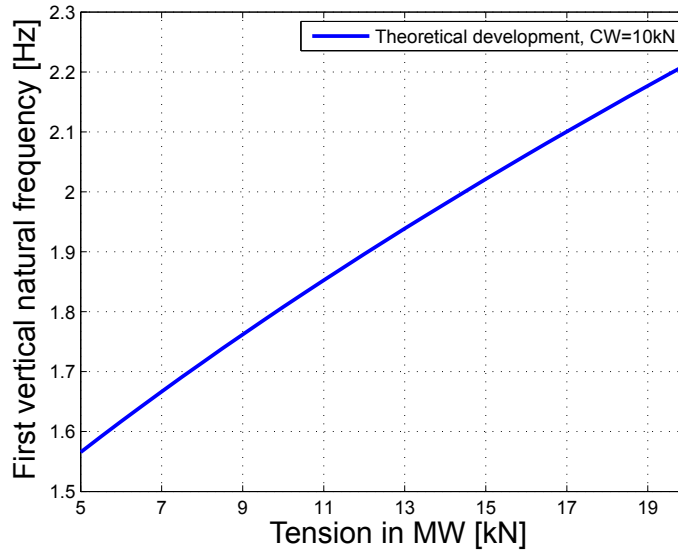
Figure 7.5: Increased tension in MW plotted against first natural frequency, theoretical values.

Note that the values[1] of frequency was of interest to compare, since the laboratory model deviated from real OCLs. It is the development that is of interest. Another thing worth mentioning is that Figure 7.5 will remain unchanged if the tension in the messenger wire was set to 10kN (instead of the contact wire), due to Equation 2.4.

7.1.3   Discussion

In the development of the first natural frequency, for different tension variations in the contact and messenger wire, some key observations were made:

- By letting the contact wire tension be constant, and increasing the messenger wire tension, the first natural frequency seemed to increase to a certain level, and then remain constant as the messenger wire tension was further increased (see Figure 7.3).

- By letting the messenger wire tension be constant, and increasing the contact wire tension, a different trend appeared. After reaching a certain level of tension in the contact wire, the development seemed to approach a linear trend (see Figure 7.4).

The reason for the two different developments in frequency may be related to the geometry of the system, in combination with the first mode shape. The mode shape related to the first

---

[1]The input used for the mass per unit length of the wires, and the length of the system are: L=30m, m'_{CW}=1.09kg/m, m'_{MW}=0.61kg/m (obtained from Table 3.1 by the use of g=9.81m/s^2)

natural frequency obtained in the numerical model is showed in Figure 3.27. By looking at the mode shape, it is noticed that the contact wire is the most displaced wire in the system, since the span is twice as long as the span of the messenger wire. If the contact wire is set hold a constant tension, and increasing the tension in the messenger wire, it is possible to assume that the first natural frequency of the system will increase until the geometry of the messenger wire are lifted to its maximum height. The point is showed in Figure 7.6.
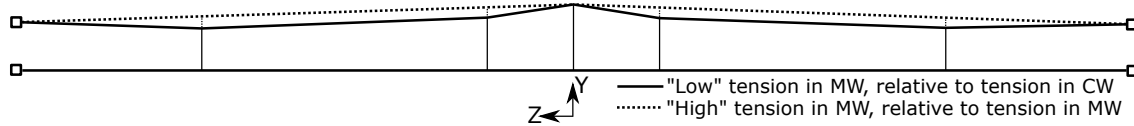
Figure 7.6: Geometric change by increase of tension in MW, when CW tension is constant.

After the system has taken the shape marked with the dotted lines in Figure 7.6, a further increase of tension in the messenger wire may not lead to further increase in natural frequency. This insinuates that the system in this state has reached its *cap* due to stiffness, and a further increase in messenger wire tension will not increase the *system* stiffness any more. The latter is clearly visualized in Figure 7.3, where the natural frequency approaches a constant value, when increasing the messenger wire tension.

This was not the case when the contact wire tension was increased, while the messenger wire tension was set to a constant value, which can be seen in Figure 7.4. The latter result indicates that for an increase in tension in the contact wire, where the messenger wire tension is kept constant, the natural frequency would keep increasing. Due to the theory presented (see Equation 2.4), the first natural frequency should increase for an increase in tension in either of the two wires.

When the results obtained in the numerical model was compared with the theoretical development, a special observation was made. The simplified calculation of the natural frequencies (see Equation 2.4) gave the same development whether the contact wire, or the messenger wire was kept at a constant value of tension. This contradics the results obtained in the numerical model, which primarily may be related to two things:

1. The simplified equation is not valid as a comparison between real OCL systems and the laboratory model.

2. The simplified equation is inconsistent due to the development of the first natural frequency, as a result of the numerical results gained.

The first bullet-point mentioned above is likely to be true, since the laboratory model differs from real OCLs. The cantilevers at the endpoints in the laboratory model are the prime reason for the difference, since they are not present in real OCLs. However, in the following discussion, it is assumed that the trend in first natural frequency obtained in the numerical simulations are directly comparable to real OCLs.

The second bullet-point mentioned is a statement that requires explanation. The statement is by no means meant to be interpreted as: "The simplified equation is invalid". It is meant to indicate that the use of Equation 2.4 may give ambiguous results. The ambiguity can be further explained by an example (which is hypothetical, but shows the point made): Consider an OCL system with the following properties:

- Span length: 30m (irrelevant to state the ambiguity).

- Mass per unit length: CW=1.0kg/m, CW=1kg/m (irrelevant to state the ambiguity).

- Tension used in the contact and messenger wire: 5kN and 10kN, or 10kN and 5kN, respectively.

This leads to the following first natural frequency, by the use of Equation 2.4:

$$f_1 = \frac{\sqrt{\frac{(H_{CW}+H_{MW})}{(m'_{CW}+m'_{MW})}}}{2L} = \frac{\sqrt{\frac{(H_{MW}+H_{CW})}{(m'_{CW}+m'_{MW})}}}{2L} = \frac{\sqrt{\frac{(10000+5000)\text{N})}{(1+1)\text{kg/m}}}}{2 \cdot 30\text{m}} = \underline{1.44\text{Hz}}$$

As observed, it does not matter which of the wires that are applied 5kN or 10kN tension; the first natural frequency will be the same. The same example was made in relation to the numerical model, and the following was obtained:

$$\text{CW=5kN, MW=10kN}: f_1 = \underline{2.37\text{Hz}} \quad \text{vs} \quad \text{CW=10kN, MW=5kN}: f_1 = \underline{2.67\text{Hz}}$$

For the numerical model, the difference in first natural frequency was approximately 11-12 %, as a result of whether it was the contact or the messenger wire that was applied 5kN or 10kN. This example states the ambiguity due to Equation 2.4. Thus, the numerical model may give more information about the actual development of the first natural frequency, than the simplified theory presented does.

To sum up:

- The development of first natural frequency seems to be dependent on whether it is the contact or the messenger wire that is applied the highest value of thension.

- By keeping the contact wire tension constant, and increasing the tension in the messenger wire, the first natural frequency seems to approach a constant value.

- By keeping the messenger wire tension constant, and increasing the tension in the contact wire, the first natural frequency seems to keep increasing, and approach a linear development.

7.2   Dropper removals effect on the natural frequency

The same procedure for analysis that was explained in Chapter 7.1.1 was performed two additional times: 1) Without dropper 1, and 2) without dropper 2 present in the system. Since the temperature changes needed to obtain the wanted level of tension in the wires had to be altered when either dropper 1 or dropper 2 was removed, the iteration-scheme explained in Chapter 4.2.7 had to be applied yet again, to find all the correct values of tension needed.

From the laboratory results (see Chapter 5.1), it was indicated that the first natural frequency was more affected by the removal of dropper 2, than the second natural frequency. In this chapter, this is further investigated. In addition, simulations without dropper 1 included in the system has been carried out, to further investigate the effect of droppers being disconnected along an OCL.

Even though there were found 7 different developments of the natural frequency vs tension in the wires (see Table 7.1), it is not necessary to include or comment all of them in this chapter, to be able to see which effect the removal of dropper 1 or dropper 2 has on the natural frequency. Therefore, four different developments (two of them relates to a constant tension in the CW, and the other two relates to constant tension in the MW) will be included in this chapter, which was assumed enough to get a general impression of the effect.

7.2.1 Results - dropper 2 removed

Figure 7.7 a) and b), and Figure 7.8 a) and b) shows how the first natural frequency are affected by the removal of dropper 2 (see Figure 3.26) from the system . The tension used in the different comparisons are included in the figures.
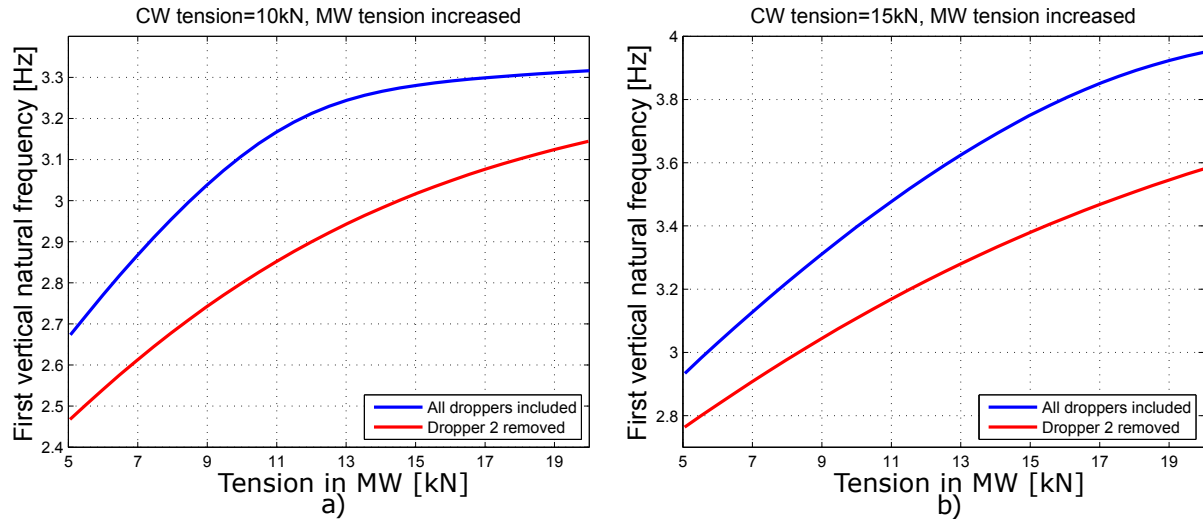
Figure 7.7: Tension in MW plotted against first natural frequency, dropper 2 removed comparison.
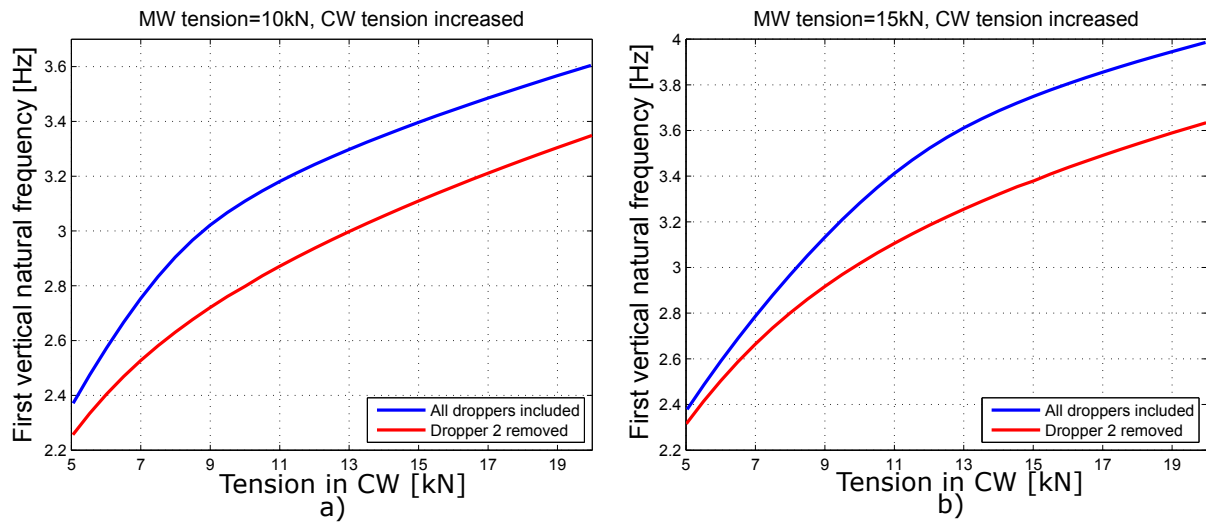
Figure 7.8: Tension in CW plotted against first natural frequency, dropper 2 removed comparison.

As seen in Figure 7.7 and 7.8, the first natural frequency seems to decrease when dropper 2 is removed. The same was obtained in the laboratory tests (see Chapter 5.1). The second natural frequency was not affected much by the removal of dropper 2 in the laboratory tests. The development of the second natural frequency are therefore also considered, which is

showed in Figure 7.9-7.10.
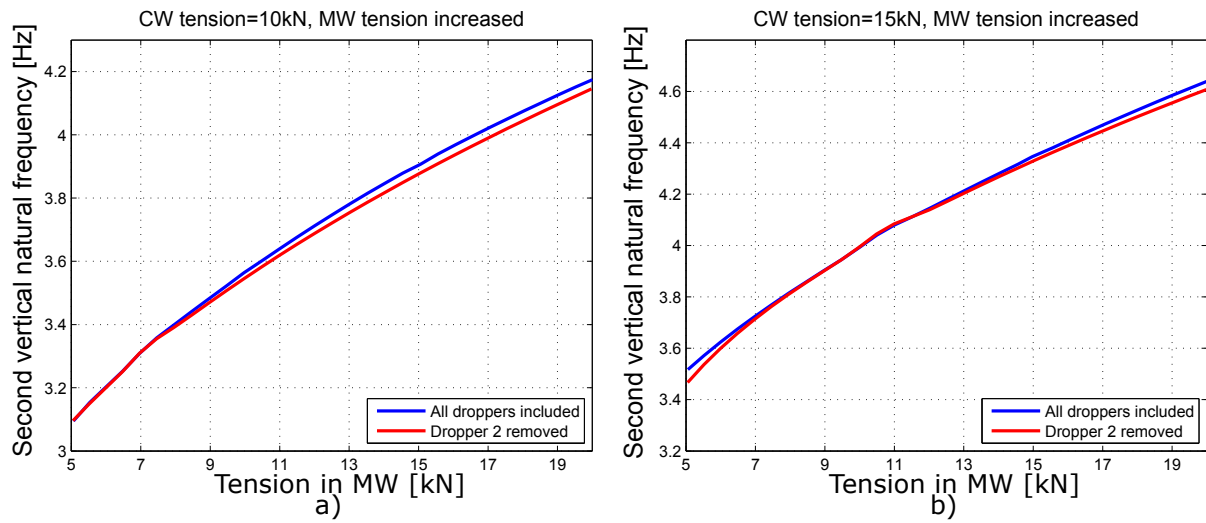
Figure 7.9: Tension in MW plotted against second natural frequency, dropper 2 removed comparison.
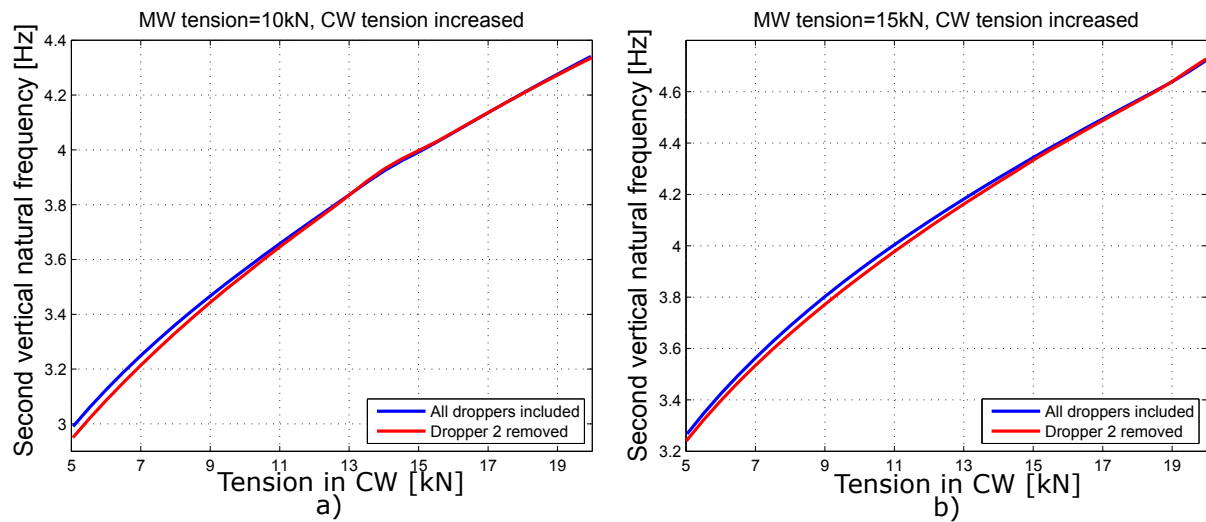
Figure 7.10: Tension in CW plotted against second natural frequency, dropper 2 removed comparison.

As in the laboratory tests, the second natural frequency does not seem to be affected for different developments of tension. This is clearly shown in Figure 7.9 and 7.10.

7.2.2 Results - Dropper 1 removed

In the laboratory tests, the removal of dropper 1 (see Figure 3.26) was never tested, and it is therefore not possible to compare this effect with the laboratory model. However, since the results obtained for the removal of dropper 2 showed the same tendency as obtained from the laboratory tests, it is possible to assume that the effect obtained in the numerical model, when the removal of dropper 1 is tested, is a plausible representation of the behavior of the laboratory model.

The effect of removing dropper 1, for the first natural frequency are shown in Figure 7.11 and 7.12. The same tension-developments that was used in Chapter 7.2.1 have been used in this comparison (i.e CW tension constantly equal to 10kN and 15kN, and MW tension constantly equal to 10kN and 15kN, while the remaining wire tension was increased, respectively).
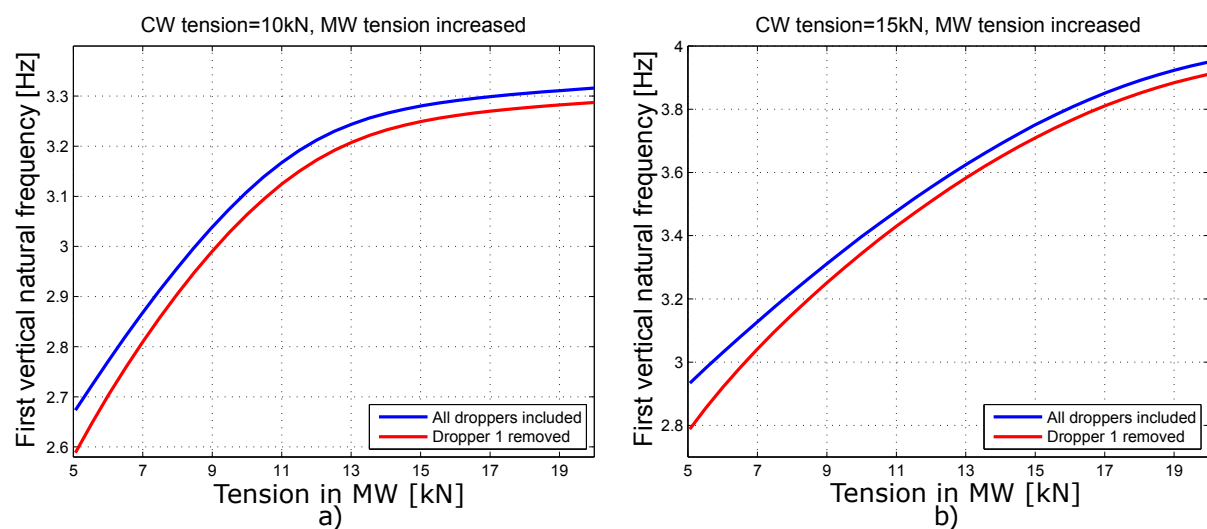
Figure 7.11: Tension in MW plotted against first natural frequency, dropper 1 removed comparison.
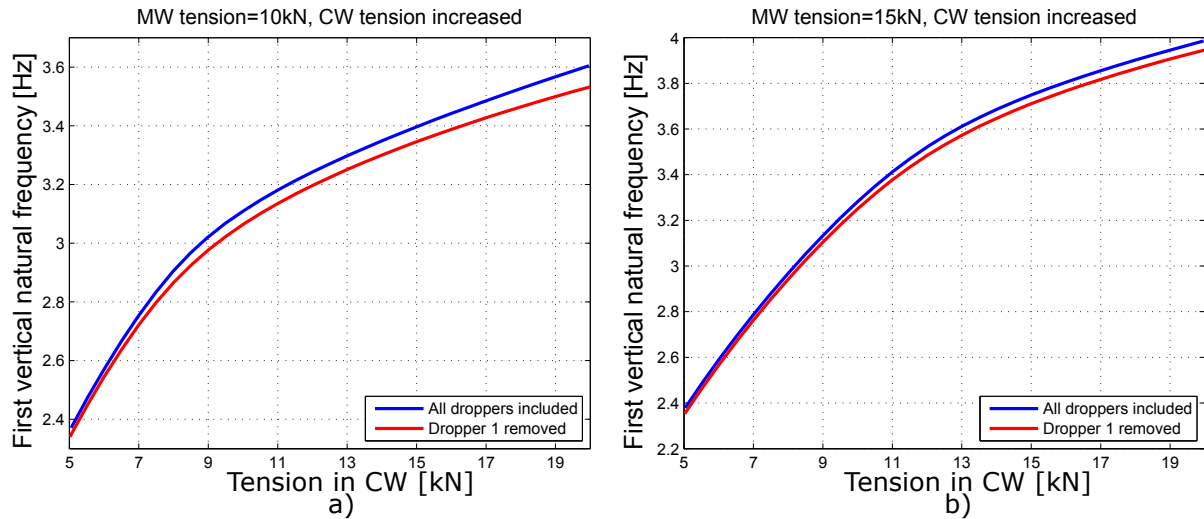
Figure 7.12: Tension in CW plotted against first natural frequency, dropper 1 removed comparison.

By looking at Figure 7.11 and 7.12, the first natural frequency does not seem to be much affected by the removal of dropper 1, compared to when dropper 2 was removed (see Figure 7.7 and 7.8).

Further, the development of the second natural frequency is compared with and without dropper 1 present in the system. This is showed in Figure 7.13, and Figure 7.14.
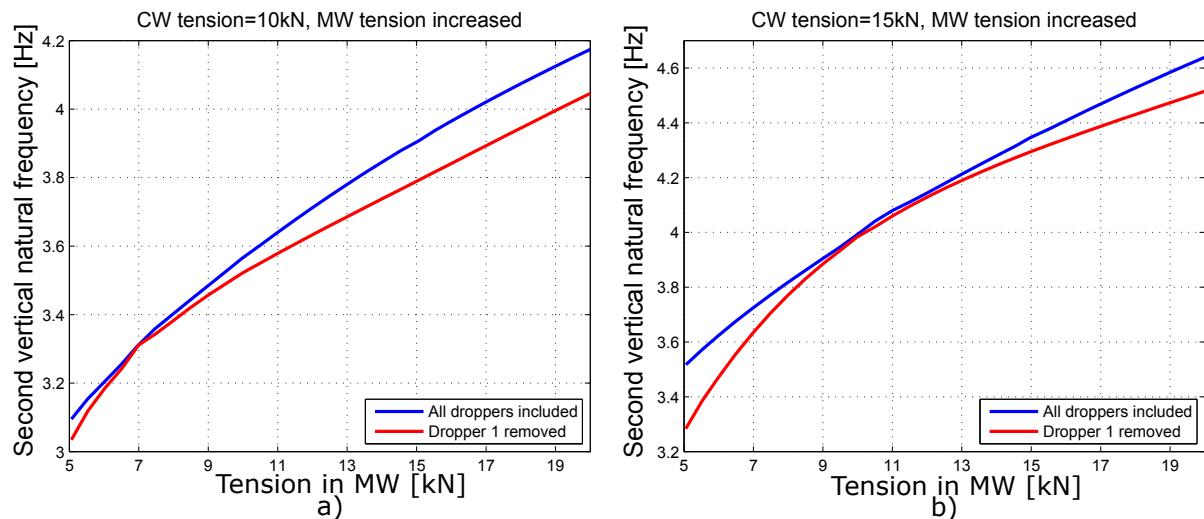
Figure 7.13: Tension in MW plotted against second natural frequency, dropper 1 removed comparison.
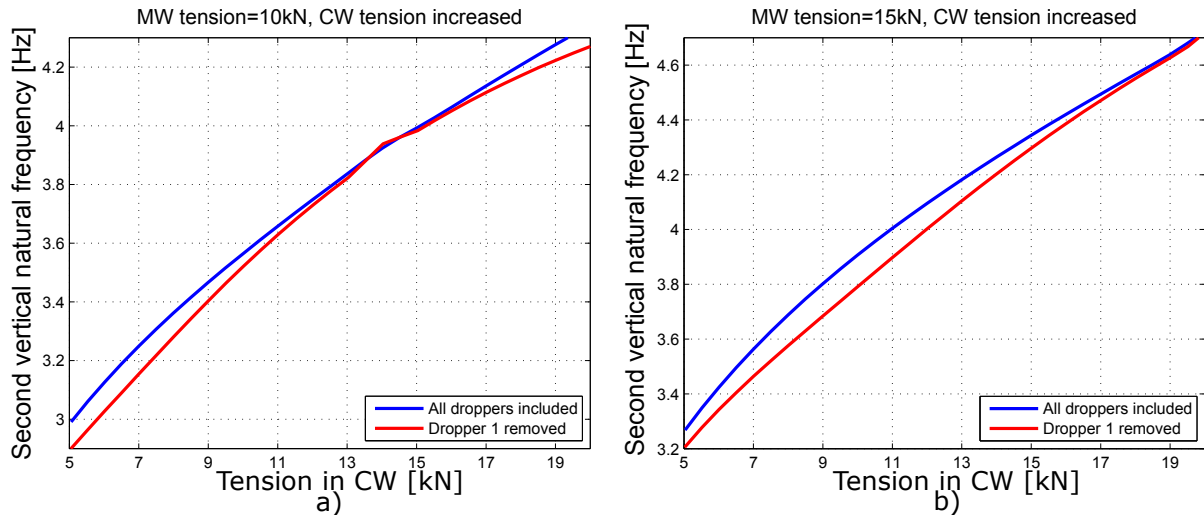
Figure 7.14: Tension in CW plotted against second natural frequency, dropper 1 removed comparison.

The development of the second natural frequency when removing dropper 1 (Figure 7.13 and 7.14) seems to be somewhat ambiguous, although it seems like it is more affected than what was obtained by the removal of dropper 2 (Figure 7.9 and 7.10).

7.2.3 Discussion

First of all, the removal of dropper 2 seemed to have more impact on the first natural frequency than it had on the second natural frequency. This was also found true in the laboratory results presented in Chapter 5.1. In the discussion of the natural frequencies obtained in the laboratory, a hypothesis about the removal of dropper 1 was proposed. It was stated that the removal of dropper 1 should have more impact on the second natural frequency than on the first natural frequency, in contrast to the removal of dropper 2.

This does not correlate with the results, since the deviation in the first natural frequency, when removing dropper 1, is hard to separate from the deviation in the second natural frequency (compare Figure 7.11 and 7.12 with Figure 7.13 and 7.14).

What can be said about the removal of dropper 1 for certain, is that the first natural frequency seems to develop in the exact same pattern as it did when all droppers was present in the system. This is visualized by the smooth and continuous development of both graphs in Figure 7.11 and 7.12. This was not the case for the development of the second natural frequency. The difference in the second natural frequency seemed to be more dependent on specific values of tension in the contact and messenger wire, which is clearly shown in Figure

7.14 and 7.13.

Consider Figure 7.13 b) as an example: The contact wire tension is set to 15kN, while the messenger wire tension is increased. For the tension-combination CW-15kN - MW-10kN, the resulting second natural frequency seemed to be the same when dropper 1 was removed, as when all droppers were present. This is shown by the two graphs in Figure 7.13 b) almost intersecting each other. In contrast, when the tension-combination CW-15kN - MW-20kN is considered in the same figure, the second natural frequency seemed to change by the removal of dropper 1. This shows that it is hard to explicitly determine the effect of removing dropper 1 from the system, in relation to the second natural frequency. It seems to have an effect, but the results are inconclusive to verify the earlier hypothesis made in Chapter 5.1, about the removal of dropper 1 leading to changes in the second natural frequency.

There is no doubt that by removing droppers from the model considered, the natural frequency will change. How much it changes are dependent on which dropper that is removed, which tension that is applied in the wires, and which of the first and the second natural frequency that is considered.

Summing up the affect the removal of a dropper from the model:

- By removing dropper 2, the first natural frequency was more affected than the second natural frequency. This was also found in the laboratory results, and the reason was assumed to be related to the decreased stiffness due to first the mode shape.

- The second natural frequency was not particularly affected by the removal of dropper 2, which also was found in the laboratory measurements. The reason was also here considered to be related to the mode shape, and that the removal of dropper 2 did not alter the stiffness related to this mode.

- The effect of removing dropper 1 seemed to have less effect than the removal of dropper 2. This result emphasizes that the effect of removing a dropper is dependent on the dropper position, and which magnitude of sag that are caused by the removal of a dropper. The latter was stated earlier, see Figure 5.3.

Chapter 8

Conclusion and further work

In this work, a numerical model which successfully describes a laboratory model of a catenary system has been made. In addition, a Python script has been generated to be able to make changes to this model, whenever changes are made in the physical model.

In particular, two analysis was made to validate the model, which involved the elasticity along the span of the model, and the first two natural frequencies. The results obtained can be summarized as follows:

- The numerical model showed the same development in natural frequency as the measurements made, and it was able to reproduce the accompanying mode shapes corrcetly.

- The values obtained for the natural frequency was slightly less in the numerical model than in the measurements, which likely related to 1) input of wrong mass in the numerical model, and 2) erroneous stiffness due to both cross sectional properties and tension applied in the wires.

- The development of the first two vertical natural frequencies showed the same trend in the numerical model, as obtained in the laboratory measurements.

- The development of the elasticity along the span showed the same tendancy as the measurements, but the numerical model turned out to be slightly softer than the laboratory model.

    ⇒ Despite that the numerical model turned out to be less stiff and more dense, than the laboratory model, it was considered plausible to use in further parameter studies

related to the development of natural frequencies.

In addition to validating the numerical model, two parameter studies were performed: (1) The development of the first natural frequency for varied tension in the contact and messenger wire, and (2) the effect of removing droppers from the system was considered. The results from the parameter studies may be summed up as:

- The first vertical natural frequency turned out to be dependent on which of the contact and messenger wire that was applied a certain magnitude of tension, which was not explicitly defined in the background theory presented.

- The effect due to natural frequency, by the removal of a dropper, seemed to be dependent on two things: 1) The position of the dropper along the span and 2) which of the first and the second natural frequency that was of interest.

- It was found that the effect of removing a dropper in the laboratory model, turned out to have more effect on the first natural frequency than the second natural frequency.

The challenges for further work, in relation to the numerical model, may be summed up as:

- Perform studies on natural frequencies higher than first and the second mode, since the dynamics related to the interaction between the pantograph and the contact wire relates to higher modes as well.

- Include the correct gravitational field in the model, the steel chains that connects the jacks, and model the connections at the support more accurately than was done in this study.

- Run simulations with Euler-Bernoulli beam elements instead of Timoshenko beam elements, to reduce the computational time.

- Model the messenger wire and droppers with a more correct representation due to the cross sections, for instance by the use of generalized cross sections.

- When comparing numerical analysis with measurements, reduce the sampling frequency to a minimum, to decrease the computational costs of each analysis.

- Further investigate the damping of the system, by iterations in an improved numerical model.

- Improve the Python script to include profile specifications, and to be able to select which type of analysis that is wanted to run on the model.

- Investigate the development of the first natural frequency for existing OCLs, and check whether the conclusion found in thesis can be drawn for real OCLs.

Bibliography

Ambrósio, J., Pombo, J., Pereira, M., Antunes, P., and Mósca, A. (2012). A computational procedure for the dynamic analysis of the catenary-pantograph interaction in high-speed trains. *Journal of Theoretical and Applied Mechanics*, 50(3):681–699.

Cho, Y. H., Lee, K., Park, Y., Kang, B., and Kim, K.-n. (2010). Influence of contact wire pre-sag on the dynamics of pantograph–railway catenary. *International journal of mechanical sciences*, 52(11):1471–1490.

Chopra, A. K. (2007). *Dynamics Of Structures*. Pearson Education, Upper Saddle River, NJ 07458.

Cook, R., Malkus, D., Plesha, M., and Witt, R. (2002). *Conceps and Applications of Finite Element Analysis*. John Wiley and Sons Inc, 111 River Street, NJ 07030, United States.

Dep. of Structural Engineering (2014). Lecture 9: Damping of structures. Lecture notes TKT4201 - Structural dynamics.

Hibbeler, R. C. (2013). *Statics and mechanics of materials*. Pearson Higher Ed.

HMH (1992). Kontaktledningsanlegg ekstruderte aluminiumsror utligger - system 20 og 25. Technical Report E-7291, Jernbaneverket. Revised version 2.

Jernbanekompetanse (2014). Mekanisk Systembeskrivelse av Kontaktledningsanlegg. [Online]. Available at: http://www.jernbanekompetanse.no/wiki/Mekanisk_systembeskrivelse_av_kontaktledningsanlegg#Ledningsf.C3.B8ring. [Accessed 9 May 15].

Jernbaneverket (2012). *Slik fungerer jernbanen*. Jernbaneverket, Oslo Norway.

Kamphuis, J. W. (2010). *Introduction to coastal engineering and management*, volume 30. World Scientific.

Kiessling, F., Puschmann, R., Schmieder, A., and Schneider, E. (2009). *Contact Lines for Electric Railways.* Publicis Publishing, Erlangen Germany.

Kistler (2014). Datasheet: Ceramic/Quartz Impedance Head for Modal Analysis Type 8770A. [Online]. Available at: http://www.intertechnology.com/Kistler/Accelerometers_Model_8770A.htm. [Accessed 9 May 15].

Labonnote, N. (2012). *Modal hammer for dummies.*

Massat, J., Laine, J., and Bobillot, A. (2006). Pantograph–catenary dynamics simulation. *Vehicle System Dynamics*, 44(sup1):551–559.

Mathisen, K. M. (2014). Lecture 13: Stress stiffness and bucling analysis. Lecture notes TKT4197 - Nonlinear finite element analysis.

National Instruments (2015). NI cDAQ-9174. [Online]. Available at:http://sine.ni.com/nips/cds/view/p/lang/no/nid/207535. [Accessed 9 May 15].

Nåvik, P. R. (2013). Numerical Analysis of the Dynamic Behaviour of Railway Catenary Systems in Accordance with Norwegian Conditions. Master's thesis, Norwegian University of Science and Technology, Trondheim.

NKTCables (2008). We deliver traction power to the Railway... [Online]. Available at:http://www.nktcables.com/~/media/Files/NktCables/download%20files/com/Railway_ProduktbroschureUK.pdf. [Ac].

Oura, Y., Mochinaga, H., and Nagasawa, H. (1998). Railway electric power feeding systems. *Japan Railway and Transport Review*, 16(3):48–58.

Pesola (2008). Item no. PHS040 - Digital Hanging Scale 40kg / 88Lb. [Online]. Available at: http://www.pesola.com/cgi-bin/shop?r0=user&r1=show&r2=item&itemId=360&lang=en_US. [Accessed 9 May 15].

Poetsch, G., EVANS, J., Meisinger, R., Kortüm, W., Baldauf, W., Veitl, A., and Wallaschek, J. (1997). Pantograph/catenary dynamics and control. *Vehicle System Dynamics*, 28(2-3):159–195.

Siemens (2015). Contact line for mass transit. [Online]. Available at: http://w3.usa.siemens.com/mobility/us/en/urban-mobility/rail-solutions/

`railway-electrification/contact-line-for-mass-transit/pages/`
`contact-line-for-mass-transit.aspx`. [Accessed 9 May 15].

SIMULIA (2012). *Abaqus 6.12 Scripting User's Manual.* Dassault Systémes, Providence, RI, USA.

SIMULIA (2014). *Abaqus/CAE User's Manual.* Dassault Systémes, Providence, RI, USA.

Strømmen, E. N. (2014). *Structural Dynamics.* Springer.

The MathWorks Inc (2015). Matlab Documentation.

Valle, H. (2014). Testing av laboratorierigg av kontaktledningsanlegg. *Rapport fra sommer-jobb 2014 for Jernbaneverket.*

Van Rossum, G. (2015). *Python Tutorial, Release 2.7.10rc0.*

Weisstein, Eric W (2015). Fast Fourier Transform. [Online]. Available at: `http://mathworld.wolfram.com/FastFourierTransform.html`. [Accessed 9 May 15].

WordPress (2010). Pantographs and the Overhead Wire. [Online]. Available at: `https://maxfaqs.wordpress.com/2010/07/28/pantographs-and-the-overhead-wire/`. [Accessed 9 May 15].

Appendix A

Abaqus/CAE additional inputs/outputs

This appendix includes additional inputs and outputs related to the numerical model.

A.1   Second and third mode obtained in eigenvalue problem

This appenix shows the second and the third mode obtained by solving the eigenvalue problem in Abaqus/CAE, which are related to motion out of the vertical plane.

Mode 2

ODB: FindTemp.odb   Abaqus/Standard 6.14 1   Sat May 30 10:19:52 W. Europe Daylight Time 2015

Step: Frequency
Mode   2: Value = 446.40   Freq = 3.3626   (cycles/time)
Deformed Var: U   Deformation Scale Factor: +1.000e+00

Mode 3

ODB: FindTemp.odb   Abaqus/Standard 6.14 1   Sat May 30 10:19:52 W. Europe Daylight Time 2015

Step: Frequency
Mode   3: Value = 459.59   Freq = 3.4120   (cycles/time)
Deformed Var: U   Deformation Scale Factor: +1.000e+00

A.2   Temperature field to obtain tension

This appendix shows which temperatures that was used in the contact and messenger wire to obtain the tension-combinations used to validate the numerical model.

Tension-combination	Wire	Wanted tension [kN]	Temperature change: ΔT [K]	Obtained tension (Abaqus/CAE) [kN]	
				All droppers included	Dropper 2 removed
CW-7.1kN - MW-7.1kN	CW	7.10	60.20	7.08	7.06
	MW	7.10	162.10	7.07	7.08
CW-7.1kN - MW-10kN	CW	7.10	58.00	7.08	7.07
	MW	10.00	190.00	9.97	9.98
CW-10kN - MW-7.1kN	CW	10.00	83.00	9.98	9.95
	MW	7.10	160.00	7.10	7.12
CW-10kN - MW-10kN	CW	10.00	81.00	9.98	9.95
	MW	10.00	188.00	9.96	9.97
CW-15kN - MW-15kN	CW	15.00	117.0	14.98	14.96
	MW	15.00	233.0	15.00	14.96

A.3   Tension obtained in Abaqus/CAE, dropper 2 removed

This appendix shows the values of tension that was optained in the numerical model, when dropper 2 was removed.

Tension-combination		Wanted tension [kN]	Avarage tension [kN]	Standard deviation [kN]	Error in %
CW-7.1kN - MW-7.1kN	CW	7.100	7.059	0.001	0.6
	MW	7.100	7.081	0.002	0.3
CW-7.1kN - MW-10kN	CW	7.100	7.073	0.003	0.4
	MW	10.000	9.976	0.002	0.2
CW-10kN - MW-7.1kN	CW	10.000	9.949	0.004	0.5
	MW	7.100	7.119	0.005	0.3
CW-10kN - MW-10kN	CW	10.000	9.950	0.004	0.5
	MW	10.000	9.965	0.003	0.4
CW-15kN - MW-15kN	CW	15.000	14.960	0.004	0.3
	MW	15.000	14.960	0.004	0.1

Appendix B

Geometry of components

This appendix includes different geometric features.

B.1   Cross section of cantilevers

Note that the specification below is not in correct scale, it has been cropped to fit this page.

B.2 Cross section of contact wire, system 25

Note that the material definitions is not the same as the one used in the laboratory model (Ri 100 Cu instead of RiS 120 CuAg), but the cross sectional properties are correct.

CrossX Massive Report   **June 24. 2014**

z' = 6.9 mm

Base material:

Name: Ri 100 Cu
E = 1.240e+005 N/mm²
G = 4.470e+004 N/mm²
ν = 0.34
ρ = 8930.00 kg/m³

C = center of gravity
S = shear center

Angle (y',y) = 0.00 deg
y'_c = 0.0 mm
z'_c = -0.4 mm
y'_s = -0.0 mm
z'_s = -1.0 mm
y_s = -0.0 mm
z_s = -0.6 mm

True area
 1.2097e+002 mm²

Weight per unit length
 0.01 kN/m

Mass per unit length
 1.08 kg/m

z' = -6.9 mm

y' = -6.9 mm   Scale: 1:0.1189   y' = 6.9 mm

PARAMETER*	VALUE		STIFFNESS	VALUE
A	1.2097e+002 mm²		EA	1.5000e+004 kN
I_y	1.3442e+003 mm⁴		EI_y	1.6668e-001 kN·m²
I_z	1.1189e+003 mm⁴		EI_z	1.3875e-001 kN·m²
I_t	1.8446e+003 mm⁴		GI_t	8.2453e-002 kN·m²
S_y	1.9324e+002 mm³		GA_{sy}	4.5782e+003 kN
S_z	1.6954e+002 mm³		GA_{sz}	4.0406e+003 kN
r_y	3.3334e+000 mm			
r_z	3.0414e+000 mm		GA	5.4073e+003 kN
$κ_y$	1.18108			
$κ_z$	1.33822			
$I_{y'}$(y' at C)	1.3442e+003 mm⁴		$EI_{y'}$	1.6668e-001 kN·m²
$I_{z'}$(z' at C)	1.1189e+003 mm⁴		$EI_{z'}$	1.3875e-001 kN·m²
$I_{y'z'}$ (at C)	0.0000e+000 mm⁴		$EI_{y'z'}$	-2.2419e-017 kN·m²

* Apply to an equivalent cross section of base material

Appendix C

Input textfiles

This appendix involves the textfiles used in the Python script to create the model. In the files, comments are marked with #.

C.1 Geometry input

The drawing sequence for the coordinates of the contact and messenger wire are shown in Figure 4.2, and for the support in Figure 4.3.

Wire geometry

NB! Do not alter the vertical position of the coordinates. For instance: '#Messenger wire' is ROW 5
Points arranged in x,y,z. NB! Do not alter the number of coordinates in this file, only coordinate values.

# Messenger wire	# Local point
2.023931,4.793,14.348	# (2)
2.193,4.6325,9.676	# (4)
2.406,4.9145,2.244	# (6)
2.397,5.257,0	# (8)
2.388,4.9005,-2.241	# (10)
2.163,4.6485,-9.691	# (12)
2.000931,4.74,-14.399	# (14)

# Contact wire	# Local Point
2.023931,3.539,14.348	# (1)
2.193,3.519,9.676	# (3)
2.406,3.482,2.244	# (5)
2.337,3.47,0	# (7)
2.388,3.453,-2.241	# (9)
2.163,3.384,-9.691	# (11)
2.000931,3.452,-14.399	# (13)

Support geometry

Coordinate drawing are in the same order as the point-sequence given below

Top anchor - Point sequence: ABRD   # Local point

0.09,5.117,0   # A

2.14,5.117,0   # B

2.397,5.117,0   # R

2.597,5.117,0   # D

Cantilevered tube - Point sequence: EFG   # Local point

0.09,3.302,0   # E

0.8584,3.942,0   # F

2.14,5.027,0   # G

Registration arm dropper - Point sequence: HJ # Local point

2.20022,4.95817,0   # H

2.9684,3.922,0   # J

Registration arm - Point sequence: IOKLM   # Local point

0.9584,3.842,0   # I

2.4659,3.842,0   # O

2.9684,3.842,0   # K

3.1854,3.842,0   # L

3.3904,3.842,0   # M

Steady arm - Point sequence: PN   # Local point

2.4617,3.595,0   # P

3.1604,3.772,0   # N

C.2   Material input

This is the layout of the material input file, that is used in combination with the python script.

Material data - Arrangement in arrays:

[Material Name,E-module,Density,Poisson's ratio]

NB: POSITIONS OF DATA NOT EDITABLE

- System 25 -

Messenger wire

Bz 70/19 Messenger wire,120000000000,8890,0.34

Contact wire

RiS 120 CuAg Contact wire,120000000000,8890,0.34

Dropper

Bz 10/49 Dropper,120000000000,8890,0.34

Aluminium

Aluminium,70000000000,2700,0.35

Steel

Steel,210000000000,7800,0.3

C.3   Section input

This is the file that is used to assign the correct profiles to the different materials.

Section names and profiles. Organized in list as: [material,name,poissons ratio]

For example: [Bz 70/19 Messenger wire,Messenger wire,Messenger wire]

The wires connected to the cantilevers uses messenger wire data

Keep this sequence as it is, the script depends on correct positions of the data

RiS 120 CuAg Contact wire,Contact wire,0.34

Bz 70/19 Messenger wire,Messenger wire,0.34

Bz 10/49 Dropper,Dropper,0.34

Aluminium,Top anchor,0.35

Aluminium,Cantilevered tube,0.35

Aluminium,Registration arm,0.35

Steel,Registration arm dropper,0.3

Aluminium,Steady arm,0.35

Appendix D

Python scripts

This appendix involves the both Python and Matlabd scripts used in the thesis.

D.1   Geometry and sets input script

The drawing sequence given for the coordinates of the support are shown in Figure (vis figur av support-coordinatene).

```
# -*- coding: mbcs -*-
# Abaqus/CAE module import commands:
from part import *
from material import *
from section import *
from assembly import *
from step import *
from interaction import *
from load import *
from mesh import *
from optimization import *
from job import *
from sketch import *
from visualization import *
from connectorBehavior import *


########################### START OF GEOMETRY-SCRIPT ###############################
import numpy as np
import math
import subprocess
# Model geometry, input from textfile: "total_geometry.txt"
# The wire geometry is drawn from left end to right end, and the support is drawn from wall and out.
# The skip_footer/skip_header in the coord-lists, are dependant on how many coordinates each
component includes.
# The number of coordinates for each component is fixed in this script, and should NOT be altered.
# Values for each coordinate may however be altered
# The dropper coordinates are taken as the two points between the support and the left/right end of,
the system.
```

```python
## Which droppers to suppress
drSuppressable = ['Wire-3','Wire-4','Wire-5','Wire-6']
# drSuppressable is the wire features for Dropper 1-4.
# To suppress a dropper, include the dropper position in dropperSuppress.
# For instance, to suppress Dropper 2 and Dropper 3, simply type dropperSuppress = [2,3]
# NB! Do not type dropperSuppress = [3,2], as the script don't understand this sequence. Lowest int first.
# Maximum droppers to suppress is dropperSuppress = [1,2,3,4]
# Default: No suppressed droppers is dropperSuppress = []
dropperSuppress = []
# Number of eigenvectors (modes) in frequency step
numEigenVec = 4
## Number of coordinates for each component:
numMW = 7                    # Messenger wire
numCW = numMW                # Contact wire
numTopAnchor = 4             # Top Anchor
numCantTube = 3              # Cantilvered tube
numRegArmDropper = 2         # Registration arm dropper
numRegArm = 5                # Registration arm
numStdArm = 2                # Steady arm
numTot = numMW + numCW + numTopAnchor + \
         numCantTube + numRegArmDropper + \
         numRegArm + numStdArm
lengths = [numMW,numCW,numTopAnchor,numCantTube,\
         numRegArmDropper,numRegArm,numStdArm]


## Input coordinates for MW, CW, and support.
mwcoord = np.genfromtxt('total_geometry.txt', comments='#', skip_footer=(numTot-numMW),
          delimiter=',')
mwcoord = mwcoord.tolist()
```

```python
cwcoord = np.genfromtxt('total_geometry.txt', comments='#', skip_header=(14), \
           skip_footer=(numTot-numMW-numCW), delimiter=',')

cwcoord = cwcoord.tolist()

tacoord = np.genfromtxt('total_geometry.txt', comments='#', skip_header=(26), \
           skip_footer=(numTot-numMW-numCW-numTopAnchor), delimiter=',')

tacoord = tacoord.tolist()

ctcoord = np.genfromtxt('total_geometry.txt', comments='#', skip_header=(32), \
           skip_footer=(numTot-numMW-numCW-numTopAnchor-numCantTube), delimiter=',')

ctcoord = ctcoord.tolist()

radcoord = np.genfromtxt('total_geometry.txt', comments='#', skip_header=(37), \
           skip_footer=(numTot-numMW-numCW-numTopAnchor-numCantTube-numRegArmDropper),
           delimiter=',')

radcoord = radcoord.tolist()

racoord = np.genfromtxt('total_geometry.txt', comments='#', skip_header=(41), \
           skip_footer=(numStdArm), delimiter=',')

racoord = racoord.tolist()

sacoord = np.genfromtxt('total_geometry.txt', comments='#', skip_header=(48), \
           delimiter=',')

sacoord = sacoord.tolist()


# All wires/support components (except droppers) stored in array 'list_of_components'
list_of_components = [mwcoord,cwcoord,tacoord,ctcoord,radcoord,racoord,sacoord]


## Creating coordinates for sets
midCoordNames = ['mwMidpoint','cwMidpoint','taMidpoint' \
                 'ctMidpoint','radMidpoint','raMidpoint','saMidpoint']

midCoordinates = list()
for i in range(0,len(lengths)):
    midCoordinates.append([[1]*3]*(lengths[i]-1))
    for j in range(0,len(midCoordinates[i])):
        midCoordinates[i][j] = 0.5*np.add(list_of_components[i][j],list_of_components[i][j+1])
```

```python
for i in range(0,len(lengths)):
    for j in range(0,len(midCoordinates[i])):
        midCoordinates[i][j] = tuple(midCoordinates[i][j])
for i in range(0,len(lengths)):
    midCoordinates[i] = tuple(midCoordinates[i])
mwMidpoint,cwMidpoint,taMidpoint, \
ctMidpoint,radMidpoint,raMidpoint,saMidpoint = tuple(midCoordinates)


## Edited all component lists to fit as 'polyline wire' in Abaqus
for i in range(len(list_of_components)):
    for j in range(1,len(list_of_components[i])*2-3,2):
        list_of_components[i].insert(j,list_of_components[i][j])


## Converting lists to tuple, to operate correctly in Abaqus
for i in range(len(list_of_components)):
    k=0
    while (k < len(list_of_components[i])):
        list_of_components[i][k] = tuple(list_of_components[i][k])
        k = k+1


## Making the tuple in the arrangement Abaqus wants:
## ((coordinate1,coordinate2),(coordinate2,coordinate3)) etc for all components:
real_list_of_components = [0]*len(list_of_components)
for i in range(len(real_list_of_components)):
    real_list_of_components[i] = [0]*(lengths[i]-1)
[mwCoordinates,cwCoordinates,taCoordinates,ctCoordinates,radCoordinates, \
raCoordinates,saCoordinates] = real_list_of_components
```

```python
for i in range(len(real_list_of_components)):
    k=0
    while (k < (int(len(real_list_of_components[i])))):
        real_list_of_components[i][k] = tuple(list_of_components[i][k*2:k*2+2])
        k=k+1


## Droppers geometry: drCoordinates - gained from mw/cw
#Number of droppers included
numDr = 4
drCoord = [0]*10
for i in range(1,len(mwcoord)/2-1,2) + range(7,len(mwcoord)-1,2):
    drCoord[i-1] = cwcoord[i]
    drCoord[i] = mwcoord[i]
del drCoord[4:6]


drCoordinates = [0]*numDr
drNames = ['Dropper 1','Dropper 2','Dropper 3','Dropper 4']
k = 0
while (k <= (len(drCoord)/2-1)):
    drCoordinates[k] = tuple(drCoord[k*2:k*2+2])
    k=k+1


## Creating sinusoidal curve for registration arm dropper
# Number of points on registration arm dropper
numRegAD = 10
# Edited in positive global x-direction (negative y-dir)
# used radcoord for registration arm dropper coordinates
#Deflection amplitude:
radDefAmplitude = 0.01
```

```python
radcoord = [[radcoord[0][0],radcoord[0][1],radcoord[0][2]],\
            [radcoord[1][0],radcoord[1][1],radcoord[1][2]]]
radXLength = radcoord[1][0]-radcoord[0][0]
radYLength = radcoord[1][1]-radcoord[0][1]
radLength = math.sqrt(radXLength**2+radYLength**2)
angle = math.atan(radXLength/(radYLength*(-1)))
radDX = np.linspace(0,radXLength,numRegAD)
radDY = np.linspace(0,radYLength,numRegAD)
radDTot = [0]*len(radDX)
radDSin = [0]*len(radDX)
radDeltaX = [0]*len(radDX)
radDeltaY = [0]*len(radDY)
radCoordinates = list()
for i in range(0,len(radDX)):
    radDTot[i] =math.sqrt(radDX[i]**2+radDY[i]**2)
    radDSin[i] =math.sin(radDTot[i]*np.pi/radLength)
    radDeltaX[i] = math.cos(angle)*radDSin[i]*radDefAmplitude
    radDeltaY[i]= math.sin(angle)*radDSin[i]*radDefAmplitude
for i in range(0,(len(radDeltaX))):
    radCoordinates.append([radcoord[0][0]+radDeltaX[i]+radDX[i],\
    radcoord[0][1]-radDeltaY[i]+radDY[i]])
for i in range(0,len(radCoordinates)):
    radCoordinates[i].append(0)


## Creating geometric error in droppers
# Defining lengths of each dropper
drLength=list()
# Deflection amplitude:
drDeflection =0.005
```

```python
# Deflectionpoints
drNumDefPoints = 50
# Midpoints on each dropper
drCreateMidPoints = 2*drNumDefPoints - 1
# Defining dropper coordinates to be able to create sin-wave geometry
drXCoordinates = list()
drYCoordinates = list()
drZCoordinates = list()
drY = list()
drXTotCoordinates = list()
drYTotCoordinates = list()
drZTotCoordinates = list()
drYTot = list()
for i in range(0,len(drCoordinates)):
    # Deflectionpoints
    drLength.append(drCoordinates[i][1][1]-drCoordinates[i][0][1])
    drY.append(np.linspace(0,drLength[i],drNumDefPoints))
    drXCoordinates.append(np.sin(drY[i]*np.pi/(drLength[i]))*drDeflection)
    drXCoordinates[i][-1] = 0
    drXCoordinates[i][0] = 0
    drXCoordinates[i] = drXCoordinates[i]+drCoordinates[i][0][0]
    drYCoordinates.append(drY[i] + drCoordinates[i][0][1])
    drZCoordinates.append([drCoordinates[i][0][2]]*len(drYCoordinates[0]))
    # Midpoints on droppers
    drYTot.append(np.linspace(0,drLength[i],drCreateMidPoints))
    drXTotCoordinates.append(np.sin(drYTot[i]*np.pi/(drLength[i]))*drDeflection)
    drXTotCoordinates[i][-1] = 0
    drXTotCoordinates[i][0] = 0
    drXTotCoordinates[i] = drXTotCoordinates[i]+drCoordinates[i][0][0]
    drYTotCoordinates.append(drYTot[i] + drCoordinates[i][0][1])
```

```
        drZTotCoordinates.append([drCoordinates[i][0][2]]*len(drYTotCoordinates[0]))


# Deflectionpoints
dr1SkewGeometry = [[0]*3]*(len(drXCoordinates[0])*2)
dr2SkewGeometry = [[0]*3]*(len(drXCoordinates[0])*2)
dr3SkewGeometry = [[0]*3]*(len(drXCoordinates[0])*2)
dr4SkewGeometry = [[0]*3]*(len(drXCoordinates[0])*2)


##Making tuple for the skew geometry of the droppers
# First dropper
for j in range(1,len(dr1SkewGeometry),2):
    dr1SkewGeometry[j-1] = [drXCoordinates[0][int(j/2)],drYCoordinates[0][int(j/2)],\
    drZCoordinates[0][int(j/2)]]
    dr1SkewGeometry[j] = [drXCoordinates[0][int(j/2)],drYCoordinates[0][int(j/2)],\
    drZCoordinates[0][int(j/2)]]
    dr1SkewGeometry[j-1] = tuple(dr1SkewGeometry[j-1])
    dr1SkewGeometry[j] = tuple(dr1SkewGeometry[j])
del dr1SkewGeometry[0]
del dr1SkewGeometry[-1]
for i in range(0,len(dr1SkewGeometry)):
    dr1SkewGeometry[i] = tuple(dr1SkewGeometry[i*2:i*2+2])
del dr1SkewGeometry[int(len(dr1SkewGeometry)/2):-1]
del dr1SkewGeometry[-1]
# Second dropper
for j in range(1,len(dr2SkewGeometry),2):
    dr2SkewGeometry[j-1] = [drXCoordinates[1][int(j/2)],drYCoordinates[1][int(j/2)],\
    drZCoordinates[1][int(j/2)]]
    dr2SkewGeometry[j] = [drXCoordinates[1][int(j/2)],drYCoordinates[1][int(j/2)],\
    drZCoordinates[1][int(j/2)]]
    dr2SkewGeometry[j-1] = tuple(dr2SkewGeometry[j-1])
```

```python
        dr2SkewGeometry[j] = tuple(dr2SkewGeometry[j])
del dr2SkewGeometry[0]
del dr2SkewGeometry[-1]


for i in range(0,len(dr2SkewGeometry)):
    dr2SkewGeometry[i] = tuple(dr2SkewGeometry[i*2:i*2+2])
del dr2SkewGeometry[int(len(dr2SkewGeometry)/2):-1]
del dr2SkewGeometry[-1]


# Third dropper
for j in range(1,len(dr3SkewGeometry),2):
    dr3SkewGeometry[j-1] = [drXCoordinates[2][int(j/2)],drYCoordinates[2][int(j/2)],\
    drZCoordinates[2][int(j/2)]]
    dr3SkewGeometry[j] = [drXCoordinates[2][int(j/2)],drYCoordinates[2][int(j/2)],\
    drZCoordinates[2][int(j/2)]]
    dr3SkewGeometry[j-1] = tuple(dr3SkewGeometry[j-1])
    dr3SkewGeometry[j] = tuple(dr3SkewGeometry[j])
del dr3SkewGeometry[0]
del dr3SkewGeometry[-1]


for i in range(0,len(dr3SkewGeometry)):
    dr3SkewGeometry[i] = tuple(dr3SkewGeometry[i*2:i*2+2])
del dr3SkewGeometry[int(len(dr3SkewGeometry)/2):-1]
del dr3SkewGeometry[-1]


# Fourth dropper
for j in range(1,len(dr4SkewGeometry),2):
    dr4SkewGeometry[j-1] = [drXCoordinates[3][int(j/2)],drYCoordinates[3][int(j/2)],\
    drZCoordinates[3][int(j/2)]]
    dr4SkewGeometry[j] = [drXCoordinates[3][int(j/2)],drYCoordinates[3][int(j/2)],\
```

```python
            drZCoordinates[3][int(j/2)]]
        dr4SkewGeometry[j-1] = tuple(dr4SkewGeometry[j-1])
        dr4SkewGeometry[j] = tuple(dr4SkewGeometry[j])
del dr4SkewGeometry[0]
del dr4SkewGeometry[-1]


for i in range(0,len(dr4SkewGeometry)):
    dr4SkewGeometry[i] = tuple(dr4SkewGeometry[i*2:i*2+2])
del dr4SkewGeometry[int(len(dr4SkewGeometry)/2):-1]
del dr4SkewGeometry[-1]


drSkewGeometry = [dr1SkewGeometry,dr2SkewGeometry,dr3SkewGeometry,dr4SkewGeometry]


## Making input for the midpoints of the droppers (to create dropper sets with)
dr1Midpoint = [[0]*3]*(len(drXTotCoordinates[0])/2)
dr2Midpoint = [[0]*3]*(len(drXTotCoordinates[1])/2)
dr3Midpoint = [[0]*3]*(len(drXTotCoordinates[2])/2)
dr4Midpoint = [[0]*3]*(len(drXTotCoordinates[3])/2)
for j in range(0,len(dr1Midpoint)):
    dr1Midpoint[j] = [drXTotCoordinates[0][j*2],drYTotCoordinates[0][j*2],\
    drZTotCoordinates[0][j*2]]
    dr1Midpoint.append([drXTotCoordinates[0][-2],drYTotCoordinates[0][-2],\
    drZTotCoordinates[0][-2]])
for j in range(0,len(dr2Midpoint)):
    dr2Midpoint[j] = [drXTotCoordinates[1][j*2],drYTotCoordinates[1][j*2],\
    drZTotCoordinates[1][j*2]]
    dr2Midpoint.append([drXTotCoordinates[1][-2],drYTotCoordinates[1][-2],\
    drZTotCoordinates[1][-2]])
for j in range(0,len(dr3Midpoint)):
    dr3Midpoint[j] = [drXTotCoordinates[2][j*2],drYTotCoordinates[2][j*2],\
```

```
            drZTotCoordinates[2][j*2]]
            dr3Midpoint.append([drXTotCoordinates[2][-2],drYTotCoordinates[2][-2],\
            drZTotCoordinates[2][-2]])
    for j in range(0,len(dr4Midpoint)):
            dr4Midpoint[j] = [drXTotCoordinates[3][j*2],drYTotCoordinates[3][j*2],\
            drZTotCoordinates[3][j*2]]
            dr4Midpoint.append([drXTotCoordinates[3][-2],drYTotCoordinates[3][-2],\
            drZTotCoordinates[3][-2]])


    ##Geometry for cantilevers
    # Offset from endpoint of CW/MW:
    z_offset = 0.05
    z_left = cwCoordinates[0][0][2] + z_offset
    z_right = cwCoordinates[-1][-1][2] - z_offset
    left_cw_cant = [[taCoordinates[0][0][0],cwCoordinates[0][0][1],z_left],[cwCoordinates[0][0][0],\
            cwCoordinates[0][0][1],z_left],[2.4,cwCoordinates[0][0][1],z_left]]
    left_mw_cant = [[taCoordinates[0][0][0],mwCoordinates[0][0][1],z_left],[mwCoordinates[0][0][0],\
            mwCoordinates[0][0][1],z_left],[2.4,mwCoordinates[0][0][1],z_left]]
    right_mw_cant = [[taCoordinates[0][0][0],mwCoordinates[-1][-1][1],z_right],[mwCoordinates[-1][-1][0],\
            mwCoordinates[-1][-1][1],z_right],[2.4,mwCoordinates[-1][-1][1],z_right]]
    right_cw_cant = [[taCoordinates[0][0][0],cwCoordinates[-1][-1][1],z_right],[cwCoordinates[-1][-1][0],\
            cwCoordinates[-1][-1][1],z_right],[2.4,cwCoordinates[-1][-1][1],z_right]]


    cantCoordinates =[left_cw_cant,left_mw_cant,right_cw_cant,right_mw_cant]
    cantNames = ['Left CW Cantilever','Left MW cantilever','Right CW Cantilever','Right MW Cantilever']
    # Creating tuples
    for i in range(0,len(cantCoordinates)):
        for j in range(1,len(cantCoordinates[i])*2-3,2):
            cantCoordinates[i].insert(j,cantCoordinates[i][j])
    for i in range(len(list_of_components)):
```

```python
        k=0
        while (k < len(list_of_components[i])):
            list_of_components[i][k] = tuple(list_of_components[i][k])
            k = k+1


# Making the tuple in the arrangement Abaqus wants:
#((coordinate1,coordinate2),(coordinate2,coordinate3)) etc for all components:
real_cantCoordinates=[0]*len(cantCoordinates)
for i in range(len(real_cantCoordinates)):
    real_cantCoordinates[i] =[0]*2


for i in range(len(real_cantCoordinates)):
    k=0
    while (k < 2):
        real_cantCoordinates[i][k] = tuple(cantCoordinates[i][k*2:k*2+2])
        k=k+1
cantCoordinates = real_cantCoordinates


## GEOMETRY FOR WIRES CONNECTED TO CANTILEVERES
# Left wires are in +z-direction, right wires are in -z-direction, globally:
coordSign = [1,1,-1,-1]
# Distance from CW/MW to where the walled wire is connected to the cantilever:
x_offset = 0.2
cantWires = list()
cantWireNames=['Left CW cantilever wire','Left MW cantilever wire',\
'Right CW cantilever wire','Right MW cantilever wire']
for i in range(0,len(cantCoordinates)):
    cantWires.append([[cantCoordinates[i][0][0][0],cantCoordinates[i][0][0][1],\
    cantCoordinates[i][0][0][2]+4.6*coordSign[i]],[cantCoordinates[i][0][1][0]-x_offset,\
    cantCoordinates[i][0][1][1],cantCoordinates[i][0][0][2]]])
```

```python
##DROPPER SUPPRESSING:

for i in dropperSuppress:
    mdb.models['Model-1'].parts['Whole Model'].features[drSuppressable[i-1]].suppress()


##GEOMETRY INPUTS TO ABAQUS/CAE
# Creating one part - 'Whole Model'
mdb.models['Model-1'].Part(dimensionality=THREE_D, name='Whole Model', type=
    DEFORMABLE_BODY)
#Messenger wire geometry (and reference point)
mdb.models['Model-1'].parts['Whole Model'].ReferencePoint(point=(0.0, 0.0, 0.0))
mdb.models['Model-1'].parts['Whole Model'].WirePolyLine(mergeType=IMPRINT, meshable=
    ON, points=(mwCoordinates))
# Contact wire geometry
mdb.models['Model-1'].parts['Whole Model'].WirePolyLine(mergeType=IMPRINT, meshable=
    ON, points=(cwCoordinates))
# Dropper geometry
for i in range(0,(numDr)):
    mdb.models['Model-1'].parts['Whole Model'].WirePolyLine(mergeType=IMPRINT, meshable=
        ON, points=(drSkewGeometry[i]))
# Top anchor
mdb.models['Model-1'].parts['Whole Model'].WirePolyLine(mergeType=IMPRINT, meshable=
    ON, points=(taCoordinates))
# Cantilevered tube
mdb.models['Model-1'].parts['Whole Model'].WirePolyLine(mergeType=IMPRINT, meshable=
    ON, points=(ctCoordinates))
# Registration arm dropper
mdb.models['Model-1'].parts['Whole Model'].WirePolyLine(mergeType=IMPRINT, meshable=
    ON, points=(radCoordinates))
```

```python
# Registration arm
mdb.models['Model-1'].parts['Whole Model'].WirePolyLine(mergeType=IMPRINT, meshable=
    ON, points=(raCoordinates))
# Steady arm
mdb.models['Model-1'].parts['Whole Model'].WirePolyLine(mergeType=IMPRINT, meshable=
    ON, points=(saCoordinates))
# Cantilevers
for i in range(0,len(cantCoordinates)):
    mdb.models['Model-1'].parts['Whole Model'].WirePolyLine(mergeType=IMPRINT, meshable=
        ON, points=(cantCoordinates[i]))
# Cantilever wires
for i in range(0,len(cantWires)):
    mdb.models['Model-1'].parts['Whole Model'].WirePolyLine(mergeType=IMPRINT, meshable=
        ON, points=(cantWires[i]))


## CREATING SETS
# Messenger wire
mdb.models['Model-1'].parts['Whole Model'].Set(edges=
    mdb.models['Model-1'].parts['Whole Model'].edges.findAt((mwMidpoint[0], ), (mwMidpoint[1], ), \
    (mwMidpoint[2],   ), (mwMidpoint[3], ), (mwMidpoint[4], ),(mwMidpoint[5], ), ), \
    name='Messenger wire')
# Contact wire
mdb.models['Model-1'].parts['Whole Model'].Set(edges=
    mdb.models['Model-1'].parts['Whole Model'].edges.findAt((cwMidpoint[0], ), (cwMidpoint[1], ),
    (cwMidpoint[2],  ), (cwMidpoint[3], ), (cwMidpoint[4], ),(cwMidpoint[5], ), ), \
    name='Contact wire')
# Top anchor
mdb.models['Model-1'].parts['Whole Model'].Set(edges=
    mdb.models['Model-1'].parts['Whole Model'].edges.findAt((taMidpoint[0], ), (taMidpoint[1], ), \
```

```
        (taMidpoint[2],  ),), name='Top anchor')
```

```
mdb.models['Model-1'].parts['Whole Model'].Set(edges=
        mdb.models['Model-1'].parts['Whole Model'].edges.findAt((cantCoordinates[0][0][0], ),\
        (cantCoordinates[0][-1][-1], ), (cantWires[0][1], ),), name=cantNames[0])
```

```
mdb.models['Model-1'].parts['Whole Model'].Set(edges=
        mdb.models['Model-1'].parts['Whole Model'].edges.findAt((cantCoordinates[1][0][0], ),\
        (cantCoordinates[1][-1][-1], ), (cantWires[1][1], ),), name=cantNames[1])
```

```
mdb.models['Model-1'].parts['Whole Model'].Set(edges=
         mdb.models['Model-1'].parts['Whole Model'].edges.findAt((cantCoordinates[2][0][0], ),\
        (cantCoordinates[2][-1][-1], ), (cantWires[2][1], ),), name=cantNames[2])
```

```
mdb.models['Model-1'].parts['Whole Model'].Set(edges=
        mdb.models['Model-1'].parts['Whole Model'].edges.findAt((cantCoordinates[3][0][0], ),\
        (cantCoordinates[3][-1][-1], ), (cantWires[3][1], ),), name=cantNames[3])
```

```
for i in range(0,len(cantWires)):
    mdb.models['Model-1'].parts['Whole Model'].Set(edges=
    mdb.models['Model-1'].parts['Whole Model'].edges.findAt((cantWires[i][0],\
    ),), name=cantWireNames[i])
```

```
mdb.models['Model-1'].parts['Whole Model'].Set(edges=
        mdb.models['Model-1'].parts['Whole Model'].edges.findAt((ctMidpoint[0], ), (ctMidpoint[1], ),), \
        name='Cantilevered tube')
```

```python
# Registration arm dropper
mdb.models['Model-1'].parts['Whole Model'].Set(edges=
    mdb.models['Model-1'].parts['Whole Model'].edges.findAt((radCoordinates[0], ),
    (radCoordinates[1], ), (radCoordinates[2], ),(radCoordinates[3], ),
    (radCoordinates[4], ), (radCoordinates[5], ), (radCoordinates[6], ),
    (radCoordinates[7], ), (radCoordinates[8], ), (radCoordinates[9], ),), name='Registration arm
    dropper')
# Registration arm
mdb.models['Model-1'].parts['Whole Model'].Set(edges=
    mdb.models['Model-1'].parts['Whole Model'].edges.findAt((raMidpoint[0], ), (raMidpoint[1], ), \
    (raMidpoint[2],   ), (raMidpoint[3], ),), name='Registration arm')
# Steady arm
mdb.models['Model-1'].parts['Whole Model'].Set(edges=
    mdb.models['Model-1'].parts['Whole Model'].edges.findAt((saMidpoint[0], ),), name='Steady arm')
#Dropper sets
mdb.models['Model-1'].parts['Whole Model'].Set(edges=
    mdb.models['Model-1'].parts['Whole Model'].edges.findAt(
    (dr1Midpoint[0], ), (dr1Midpoint[1], ), (dr1Midpoint[2], ),
    (dr1Midpoint[3], ), (dr1Midpoint[4], ), (dr1Midpoint[5], ), (dr1Midpoint[6], ),
    (dr1Midpoint[7], ), (dr1Midpoint[8], ), (dr1Midpoint[9], ), (dr1Midpoint[10], ),
    (dr1Midpoint[11], ), (dr1Midpoint[12], ), (dr1Midpoint[13], ), (dr1Midpoint[14], ),
    (dr1Midpoint[15], ), (dr1Midpoint[16], ), (dr1Midpoint[17], ), (dr1Midpoint[18], ),
    (dr1Midpoint[19], ), (dr1Midpoint[20], ), (dr1Midpoint[21], ), (dr1Midpoint[22], ),
    (dr1Midpoint[23], ), (dr1Midpoint[24], ), (dr1Midpoint[25], ), (dr1Midpoint[26], ),
    (dr1Midpoint[27], ), (dr1Midpoint[28], ), (dr1Midpoint[29], ), (dr1Midpoint[30], ),
    (dr1Midpoint[31], ), (dr1Midpoint[32], ), (dr1Midpoint[33], ), (dr1Midpoint[34], ),
    (dr1Midpoint[35], ), (dr1Midpoint[36], ), (dr1Midpoint[37], ), (dr1Midpoint[38], ),
    (dr1Midpoint[39], ), (dr1Midpoint[40], ), (dr1Midpoint[41], ), (dr1Midpoint[42], ),
    (dr1Midpoint[43], ), (dr1Midpoint[44], ), (dr1Midpoint[45], ), (dr1Midpoint[46], ),
```

```
        (dr1Midpoint[47], ), (dr1Midpoint[48], ), (dr1Midpoint[49], ), ), name=
         'Dropper 1')
mdb.models['Model-1'].parts['Whole Model'].Set(edges=
        mdb.models['Model-1'].parts['Whole Model'].edges.findAt(
        (dr2Midpoint[0], ),(dr2Midpoint[1], ), (dr2Midpoint[2], ),
        (dr2Midpoint[3], ), (dr2Midpoint[4], ), (dr2Midpoint[5], ), (dr2Midpoint[6], ),
        (dr2Midpoint[7], ), (dr2Midpoint[8], ), (dr2Midpoint[9], ), (dr2Midpoint[10], ),
        (dr2Midpoint[11], ), (dr2Midpoint[12], ), (dr2Midpoint[13], ), (dr2Midpoint[14], ),
        (dr2Midpoint[15], ), (dr2Midpoint[16], ), (dr2Midpoint[17], ), (dr2Midpoint[18], ),
        (dr2Midpoint[19], ), (dr2Midpoint[20], ), (dr2Midpoint[21], ), (dr2Midpoint[22], ),
        (dr2Midpoint[23], ), (dr2Midpoint[24], ), (dr2Midpoint[25], ), (dr2Midpoint[26], ),
        (dr2Midpoint[27], ), (dr2Midpoint[28], ), (dr2Midpoint[29], ), (dr2Midpoint[30], ),
        (dr2Midpoint[31], ), (dr2Midpoint[32], ), (dr2Midpoint[33], ), (dr2Midpoint[34], ),
        (dr2Midpoint[35], ), (dr2Midpoint[36], ), (dr2Midpoint[37], ), (dr2Midpoint[38], ),
        (dr2Midpoint[39], ), (dr2Midpoint[40], ), (dr2Midpoint[41], ), (dr2Midpoint[42], ),
        (dr2Midpoint[43], ), (dr2Midpoint[44], ), (dr2Midpoint[45], ), (dr2Midpoint[46], ),
        (dr2Midpoint[47], ), (dr2Midpoint[48], ), (dr2Midpoint[49], ), ), name=
        'Dropper 2')
mdb.models['Model-1'].parts['Whole Model'].Set(edges=
        mdb.models['Model-1'].parts['Whole Model'].edges.findAt(
        (dr3Midpoint[0], ), (dr3Midpoint[1], ), (dr3Midpoint[2], ),
        (dr3Midpoint[3], ), (dr3Midpoint[4], ), (dr3Midpoint[5], ), (dr3Midpoint[6], ),
        (dr3Midpoint[7], ), (dr3Midpoint[8], ), (dr3Midpoint[9], ), (dr3Midpoint[10], ),
        (dr3Midpoint[11], ), (dr3Midpoint[12], ), (dr3Midpoint[13], ), (dr3Midpoint[14], ),
        (dr3Midpoint[15], ), (dr3Midpoint[16], ), (dr3Midpoint[17], ), (dr3Midpoint[18], ),
        (dr3Midpoint[19], ), (dr3Midpoint[20], ), (dr3Midpoint[21], ), (dr3Midpoint[22], ),
        (dr3Midpoint[23], ), (dr3Midpoint[24], ), (dr3Midpoint[25], ), (dr3Midpoint[26], ),
        (dr3Midpoint[27], ), (dr3Midpoint[28], ), (dr3Midpoint[29], ), (dr3Midpoint[30], ),
        (dr3Midpoint[31], ), (dr3Midpoint[32], ), (dr3Midpoint[33], ), (dr3Midpoint[34], ),
        (dr3Midpoint[35], ), (dr3Midpoint[36], ), (dr3Midpoint[37], ), (dr3Midpoint[38], ),
```

```
        (dr3Midpoint[39], ), (dr3Midpoint[40], ), (dr3Midpoint[41], ), (dr3Midpoint[42], ),

        (dr3Midpoint[43], ), (dr3Midpoint[44], ), (dr3Midpoint[45], ), (dr3Midpoint[46], ),

        (dr3Midpoint[47], ), (dr3Midpoint[48], ), (dr3Midpoint[49], ), ), name=

        'Dropper 3')
mdb.models['Model-1'].parts['Whole Model'].Set(edges=

        mdb.models['Model-1'].parts['Whole Model'].edges.findAt(

        (dr4Midpoint[1], ), (dr4Midpoint[2], ),

        (dr4Midpoint[3], ), (dr4Midpoint[4], ), (dr4Midpoint[5], ), (dr4Midpoint[6], ),

        (dr4Midpoint[7], ), (dr4Midpoint[8], ), (dr4Midpoint[9], ), (dr4Midpoint[10], ),

        (dr4Midpoint[11], ), (dr4Midpoint[12], ), (dr4Midpoint[13], ), (dr4Midpoint[14], ),

        (dr4Midpoint[15], ), (dr4Midpoint[16], ), (dr4Midpoint[17], ), (dr4Midpoint[18], ),

        (dr4Midpoint[19], ), (dr4Midpoint[20], ), (dr4Midpoint[21], ), (dr4Midpoint[22], ),

        (dr4Midpoint[23], ), (dr4Midpoint[24], ), (dr4Midpoint[25], ), (dr4Midpoint[26], ),

        (dr4Midpoint[27], ), (dr4Midpoint[28], ), (dr4Midpoint[29], ), (dr4Midpoint[30], ),

        (dr4Midpoint[31], ), (dr4Midpoint[32], ), (dr4Midpoint[33], ), (dr4Midpoint[34], ),

        (dr4Midpoint[35], ), (dr4Midpoint[36], ), (dr4Midpoint[37], ), (dr4Midpoint[38], ),

        (dr4Midpoint[39], ), (dr4Midpoint[40], ), (dr4Midpoint[41], ), (dr4Midpoint[42], ),

        (dr4Midpoint[43], ), (dr4Midpoint[44], ), (dr4Midpoint[45], ), (dr4Midpoint[46], ),

        (dr4Midpoint[47], ), (dr4Midpoint[48], ), (dr4Midpoint[49], ), ), name=

        'Dropper 4')
# IMPORTANT: Command to get the sets arranged as wanted:
session.journalOptions.setValues(replayGeometry=COORDINATE, recoverGeometry=COORDINATE)
###########################  END OF GEOMETRY-SCRIPT ###############################
```

D.2   material properties, profiles and sections input

```
################## START OF MATERIAL, PROFILES AND SECTIONS SCRIPT ####################
## MATERIAL INPUT
# Material properties MW, CW and droppers, aluminium and steel for support
# (S25/S20 existing values  2.feb2015)
# Gathered from textfile materialprop.txt
matName = np.genfromtxt('materialprop.txt',comments='#', dtype='str', usecols=0, delimiter=',')

matEmodule = np.genfromtxt('materialprop.txt',comments='#', dtype='float', usecols=1, delimiter=',')

matDensity = np.genfromtxt('materialprop.txt',comments='#', dtype='float', usecols=2, delimiter=',')

matPoisson = np.genfromtxt('materialprop.txt',comments='#', dtype='float', usecols=3, delimiter=',')

# Defining shear modulus, to use in generalized profiles
matGmodule = [0]*len(matEmodule)

for j in range(len(matName)):

    matGmodule[j] = matEmodule[j]/(2*(1+matPoisson[j]))

    mdb.models['Model-1'].Material(name=matName[j])

    mdb.models['Model-1'].materials[matName[j]].Elastic(table=((

    matEmodule[j], matPoisson[j]), ))

    mdb.models['Model-1'].materials[matName[j]].Density(table=((matDensity[j], ), ))


## PROFILES INPUT
# Creating section name and profile name the same: from section_MaterialAndName.txt
sectionName = np.genfromtxt('section_MaterialAndName.txt',comments='#', dtype='str', usecols=1,
delimiter=',')

#CW - generalized profile
mdb.models['Model-1'].GeneralizedProfile(area=0.00012097, gammaO=0.0, gammaW=
    0.0, i11=1.3442e-10, i12=0.0, i22=1.1189e-10, j=1.8446e-09, name=sectionName[0])

#MW
mdb.models['Model-1'].CircularProfile(name=sectionName[1], r=0.00525)

#Droppers (1-4 are the same)
mdb.models['Model-1'].CircularProfile(name=(sectionName[2]), r=0.00225)
```

#Top anchor

mdb.models['Model-1'].PipeProfile(formulation=THICK_WALL, name=sectionName[3], r=
    0.0275, t=0.0065)

#Cantilevered tube

mdb.models['Model-1'].PipeProfile(formulation=THICK_WALL, name=
    sectionName[4], r=0.0275, t=0.0065)

Registration arm

mdb.models['Model-1'].PipeProfile(formulation=THICK_WALL, name=
    sectionName[5], r=0.021, t=0.004)

Reg arm dropper

mdb.models['Model-1'].CircularProfile(name=sectionName[6], r=0.003)

Steady arm

mdb.models['Model-1'].RectangularProfile(a=0.025, b=0.013, name=sectionName[7])

Cantilevers

mdb.models['Model-1'].GeneralizedProfile(area=0.0038364, gammaO=0.0, gammaW=
    0.0, i11=3.731401e-06, i12=0.0, i22=5.810597e-06, j=1.5e-05, name='Cantilever')

Wires connected to cantilevers have the same profile as messenger wire

SECTION DATA

Gathered from textfile section_MaterialAndName.txt

sectionMaterial = np.genfromtxt('section_MaterialAndName.txt',comments='#', dtype='str', usecols=0, delimiter=',')

sectionPoisson = np.genfromtxt('section_MaterialAndName.txt',comments='#', dtype='float', usecols=2, delimiter=',')

expansionCoeff = 1.7e-05   #Same for CW/Dropper/MW

for i in range(1,len(sectionName)):

    if (i == 2):

        for j in range(1,numDr+1):

            mdb.models['Model-1'].BeamSection(consistentMassMatrix=False,

```
                    integration=DURING_ANALYSIS, material=sectionMaterial[i], name=sectionName[i]+''+
                    str(j),poissonRatio=sectionPoisson[i], profile=sectionName[i], temperatureVar=LINEAR)
        else:
                mdb.models['Model-1'].BeamSection(consistentMassMatrix=False, integration=
                    DURING_ANALYSIS, material=sectionMaterial[i], name=sectionName[i],
                    poissonRatio=sectionPoisson[i], profile=sectionName[i], temperatureVar=LINEAR)
```

SECTION DATA FOR CONTACT WIRE: GENERALIZED DATA

```
mdb.models['Model-1'].BeamSection(alphaDamping=0.0, beamShape=CONSTANT,
        betaDamping=0.0, centroid=(0.0, 0.0), compositeDamping=0.0,
        consistentMassMatrix=False, density=matDensity[1], dependencies=0, integration=
        BEFORE_ANALYSIS, name=sectionName[0], poissonRatio=matPoisson[1], profile=
        sectionName[0], shearCenter=(0.0, 0.0), table=((matEmodule[1], matGmodule[1],
        expansionCoeff,), ), temperatureDependency=OFF, thermalExpansion=ON)
```

SECTION FOR CANTILEVERS : GENERALIZED DATA

```
mdb.models['Model-1'].BeamSection(alphaDamping=0.0, beamShape=CONSTANT,
        betaDamping=0.0, centroid=(0.0, 0.0), compositeDamping=0.0,
        consistentMassMatrix=False, density=matDensity[3], dependencies=0, integration=
        BEFORE_ANALYSIS, name='Cantilever', poissonRatio=matPoisson[3], profile=
        'Cantilever', shearCenter=(0.0, 0.0), table=((matEmodule[3], matGmodule[3]), ),
        temperatureDependency=OFF, thermalExpansion=OFF)
```

SECTION DATA FOR CANTILEVER WIRES – not needed, use messenger wire section.

```
# Second for loop is to get Dropper 1, Dropper 2 etc...

for i in range(1,len(sectionMaterial)):
    if (i == 2):
        for j in range(1,numDr+1):
        mdb.models['Model-1'].parts['Whole Model'].SectionAssignment(offset=0.0,
            offsetField='', offsetType=MIDDLE_SURFACE, region=
            mdb.models['Model-1'].parts['Whole Model'].sets[sectionName[i]+''+ str(j)],
            sectionName=sectionName[i]+''+ str(j), thicknessAssignment=FROM_SECTION)
    else:
        mdb.models['Model-1'].parts['Whole Model'].SectionAssignment(offset=0.0,
            offsetField='', offsetType=MIDDLE_SURFACE, region=
            mdb.models['Model-1'].parts['Whole Model'].sets[sectionName[i]],
            sectionName=sectionName[i], thicknessAssignment=FROM_SECTION)

for i in range(1,len(sectionName)):
    if (i==2):
        for j in range(1,numDr+1):
            mdb.models['Model-1'].parts['Whole Model'].assignBeamSectionOrientation(method=
                N1_COSINES, n1=(0.0, 0, -1.0), region=
                mdb.models['Model-1'].parts['Whole Model'].sets[sectionName[i]+'' + str(j)])
    else:
            mdb.models['Model-1'].parts['Whole Model'].assignBeamSectionOrientation(method=
                N1_COSINES, n1=(0.0, 1.0, 0.0), region=
                mdb.models['Model-1'].parts['Whole Model'].sets[sectionName[i]])


# Contact wire - generalized, treated separately
mdb.models['Model-1'].parts['Whole Model'].SectionAssignment(offset=0.0,
    offsetField='', offsetType=MIDDLE_SURFACE, region=
    mdb.models['Model-1'].parts['Whole Model'].sets['Contact wire'],
```

```python
        sectionName='Contact wire', thicknessAssignment=FROM_SECTION)
mdb.models['Model-1'].parts['Whole Model'].assignBeamSectionOrientation(method=
    N1_COSINES, n1=(0.0, 1.0, 0.0), region=
    mdb.models['Model-1'].parts['Whole Model'].sets['Contact wire'])


# Cantilevers – generalized, treated separately
for i in range(0,len(cantCoordinates)):
    mdb.models['Model-1'].parts['Whole Model'].SectionAssignment(offset=0.0,
        offsetField='', offsetType=MIDDLE_SURFACE, region=
        mdb.models['Model-1'].parts['Whole Model'].sets[cantNames[i]],
        sectionName='Cantilever', thicknessAssignment=FROM_SECTION)
    mdb.models['Model-1'].parts['Whole Model'].assignBeamSectionOrientation(method=
        N1_COSINES, n1=(0.0, 1.0, 0.0), region=
        mdb.models['Model-1'].parts['Whole Model'].sets[cantNames[i]])
# Cantilever wires:
for i in range(0,len(cantWires)):
    mdb.models['Model-1'].parts['Whole Model'].SectionAssignment(offset=0.0,
        offsetField='', offsetType=MIDDLE_SURFACE, region=
        mdb.models['Model-1'].parts['Whole Model'].sets[cantWireNames[i]],
        sectionName='Messenger wire', thicknessAssignment=FROM_SECTION)
    mdb.models['Model-1'].parts['Whole Model'].assignBeamSectionOrientation(method=
        N1_COSINES, n1=(0.0, 0.0, -1-0), region=
        mdb.models['Model-1'].parts['Whole Model'].sets[cantWireNames[i]])


############### END CREATING MATERIAL, PROFILES AND SECTIONS ####################
```

Appendix E

Zip-file content

The zip-file attached to this thesis contains the following:

1. Folder: Basis_Script. This folder contains a README file, which explains how to run the Python script, to generate the base model in Abaqus/CAE. It also contains the .cae file which are generated from the script, and its accompanying .jnl file.

2. Folder: RunSeveralJobs. This folder contains the complete model which has been used in this thesis, which is called ModelAllJobs.cae. It also contains the script used to run several jobs, for different tension-combinations. The README file in this folder explains how to run the script correctly, and obtain many tension-combinations.